UCSF

Title

Manipulation of mitochondria and Ras superfamily small GTPases by Legionella pneumophila

Permalink

https://escholarship.org/uc/item/8qs3n2x4

Author

Bhadkamkar, Varun Louis

Publication Date

2023

Supplemental Material

https://escholarship.org/uc/item/8qs3n2x4#supplemental

Peer reviewed|Thesis/dissertation

Manipulation of mitochondria and Ras superfamily small GTPases by Legionella pneumophila

by
Varun Bhadkamkar

DISSERTATION
Submitted in partial satisfaction of the requirements for degree of
DOCTOR OF PHILOSOPHY

in

Cell Biology

in the

GRADUATE DIVISION
of the
UNIVERSITY OF CALIFORNIA, SAN FRANCISCO

Approved:

DocuSigned by:

Martin Kampmann

———03BA4012CC044AF…

Martin Kampmann

Chair

DocuSigned by:

Roshanak Irannejad

Roshanak Irannejad

DocuSigned by:

Kevan Shokat

Kevan Shokat

DocuSigned by:

Shaeri Mukherjee

———7AA908684B40471…

Shaeri Mukherjee

_____

Committee Members

Acknowledgments

The completion of this PhD took a village, and there are many to whom I owe thanks. First and foremost, to my advisor Shaeri, I am grateful that you took a chance on me, a biochemistry major with very little cell biological experience. I will never forget my rotation, where we immunostained COS cells for tubulin, ER, and mitochondria, just so you could show me how amazing the cell is. The lab I joined in July 2018 was still in the early stages of development, and the lab I am leaving now in December 2023 is a fully fledged research operation. It has been a joy to be a part of this period of growth and change, and your support was integral in guiding me through the successes and failures of the past few years.

I'd next like to acknowledge the many scientific mentors who have trained and supported me throughout the years. To Tony Norcia, Peter Køhler, Simin Rahigi, Amy Gehring: thank you for your mentorship and for encouraging me to follow my dreamy scientific passions. Your patience and dedication to my training did not go unnoticed. To the members of my thesis committee, Martin Kampmann, Kevan Shokat, and Roshanak Irannejad: thank you for guiding me towards a timely completion. I'd like to particularly acknowledge Roshanak for her exceptional support from the first year of my PhD to now. Finally, to Dave Morgan, Geeta Narlikar, and Kaveh Ashrafi: you supported me immensely when I needed it the most.

The Mukherjee Lab has changed considerably over these six years, but I've been fortunate to have amazing lab mates at every stage. When I started, the lab was composed of Haley Gause, Nneji Ibe, Elias Taylor-Cornejo, Ady Steinbach, and Steven Moss (occasionally), with Edwin Jeng popping up from Stanford every few weeks. Then came Julia Noack, Hana Kimura, Advait Subramanian, and Tom Moss. Finally, in the past year, Alex Wooldredge and Attinder Chadha have joined as well. I cannot do justice to the support I've received from everyone. Edwin, working

with you on the CRISPR paper was a joy, and I'll never fail to be impressed with how productive you were in your PhD. Julia, we worked together briefly on the mitochondrial project, but I'm so grateful for your support.

Four of you have become good friends, and I believe there is no proper way to acknowledge this without roasting you. Alex "Elox" Wooldredge – your maturity and scientific prowess is far beyond your years, which compensates for your profound inability to buy cookware. Advait – I've watched you grow from a bright new postdoc who never bleaches his biohazard flask, to a PI-level researcher, who also never bleaches his biohazard flask. Keep doing you, but also, you should maybe bleach your biohazard flask BEFORE you pour it down the drain. Ady "Adrillama Steamboat" Steinbach – I don't know how to express my gratitude to you properly, so I'll just use the sound we use all-to-frequently to communicate with each other: meow. Tom "Thoomble McSomething" Moss – I'd write a longer acknowledgment for you but I don't think your computer would have the RAM to properly load this file anymore.

I will spare my other closest friends and classmates from further roasting. Chris Carlson and Elise Muñoz, you were my grad school "day ones" and going through this experience with you has been nothing short of amazing. I believe my friendship with you has truly made me a better person, and I'm excited where the next few years will bring us. To my other classmates, Dana Kennedy, Francesca del Frate, Luke Strauskulage (adopted classmate), Eric Simental, Henry Ng, Haley Gause, I'm so glad we found each other.

Several other friends deserve specific acknowledgement. To Melanie Subbiah and Rachel O'Sullivan, who have been constant sources of joy and wisdom, who I will travel any distance to see, who bravely took on PhDs themselves – you make my world so much better.

I'd like to finish by thanking my family. First and foremost, my father, Neal Bhadkamkar, who is my greatest scientific role model. From science fair projects, to summer electronics adventures, to homework help, to our conversations about biotech – you have always encouraged and supported me to follow my scientific dreams. You are the reason I think and explain science the ways that I do, and I don't know where I'd be without you. And to my mother, Odile Disch-Bhadkamkar, to you I owe much of my perseverance, my emotional depth, and my creativity. To both of you, I have come to increasingly recognize the sacrifices you have made for me, and I am so fortunate that I can come home to you when home is what I need the most. To my older brother, Ishan Fitkar – troubleshooting an experiment is nothing like being pinned down and tickled for 30 seconds, and I would often remind myself of that when struggling in lab. Catherine Fitkar – your ability to make Ishan comfortable in the wilderness is a testament to your ability to deeply care and support, and I'm grateful to have you as a part of our family. To my twin sister, Devyani Bhadkamkar – you are my closest friend, my greatest advocate, and my greatest critic. I don't know what I'd do without you.

Finally, to our family dog Lulu, you may not be able to read this but I'd still like to thank you for reminding me what truly is important: food, sleep, playtime, and cuddles. There is nothing that can cheer me up more than the big smile you put on your face when I come home. Thanks for being you.

Contributions

This thesis contains material reprinted as a manuscript in preparation (**Chapter 2**), as well as material in review for publication at *Molecular Biology of the Cell* (**Chapter 3**), modified to not include key experiments performed by Ady Steinbach. Chapter 2 includes an extensive revision of work initially presented in Noack, J *et al.* 2020 bioRxiv. Varun Bhadkamkar was responsible for re-analysis and visualization of the proteomic data, rewriting the manuscript, and experimentation included in the "Additional data and discussion" section. Citations are presented below.

Bhadkamkar VB*, Noack J*, Jimenez-Morales D, Stevenson E, Moss T, Jang GM, Krogan NJ, Swaney DL, Mukherjee S. Dynamic proteomic profiling of *Legionella pneumophila* infection unveils modulation of the host mitochondrial stress response pathway.
Conceptualization, S.M., V.B, J.N., D.J-M., D.L.S., and N.J.K.; Methodology, S.M., J.N., E.S., G.J., D.J-M., D.L.S., and N.J.K.; Data Curation, V.B., D.J-M., D.L.S., and J.N.; Validation, J.N., V.B.; Formal Analysis, V.B., D.J-M. and J.N.; Investigation, V.B., J.N., T.M.; Writing – V.B., J.N., T.M., S.M., D.L.S., and D.J-M.; Visualization, J.N, V.B., D.J.-M.; Funding Acquisition, S.M., D.L.S., and N.J.K.; Resources, S.M., D.L.S., and N.J.K.; Supervision, S.M., D.L.S., and N.J.K..

Bhadkamkar VB*, Steinbach AM*, Jimenez-Morales D, Stevenson E, Jang GM, Krogan NJ, Swaney DL, Mukherjee S. (*In Review*) Cross-family small GTPase ubiquitination by the intracellular pathogen Legionella pneumophila. *Molecular Biology of the Cell.*
Conceptualization, S.M., V.B., A.S., D.J-M., D.L.S., and N.J.K.; Methodology, S.M., E.S., G.M.J., D.J-M., D.L.S., and N.J.K.; Data Curation, A.S., V.B., D.J-M., D.L.S.; Validation, A.S., V.B.; Formal Analysis, A.S., V.B., D.J-M.; Investigation, V.B., A.S., T.M.; Writing, V.B., A.S., S.M., D.L.S., and D.J-M.; Visualization, A.S., V.B., D.J-M.; Funding Acquisition, S.M., D.L.S., and N.J.K.; Resources, S.M., D.L.S., and N.J.K.; Supervision, S.M., D.L.S., and N.J.K.

Manipulation of mitochondria and Ras superfamily small GTPases by *Legionella pneumophila*

Varun Bhadkamkar

Abstract

The intracellular bacterial pathogen *Legionella pneumophila* (*L.p.*) secretes ~330 bacterial effector proteins into the host cell that interfere with numerous cellular pathways and often regulate host cell proteins through post-translational modifications. Many aspects of L.p.-mediated pathogenesis, including the functions and targets of most effectors, remain elusive. To obtain a global overview of host cell rewiring and potential targets of these effectors, we analyzed the host cell proteome for changes in protein abundance, phosphorylation, and ubiquitination during *L.p.* infection. Our analysis reveals dramatic spatiotemporal changes in the host cell proteome that are dependent on the secretion of bacterial effectors. In **Chapter 2**, we show that *L.p.* substantially reshapes the mitochondrial proteome and induces a mitochondrial stress response with many similarities to the mitochondrial unfolded protein response (UPRmt). *L.p.* modulates downstream adaptive responses to mitochondrial stress by blocking the translation of transcription factors ATF4 and CHOP while allowing for the translation of ATF3. To our knowledge, this is the first evidence of manipulation of the UPRmt by a bacterial pathogen in mammalian cells. In **Chapter 3**, we show that *L.p.* infection results in increased ubiquitination of host proteins regulating subcellular trafficking and membrane dynamics, most notably 63 of ~160 mammalian Ras superfamily small GTPases. We determine that these small GTPases undergo non-degradative ubiquitination, and link their ubiquitination to recruitment to the *Legionella*-containing vacuole membrane. Finally, we find that the bacterial effectors SidC/SdcA play a

central role in cross-family small GTPase ubiquitination, and that these effectors function upstream of SidE-family ligases in the poly-ubiquitination and retention of GTPases in the LCV membrane. This work highlights the extensive reconfiguration of host ubiquitin signaling by bacterial effectors during infection and establishes simultaneous ubiquitination of small GTPases across the Ras superfamily as a novel consequence of *L.p.* infection. Overall, the findings presented in this dissertation position *L.p.* as a tool to better understand the regulation of mitochondria and small GTPases in uninfected contexts.

Table of Contents

List of Figures

Supplemental Files

Chapter 1: Introduction

1.1 Intracellular bacterial pathogens as tools to study cell biology

The human cellular environment is immensely complex. Inside every cell, a multitude of subcellular compartments components work together in elaborate networks to ensure continued cellular sustenance, replication, and functionality. These networks form the basis of foundational processes such as mitochondrial respiration, protein translation, DNA replication, and intracellular trafficking, which are further interlinked to guide important cellular decisions, such as when division should occur, how undesirable components should be removed, how a cell should respond to changing conditions, and when to initiate cell death. Central to these networks and decisions are proteins, which, in their vast array of forms and functions, act as the executors of most cellular processes. The presence of a protein alone is not sufficient for proper cellular function; protein activity is intimately tied to precise biological regulatory mechanisms which ensure that proteins are not only produced but are also active in the correct subcellular location, at the right times, and for the right durations. This meticulous control is essential to cellular homeostasis, and dysregulation of these biological regulatory mechanisms is a key driver of disease.

Since cells were first observed under microscopes by Robert Hooke and Anton van Leeuwenhoek in the 18th century, advances in the fields of physics, chemistry, physiology, genetics, and biochemistry, as well as considerable improvements in scientific methods, have greatly deepened our understanding of cells and their underlying biological regulatory mechanisms. A driving force behind many cell biological discoveries, however, has been the unchanging principle that biological regulatory mechanisms are challenging to study in the absence of some form of perturbation. By introducing deliberate perturbations, researchers have been able to dissect the myriad pathways and reactions within the cellular environment. For instance, pharmacological

agents, like cycloheximide, which inhibits protein synthesis, or brefeldin A, which disrupts protein transport, have proven invaluable in elucidating the intricate processes of protein synthesis and transport, respectively (Klausner et al., 1992; McKeehan and Hardesty, 1969; Moss et al., 2019). Genetic modifications, such as those achieved through techniques like CRISPR-Cas9 gene editing, have allowed for the targeted knockdown or knockout of specific genes, revealing their roles and interactions within larger cellular networks. By examining the consequences of these perturbations, we have furthered our understanding of the numerous checks and balances governing cellular processes, as well as the potential repercussions when these mechanisms falter. These examples underscore the fundamental tenet of cell biology: to truly understand the function and regulation of any component, one must observe what happens in its absence or altered state.

Among the many perturbagens that have facilitated cell biological discoveries, many have come in the form of living organisms. In the case of metazoan cell biology, for example, organisms like bacteria, fungi, and protozoa, have proven to be uniquely useful tools to unearth metazoan regulatory mechanisms. Through thousands of years of co-evolution, these many of these organisms have evolved dedicated biological strategies allowing them to interact with metazoan cells in mutualistic, commensal, or parasitic relationships. In turn, metazoan cells have developed mechanisms to both foster beneficial relationships and ward off potentially harmful ones. By studying the changes that occur when these organisms interact, as well as the genes, proteins, or molecules responsible for these changes, many of the intricacies of metazoan cell regulation have been unearthed.

Notable within the world of living "perturbagens" are intracellular bacterial pathogens, which enact diverse, elaborate pathogenic programs to rewire their host metazoan cells into habitable environments. These bacteria include notable human pathogens such as *Mycobacterium*

tuberculosis, *Salmonella enterica*, *Listeria monocytogenes*, *Chlamydia trachomatis*, and *Legionella pneumophila*. In order to subvert the host cell, intracellular bacterial pathogens use secretion systems, which facilitate the secretion of numerous protein toxins (often referred to as effectors) into the host cell. Intracellular pathogenesis poses two unique problems. First, these bacteria must exploit their host cells enough to thrive, but not so much that the host cell is prematurely destroyed. Second, while the intracellular environment is rife with valuable nutrients and compounds, it is also a harsh environment for invaders. For these reasons, bacterial pathogens and their toxins often quickly target the cell's crucial or conserved regulatory mechanisms with high precision and potency, making them valuable tools to study, and often discover important cell biological regulatory processes (Theriot, 1995; Welch, 2015).

Indeed, insights from studying intracellular bacterial pathogenesis have been profound. For example, initial observations of the rocket-like bacterial movement seen during *Shigella flexneri* and *Listeria monocytogenes* infections lead to the discovery of the Arp2/3 complex and the WASP family of proteins, crucial actin-nucleating factors in metazoan cell biology (Welch et al., 1998, 1997). In addition, studies of *Salmonella* pathogenesis have resulted in crucial insights regarding selectivity in autophagy (Thurston et al., 2009), and numerous pathogens have provided important insights into membrane trafficking (Asrat et al., 2014). Intracellular bacterial pathogens remain a treasure trove for cell biological discoveries, consistently revealing host-pathogen dynamics.

1.2 *Legionella pneumophila*

This study is focused on the pathogenesis of *Legionella pneumophila*. *Legionella pneumophila* (*L.p.*) is an intracellular bacterial pathogen that has proved to be a master manipulator of its eukaryotic hosts. It is the causative agent of Legionnaires' disease, a severe pneumonia that affects immunocompromised patients upon exposure to contaminated aerosols. In the context of

human disease, *L.p.* infects alveolar macrophages, but its preferred hosts include a wide range of protozoa, demonstrating the bacterium's ability to manipulate conserved eukaryotic processes to promote pathogenesis (Best and Kwaik, 2018; Gomez-Valero and Buchrieser, 2019). Phagocytosis by a permissive host cell triggers a complex pathogenic program in which *L.p.* avoids clearance by the endolysosomal system and instead remodels its plasma membrane-derived phagosome into an endoplasmic reticulum (ER)-like compartment called the *Legionella*-containing vacuole (LCV) (Hubber and Roy, 2010) (**Figure 1.1**). *L.p.* pathogenesis requires an enormous arsenal of ~330 bacterial proteins (effectors), which *L.p.* injects into the host cell cytosol with its Dot/Icm type IV secretion system (T4SS). By virtue of its mastery of the intracellular environment, *L.p.* and its effectors have emerged as powerful tools to study the molecular mechanisms of modulated host cell processes and to identify novel targets of pathogen manipulation more broadly (Cornejo et al., 2017; Noack and Mukherjee, 2020; Qiu and Luo, 2017a). For instance, *L.p.* studies have uncovered entirely novel regulatory mechanisms that modulate protein synthesis and folding (Moss et al., 2019; Treacy-Abarca and Mukherjee, 2015), conventional and unconventional modes of vesicular transport (Camus et al., 2019; Levin et al., 2016; Mukherjee et al., 2011), and phagocytosis (Jeng et al., 2019). Numerous *L.p.* effectors are known to regulate host cell proteins through conventional post-translational modifications (PTMs) such as phosphorylation, ubiquitination, and methylation (Michard and Doublet, 2015). *L.p.* also uses novel PTMs, such as phosphocholination (Mukherjee et al., 2011), and can catalyze non-canonical protein phosphoribosyl-ubiquitination with secreted ubiquitin ligases (Bhogaraju et al., 2016; Kalayil et al., 2018; Qiu et al., 2016; Wang et al., 2018). Importantly, since many aspects of *L.p.*-mediated pathogenesis, including the functions and targets of most effectors, remain elusive (Qiu and Luo, 2017a), studying the effects of these effector proteins on host cell pathways offers a great potential for the discovery of novel pathogenic and cell biological mechanisms.
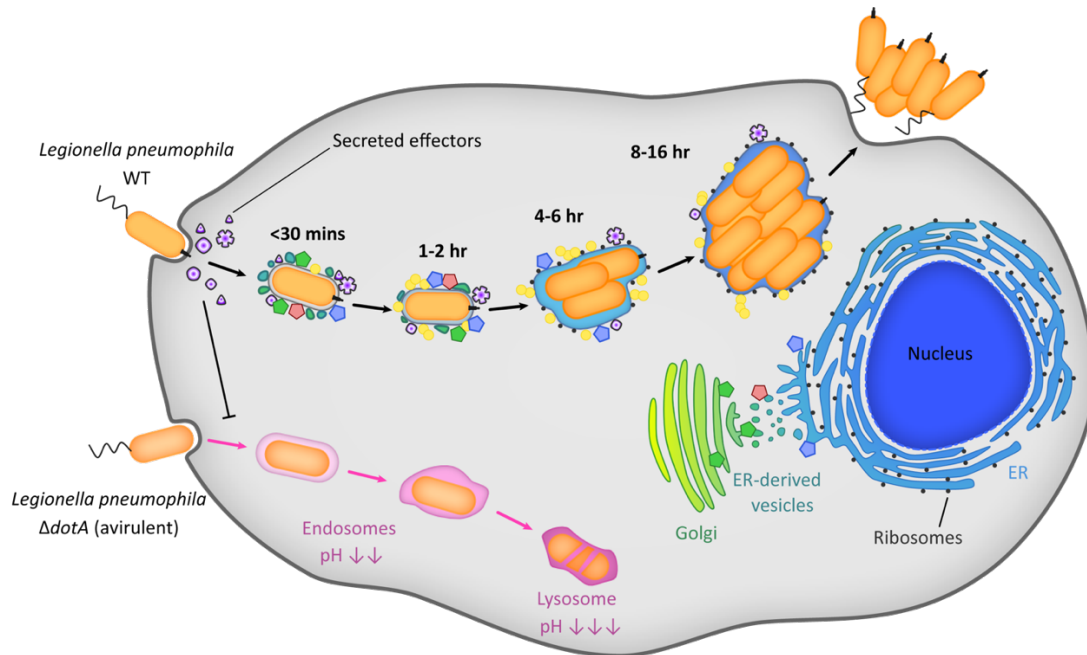
Figure 1.1: Life cycle of *Legionella pneumophila*. *L. pneumophila* establishes an ER-like niche for itself, deemed the Legionella- containing vacuole (LCV), in a matter of hours. It secretes over 330 effector proteins throughout infection to manipulate host pro cesses to its advantage. In grey font: proteins that serve as markers of the LCV at different stages of infection. L. pneumophila ΔdotA lack a functional T4SS secretion system and are degraded rapidly in the endolysosomal pathway.

1.3   Proteomic analysis of *Legionella*-infected cells

Thus far, a few studies have employed proteomic techniques to develop a broad understanding of targets in the host cell during *L.p.* pathogenesis. Focused research on the proteome of the LCV purified from macrophages or *Dictyostelium discoideum* has identified a strong recruitment of endosomal and secretory traffic markers, mitochondrial and metabolic proteins, and numerous GTPases from the Ras superfamily, such as Rab1, Rab5, and Rap1 (Bruckert and Kwaik, 2015; Schmölders et al., 2017; Urwyler et al., 2009). While these findings have provided valuable insights, they offer a limited view by concentrating solely on the LCV-localized proteome, leaving global proteomic changes obscured. One study that attempted to develop a global understanding of changes in the host ubiquitinome during infection revealed that *L.p.* hijacks the ubiquitin-proteasome system to suppress innate immunity pathways and mTOR signaling during infection

(Ivanov and Roy, 2013). However, this research relied on stable cell lines expressing tagged ubiquitin, which are susceptible to non-specific ubiquitination (Emmerich and Cohen, 2015; Peng et al., 2017). Contemporary ubiquitinomics has shifted towards diGlycine enrichment to detect endogenous ubiquitination events, avoiding the pitfalls of overexpression artifacts—a technique proven effective in analyzing host cell ubiquitinome changes during infections like *Salmonella Typhimurium* and *Mycobacterium tuberculosis* (Budzik et al., 2020; Fiskin et al., 2016) but not yet applied to *L.p.* infection. Moreover, a dynamic, temporal profile of host protein abundance and post-translational modifications (PTMs), including phosphorylation, is essential for a nuanced understanding of regulatory mechanisms, considering the distinct subsets of effectors operative during various infection stages (Oliva et al., 2018).

We therefore performed a time-dependent global proteomic analysis measuring changes in host protein abundance, phosphorylation, and ubiquitination during *L.p.* infection. To distinguish between effector-dependent and -independent effects on the proteome, we used the *L.p.* WT strain and the isogenic *ΔdotA* mutant, which lacks a T4SS and is cleared via the endolysosomal pathway. We chose HEK293 cells stably expressing the FcγRIIb receptor (HEK293 FcγR cells), as HEK293 FcγR have been used extensively in previous studies of *L.p.* pathogenesis and efficiently internalize antibody-opsonized *L.p.* (Black et al., 2019; Moss et al., 2019; Mukherjee et al., 2011; Qiu et al., 2016; Treacy-Abarca and Mukherjee, 2015). Cells were left uninfected or infected with either wild-type (WT) *L.p.* or the *ΔdotA* strain (**Fig 1.2A**). For temporal resolution, infected cells were lysed at 1 or 8 hours post infection (hpi). Extracted proteins from these five conditions (uninfected control, WT 1hr, WT 8hr, *ΔdotA* 1hr, *ΔdotA* 8hr) were trypsinized and separated into 3 aliquots: (1) for the analysis of protein abundance, (2) for the analysis of phosphorylated peptides, or (3) for the analysis of ubiquitinated peptides by diglycine (diGly) remnant enrichment. While diGly enrichment also captures peptides modified with the ubiquitin-like proteins NEDD8 and ISG15, these peptides make up only a small fraction of the total enriched

pool (~5%) (Kim et al., 2011). It is important to note that diGly enrichment can identify only canonically ubiquitinated sites; phosphoribosyl ubiquitination mediated by non-canonical ubiquitin ligase effectors is not detected, nor can ubiquitin chain length at a detected site be determined. Peptides were then subjected to mass spectrometric analysis and quantified with appropriate adjustments made based on quality control metrics (see **Materials and Methods**, **Supplemental File 1**, **Supplementary Figure 1.1**). Peptide intensities between all three biological replicates per condition showed a robust reproducibility with correlation coefficients ranging from 0.79 to 0.93 (**Supplementary Figure 1.1**). To capture the overall similarities and differences between the five experimental conditions, we performed a Principal Component Analysis (PCA). PCA identified a larger correlation between uninfected control and Δ*dotA* relative to WT (**Fig 1.2B**). This indicates that, as expected, most changes in the proteome during infection are driven by effector secretion from *L.p.* WT.
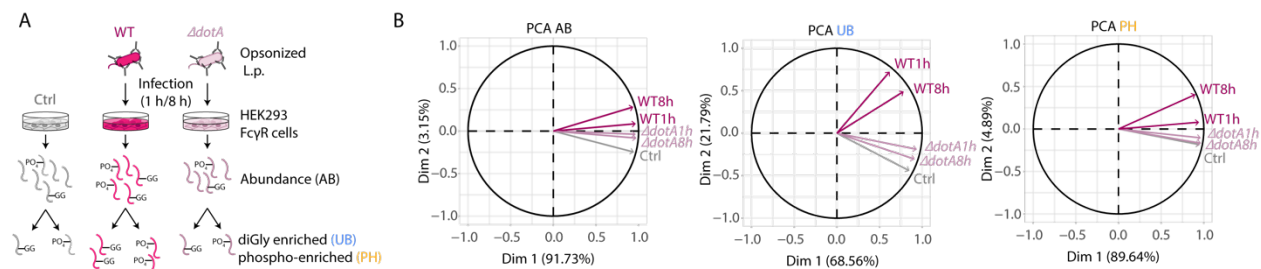
Figure 1.2: Proteomic analysis of *Legionella*-infected cells. A) Experimental design. HEK293 FcγR cells were left uninfected (Ctrl) or infected with the opsonized *L.p.* WT or Δ*dotA* strain for 1h or 8h (MOI 100). After tryptic digestion, extracted proteins were directly subjected to MS/MS analysis (abundance, AB) or further enriched for ubiquitinated (UB) and phosphorylated (PH) peptides prior to analysis. **(B)** Principal Component analysis of normalized MS Intensities of experimental conditions (control, Δ*dotA*-1h, Δ*dotA*-8h, WT-1h, WT-8h). PC1 and PC2 captured most of the variability. Loading variables are represented as vectors. The smaller angle between control and the mutant time points (Δ*dotA*-1h, Δ*dotA*-8h) implies a larger positive correlation between them, as oppose to a lower correlation (larger angle) between the Control and the WT strain, especially for the later time point (WT-8h).

To compare changes in protein abundance, ubiquitination, or phosphorylation between the different samples (Ctrl, WT, Δ*dotA*), we calculated the Log$_2$ fold changes (Log2FC), corresponding p-values, and adjusted p-values of all proteins/proteoforms between WT-infected

and uninfected cells (WT-Control), *ΔdotA*-infected and uninfected cells (*ΔdotA*-Control), and WT- and *ΔdotA*-infected cells (WT-*ΔdotA*) at both timepoints using the artMS Bioconductor package (**Supplementary File 2**) (Jimenez-Morales et al., 2019). As expected, we encountered several quantifications in which a peptide was uniquely identified in only one of the conditions while missed in the other one ("missing values", e.g. a ubiquitinated peptide detected during WT but not *ΔdotA* infection). In our analyses, we largely consider these missing value events to be biologically significant, particularly in our PTM datasets, because *L.p.* secretes numerous ubiquitin ligases, deubiquitinases, kinases, and phosphatases with unknown targets (Michard and Doublet, 2015; Qiu and Luo, 2017b). To ensure that these events were factored into our analyses when appropriate, we used a suitable imputation strategy (see **Materials and Methods**) (Webb-Robertson et al., 2015).

The following chapters contain two distinct analyses of the proteomic datasets and two independent lines of research that arose from these analyses. Each chapter is written as a full and complete manuscript. In **Chapter 2**, the proteomic infection signature of WT *L.p.* is compared to that of Δ*dotA L.p.* for all three proteomic datasets (abundance, phosphorylation, ubiquitination). By using Log2FC(WT/Δ*dotA*) values as the basis of our analyses, we enrich for proteomic changes driven by effector secretion rather than the presence of the bacterium itself (e.g. a protein that increases in abundance in response to both WT and Δ*dotA* infections will have a Log2FC close to 0 and therefore will be considered insignificant in downstream analyses). From these analyses, we identify the mitochondrial proteostasis network as a novel target of *L.p.* effectors. In response to infection with *L.p.*, the abundance, phosphorylation, and ubiquitination of mitochondrial proteins involved in mitochondrial protein import, oxidative phosphorylation, gene expression and protein folding were strongly regulated in a T4SS-dependent manner. Changes in the mitochondrial proteome during infection match patterns observed in a mitochondrial stress response (MSR) activated during proteotoxic stress, such as the mitochondrial unfolded protein

response (UPR^{mt}). Although we find several transcriptional upregulations consistent with the induction of a MSR, we determine that *L.p.* induces their upregulation through non-canonical mechanisms.

In **Chapter 3**, proteomic analyses are primarily focused on the ubiqutinomics, and the relationship between changes in protein ubiquitination and changes in abundance. Importantly, proteomic analyses were performed comparing WT *L.p.* infected cells and ΔdotA *L.p.* infected cells to uninfected cells, avoiding some of the pitfalls of using Log2FC(WT/ΔdotA) values for analysis (discussed further in the **Chapter 2, Additional Data and Discussion** section). From these analyses, we determine that *L.p.*-induces numerous ubiquitinations on Ras superfamily small GTPases, and further experimentation is performed to determine that *L.p.* exclusively ubiquitinates Ras small GTPases recruited to the membrane of the LCV through the activity of the secreted effectors SidC and SdcA.

1.4   Materials and Methods

1.4.1   Cell Lines

HEK293 cells (female) stably expressing the Fcγ receptor IIb (HEK293 FcγR cells),were cultured in Dulbecco's Modified Eagle's Medium (DMEM, GIBCO) containing 10% fetal bovine serum (FBS, VWR) at 37°C and 5% CO_2. These cell lines were gifts from the lab of Dr. Craig Roy at Yale University.

1.4.2   Bacterial strains and plasmids

Experiments were performed with *Legionella pneumophila* serogroup 1, strain Lp01. Avirulent T4SS-null strains (*ΔdotA*) were derived as previously described (Berger et al., 1994; Berger and Isberg, 1993). *L. pneumophila* strains were grown on Charcoal Yeast Extract (CYE) agar plates or AYE broth supplemented with ($FeNO_3$ 0.135g/10mL) and cysteine (0.4g/10mL).

1.4.3   Infection of cultured mammalian cells with L.p.

Infections with *L.p.* were performed as previously described (Treacy-Abarca and Mukherjee, 2015). *L.p.* heavy patches grown for 48 h on CYE plates were either used directly for infection, or for overnight liquid cultures in AYE medium until reaching an OD600 of 3. *L.p.* from the overnight culture was enumerated and the appropriate amount was opsonized with *L.p.*-specific antibodies at a dilution of 1:2000 in cell growth medium for 20 min. HEK293 FcγR were grown on poly-lysine coated cell culture plates to a confluency of 80% and infected with the *L.p.* WT strain or the isogenic Δ*dotA* mutant strain at a multiplicity of infection (MOI) of 100. The infection was synchronized by centrifugation of the plates at 1000xg for 5 min. To prevent internalization of any remaining extracellular bacteria at later timepoints, cells were washed three times with warm PBS after 1 h of infection and fresh growth medium was added. Cells were collected for down-stream processing at the indicated timepoints. Uninfected samples used as controls for infection experiments were mock-infected using media and opsonization antibody only.

1.4.4   Sample preparation for proteomics analysis

HEK293 FcγR infected for 1 h or 8 h with the *L.p.* WT strain Lp01 or the isogenic *ΔdotA* mutant were infected at an MOI of 100. Uninfected HEK293 FcγR cells were included as a control. Cells were washed with ice-cold PBS, collected and the pellet was frozen at -80°C. Cell pellets were lysed by probe sonication in three pulses of 20% amplitude for 15 s in a lysis buffer consisting of: 8 M urea, 150 mM NaCl, 100 mM ammonium bicarbonate, pH 8; added per 10 ml of buffer: 1 tablet of Roche mini-complete protease inhibitor EDTA free and 1 tablet of Roche PhosSTOP. In order to remove insoluble precipitate, lysates were centrifuged at 16,100 g at 4°C for 30 min. A Bradford Assay (Thermo) was performed to measure protein concentration in cell lysate supernatants. 6 mg of each clarified lysate was reduced with 4 mM tris(2-carboxyethyl)phosphine for 30 min at room temperature and alkylated with 10 mM iodoacetamide for 30 min at room temperature in the dark. Remaining alkylated agent was quenched with 10 mM 1,4-dithiothreitol for 30 min at room temperature in the dark. The samples were diluted with three starting volumes of 100 mM ammonium bicarbonate, pH 8.0, to reduce the urea concentration to 2 M. Samples were incubated with 50 µg of sequencing grade modified trypsin (Promega) and incubated at room temperature with rotation for 18 hr. The sample pH was reduced to approximately 2.0 by the addition of 10% trifluoroacetic acid (TFA) to a final concentration of 0.3% trifluoroacetic acid. Insoluble material was removed by centrifugation at 16,000 g for 10 min. Peptides were desalted using SepPak C18 solid-phase extraction cartridges (Waters). The columns were activated with 1 ml of 80% acetonitrile (I), 0.1% TFA, and equilibrated 3 times with 1 ml of 0.1% TFA. Peptide samples were applied to the columns, and the columns were washed 3 times with 1 ml of 0.1% TFA. Peptides were eluted with 1.2 ml of 50% I, 0.25% formic acid. Peptides were divided for global protein analysis (10 µg) or diGly-enrichment (remaining sample), and lyophilized.

1.4.5   diGlycine peptide enrichment by immunoprecipitation

Peptide samples were subjected to ubiquitin remnant immunoaffinity. 10 uL of PTMScan® Ubiquitin Remnant Motif (K-ε-GG) Antibody Bead Conjugate purification (Cell Signaling) slurry

was used per 1 mg peptide sample. Ubiquitin remnant beads were washed twice with IAP buffer, then split into individual 1.7 mL low bind tubes (Eppendorf) for binding with peptides. Peptides were dried with a centrifugal evaporator for 12 hours to remove TFA in the elution. The lyophilized peptides were resuspended in 1 ml of IAP buffer (50 mM 4- morpholinepropnesulfonic acid, 10 mM disodium hydrogen phosphate, 50 mM sodium chloride, pH 7.5). Peptides were sonicated and centrifuged for 5 minutes at 16,100g. The soluble peptide supernatant was incubated with the beads at 4°C for 90 minutes with rotation. Unbound peptides were separated from the beads after centrifugation at 700g for 60 seconds. Beads containing peptides with di-glycine remnants were washed twice with 500 μL of IAP buffer, then washed twice with 500 μL of water, with a 700g 60s centrifugation to allow the collection of each wash step. Peptides were eluted twice with 60 μL of 0.15% TFA. Di-glycine remnant peptides were desalted with UltraMicroSpin C18 column (The Nest Group). Desalted peptides were dried with a centrifugal adaptor and stored at -20°C until analysis by liquid chromatograph and mass spectrometry.

1.4.6   *Phosphopeptide enrichment by immobilized metal affinity chromatography*

Iron nitriloacetic acid (NTA) resin were prepared in-house by stripping metal ions from nickel nitroloacetic acid agarose resin with 100 mM ethylenediaminetetraacetic acid, pH 8.0 four times. Resin was washed twice with water and 100 mM iron(III) chloride was applied four times. The iron-NTA resin was washed twice with water and once with 0.5% formic acid. Iron- NTA beads were resuspended in water to create a 25% resin slurry. 60 μl of Fe-NTA resin slurry was transferred to individual Silica C18 MicroSpin columns (The Nest Group) pre-equilibrated with 100 μl of 80% CAN, 0.1% TFA on a vacuum manifold. Subsequent steps were performed with the Fe-NTA resin loaded above the Silica C18 columns. Dry peptide samples were resuspended in a solution of 200 μl 75% I 0.15% TFA. Peptide samples were mixed twice with the Fe-NTA resin, allowing the peptides to incubate for 2 minutes between each mixing step. The resin was rinsed four times with 200 μl of 80% I, 0.1% TFA. In order to equilibrate the columns, 200 μl of 0.5% formic acid was applied twice to the resin and columns. Peptides were eluted from the resin onto

the C18 column by mixing and incubating the Fe-NTA resin with 200 µl of 500 mM potassium phosphate, pH 7.0 for 2 minutes. The elution step was repeated once. Peptides bound to the C18 column were washed three times with 200 µl of 0.5% formic acid. The C18 columns were removed from the vacuum manifold and eluted twice by centrifugation at 1000g with 75 µl of 50% I, 0.25% formic acid. Peptides were dried with a centrifugal adaptor and stored at -20˚C until analysis by liquid chromatograph and mass spectrometry.

1.4.7   Mass spectrometry data acquisition and processing

Samples were resuspended in 4% formic acid, 4% acetonitrile solution, separated by a reversed-phase gradient over a nanoflow column (360 µm O.D. x 75 µm I.D.) packed with 25 cm of 1.8 µm Reprosil C18 particles with (Dr. Maisch), and directly injected into an Orbitrap Fusion Lumos Tribrid Mass Spectrometer (Thermo). Total acquisition times were 120 min for protein abundance, 100 min for phosphorylation, and 70 min for ubiquitylation analyses. Specific data acquisition settings are detailed in **Supplemental File 3**. Raw MS data were searched with MaxQuant against both the human proteome (UniProt canonical protein sequences downloaded January 11, 2016) and the *Legionella Pneumophila Philadelphia* proteome (downloaded July 17, 2017). Peptides, proteins, and PTMs were filtered to 1% false discovery rate in MaxQuant (Cox et al., 2014). Principal Component analysis of normalized MS Intensities of experimental conditions (control, Δ*dotA*-1h, Δ*dotA*-8h, WT-1h, WT-8h) was performed using the factoextra R package as implemented by the artMS bioconductor package. The plot illustrates the relationship between the variables (conditions) and the principal components, where each variable is represented as a vector, and the direction and length of the vectors indicate how each variable contributes to the two principal components. If two vectors are close together indicates a strong positive correlation between those two variables, i.e. they contribute to the principal components in a similar way. Statistical analysis of quantifications obtained from MaxQuant was performed with the artMS Bioconductor package (version 0.9) (Jimenez-Morales et al., 2019). Each dataset (proteome and ubiquitinome) was analyzed independently. Quality control plots were generated using the artMS

quality control functions. The site-specific relative quantification of posttranslational modifications required a preliminary step consisting of providing the ptm-site/peptide-specific annotation ("artmsProtein2SiteConversion()" function). artMS performs the relative quantification using the MSstats Bioconductor package (version 3.14.1) (Choi et al., 2014). Contaminants and decoy hits were removed. Samples were normalized across fractions by median-centering the Log_2-transformed MS1 intensity distributions (**Supplementary Fig 1.1B**). **Imputation strategy:** Log2FC for protein/sites with missing values in one condition but found in ≥ 2 biological replicates of the other condition of any given comparison were estimated by imputing intensity values from the lowest observed MS1-intensity across sample peptides (Webb-Robertson et al., 2015); p-values were randomly assigned between 0.05 and 0.01 for illustration purposes.

1.5   Supplementary Figures
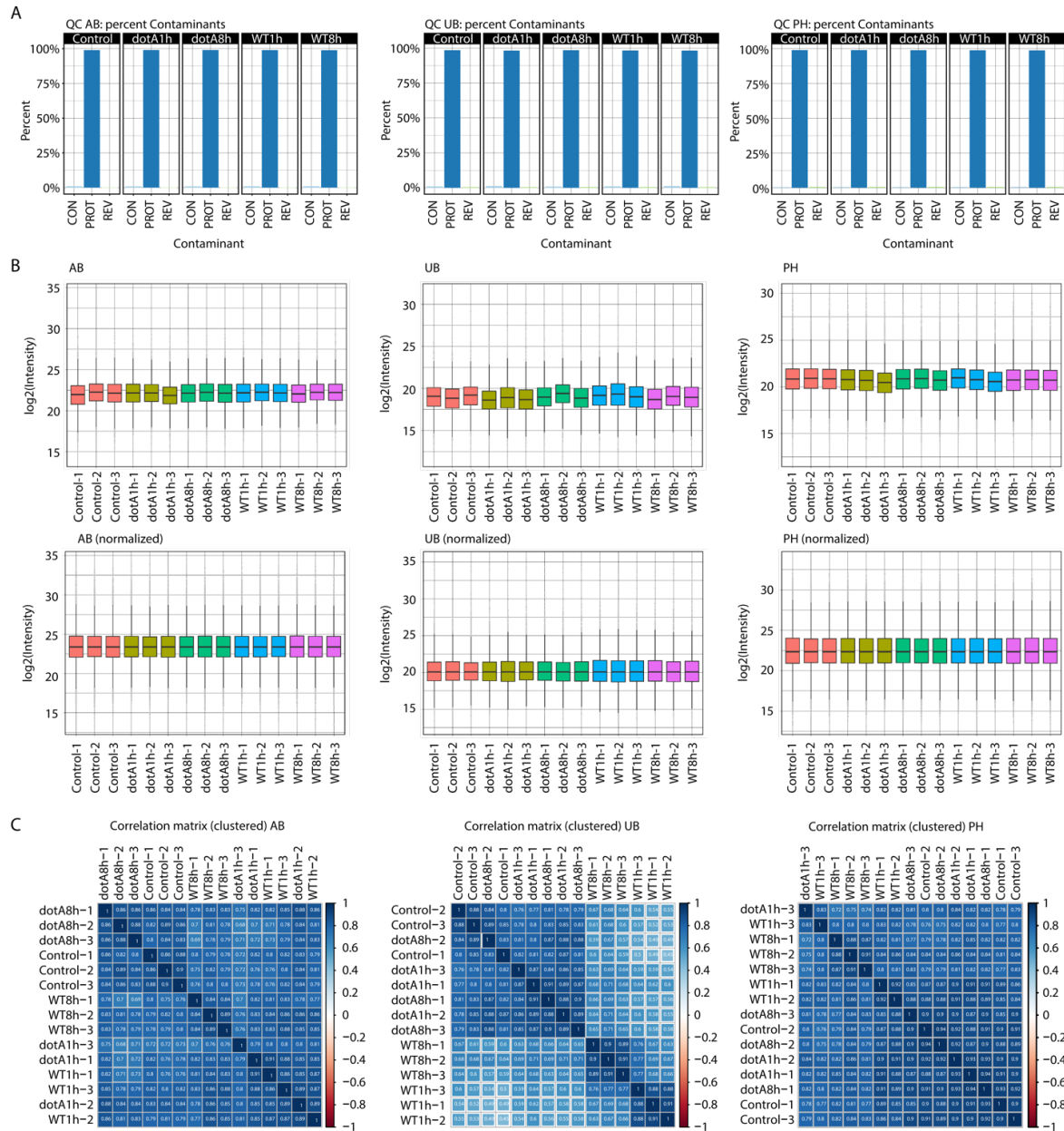
Supplementary Figure 1.1: Quantification and quality control plots of proteomics data. Quality control plots for each dataset (AB, UB, PH) were generated using the artMS Bioconductor package (version 0.9) (Jimenez-Morales et al., 2019). **(A)** Percent of contaminants (CON), proteins (PROT) and reversed sequences (REV) in each experimental condition (control, dotA-1h, dotA-8h, WT-1h, WT-8h) were quantified to adjust the false-discovery-rate (FDR). **(B)** Samples were normalized across fractions by median-centering the Log2-transformed MS1 intensity distributions. **(C)** Correlation matrices showing the clustering of the different experimental conditions.

Chapter 2: Dynamic proteomic profiling of Legionella pneumophila infection unveils modulation of the host mitochondrial stress response pathway.

2.1   Abstract

The intracellular bacterial pathogen *Legionella pneumophila* (*L.p.*) secretes ~330 bacterial effector proteins into the host cell that interfere with numerous cellular pathways and often regulate host cell proteins through post-translational modifications. Many aspects of *L.p.*-mediated pathogenesis, including the functions and targets of most effectors, remain elusive. To obtain a global overview of host cell rewiring and potential targets of these effectors, we analyzed the host cell proteome for changes in protein abundance, phosphorylation, and ubiquitination during *L.p.* infection. Our analysis reveals dramatic spatiotemporal changes in the host cell proteome that are dependent on the secretion of bacterial effectors. Strikingly, we show that *L.p.* substantially reshapes the mitochondrial proteome and induces a mitochondrial stress response with many similarities to the mitochondrial unfolded protein response (UPR^{mt}). *L.p.* modulates downstream adaptive responses to mitochondrial stress by blocking the translation of transcription factors ATF4 and CHOP while allowing for the translation of ATF3. To our knowledge, this is the first evidence of manipulation of the UPR^{mt} by a bacterial pathogen in mammalian cells.

2.2   Introduction

Legionella pneumophila (*L.p.*) is a gram-negative, intracellular bacterial pathogen, and natural parasite to evolutionarily diverse amoeba (Best and Kwaik, 2018; Qiu and Luo, 2017a). Evolution of a broad host range has conferred an ability for *L.p.* to infect humans as a dead-end host, in

which it can cause a severe form of pneumonia known as Legionnaires' disease. Inhalation of contaminated aerosols and subsequent phagocytosis by alveolar macrophages triggers a complex pathogenic program in which *L.p.* avoids clearance in the endolysosomal system and instead remodels its plasma membrane (PM)-derived phagosome into an endoplasmic reticulum (ER)-like compartment called the *Legionella*-containing vacuole (LCV). *L.p.* pathogenesis requires an enormous arsenal of ~330 bacterial proteins (effectors), which *L.p.* injects into the host cell cytosol with its Dot/Icm type IV secretion system (T4SS). By virtue of its mastery of the intracellular environment, *L.p.* and its effectors have emerged as powerful tools to study the molecular mechanisms of modulated host cell processes and to identify novel targets of pathogen manipulation more broadly (Cornejo et al., 2017; Noack and Mukherjee, 2020; Qiu and Luo, 2017a). For instance, *L.p.* studies have uncovered entirely novel regulatory mechanisms that modulate protein synthesis and folding (Moss et al., 2019; Treacy-Abarca and Mukherjee, 2015), conventional and unconventional modes of vesicular transport (Camus et al., 2019; Levin et al., 2016; Mukherjee et al., 2011), and phagocytosis (Jeng et al., 2019). Numerous *L.p.* effectors are known to regulate host cell proteins through conventional post-translational modifications (PTMs) such as phosphorylation, ubiquitination, and methylation (Michard and Doublet, 2015). *L.p.* also uses novel PTMs, such as phosphocholination (Mukherjee et al., 2011), and can catalyze non-canonical protein phosphoribosyl-ubiquitination with secreted ubiquitin ligases (Bhogaraju et al., 2016; Kalayil et al., 2018; Qiu et al., 2016; Wang et al., 2018). Importantly, since many aspects of *L.p.*-mediated pathogenesis, including the functions and targets of most effectors, remain elusive (Qiu and Luo, 2017a), studying the effects of these proteins on host cell pathways offers a great potential for the discovery of novel pathogenic and cell biological mechanisms.

A few targeted proteomics studies have been performed in order to identify proteins recruited to the LCV and host factors required for *L.p.* replication (Bruckert and Kwaik, 2015; Ivanov and Roy, 2013; Schmölders et al., 2017; Urwyler et al., 2009). For instance, the ubiquitinome of *L.p.* infected

cells revealed many interesting insights into the regulation of innate immunity pathways and mTOR signaling during infection (Ivanov and Roy, 2013). However, this approach relied on stable cell lines expressing tagged ubiquitin, which are prone to non-specific ubiquitination (Emmerich and Cohen, 2015; Peng et al., 2017). Past studies have focused on the proteome of the purified LCV (Bruckert and Kwaik, 2015; Schmölders et al., 2017; Urwyler et al., 2009), however, global proteomic changes in the host cell remained elusive. Lastly, because distinct subsets of effectors function during early and late stages of infection, a dynamic, temporal profile of host protein abundance and PTM changes was needed to more deeply understand the regulatory mechanisms at play during infection.

We therefore performed a time-dependent global proteomic analysis measuring changes in host protein abundance, phosphorylation, and ubiquitination during *L.p.* infection. To distinguish between effector-dependent and -independent effects on the proteome, we used the *L.p.* WT strain and the isogenic *ΔdotA* mutant, which lacks a T4SS and is cleared via the endolysosomal pathway. Our analysis provides a comprehensive resource that highlights T4SS-dependent, spatiotemporal changes in the host cell proteome during *L.p.* infection. Here, we identify the mitochondrial proteostasis network as a novel target of *L.p.* effectors. In response to infection with *L.p.*, the abundance, phosphorylation, and ubiquitination of mitochondrial proteins involved in mitochondrial protein import, oxidative phosphorylation, gene expression and protein folding were strongly regulated in a T4SS-dependent manner. Changes in the mitochondrial proteome during infection match patterns observed in a mitochondrial stress response (MSR) activated during proteotoxic stress, such as the mitochondrial unfolded protein response (UPR^{mt}). In accordance with an active MSR, we find that infection induces transcription of ATF3, ATF4, ATF5, CHOP, and GADD34, classic downstream targets of the integrated stress response (ISR) (Mottis et al., 2019). Paradoxically, we find that induction of these genes is not antagonized by the ISR inhibitor ISRIB, suggesting that mitochondrial stress may overpower ISRIB, or that gene upregulation may occur

through an ISR-independent mechanism. Furthermore, we find that *L.p.* infection blocks the translation of ATF4 and CHOP but permits the translation of ATF3, potentially modulating a host cell adaptive response to mitochondrial stress. In summary, our data serve as an invaluable resource to determine host cell organelles and pathways rewired during infection, and highlight *L.p.* as an inducer and manipulator of mitochondrial stress responses.

2.3   Results

2.3.1   *L.p. infection induces T4SS-dependent proteomic changes in the host cell*

To identify novel host cell components and pathways targeted during *L.p.* infection, we performed a global proteomics analysis of protein abundance, phosphorylation, and ubiquitination in *L.p.*-infected HEK293 cells stably expressing the FcγR receptor (HEK293 FcγR cells, **Fig 2.1A**). Like amoeba, HEK293 FcγR cells are deficient in innate immune sensors and therefore serve as excellent tools to uncover conserved eukaryotic pathways targeted by *L.p.* effectors. HEK293 FcγR have been used extensively in previous studies of *L.p.* pathogenesis, and efficiently internalize antibody-opsonized *L.p.*(Bhogaraju et al., 2019; Black et al., 2019; Gan et al., 2020; Liu et al., 2017; Moss et al., 2019; Mukherjee et al., 2011; Qiu et al., 2016; Shin et al., 2020; Treacy-Abarca and Mukherjee, 2015). To control for effector-dependent and -independent changes, we utilized wild-type *L.p.* bacteria (WT) and the isogenic *L.p. ΔdotA* strain that lacks a functional secretion system but exposes the cell to the same pathogen-associated molecular patterns (**Fig 2.1A**). Cells were infected with either of the *L.p.* strains or left uninfected (Ctrl) and lysed at 1 or 8 hours post infection (hpi). The extracted proteins of three biological replicates were trypsinized and separated into 3 aliquots: (1) for the analysis of protein abundance (AB), (2) for the analysis of phosphorylated peptides (phosphoproteome, PH), or (3) for the analysis of ubiquitinated peptides by diglycine (diGly) remnant enrichment, which is found upon protein modification with ubiquitin or the ubiquitin-like proteins NEDD8 and ISG15 (hereafter referred to

as ubiquitinome, UB) (**Fig 2.1A**) (Kim et al., 2011; Swaney and Villén, 2016; Udeshi et al., 2012). Peptides were then subjected to mass spectrometric analysis and quantified (**Supplementary File 1** and **Supplementary Figure 2.1A-B**). Peptide intensities in biological replicates showed a robust reproducibility with correlation coefficients ranging from 0.79 to 0.93 (**Supplementary File 1** and **Supplementary Figure 2.1C**). We performed a Principal Component Analysis (PCA) to identify the overall similarities between the different conditions (control, *ΔdotA*-1h, *ΔdotA*-8h, WT-1h, WT-8h). Importantly, PCA results captured a larger correlation between control and *ΔdotA* time points relative to the WT time points in all proteomics datasets, especially in the ubiquitinome (**Fig 2.1B**). This indicates that most proteomic changes during infection are driven by effector secretion, and that the most dramatic host cell rewiring occurs in the ubiquitinome.
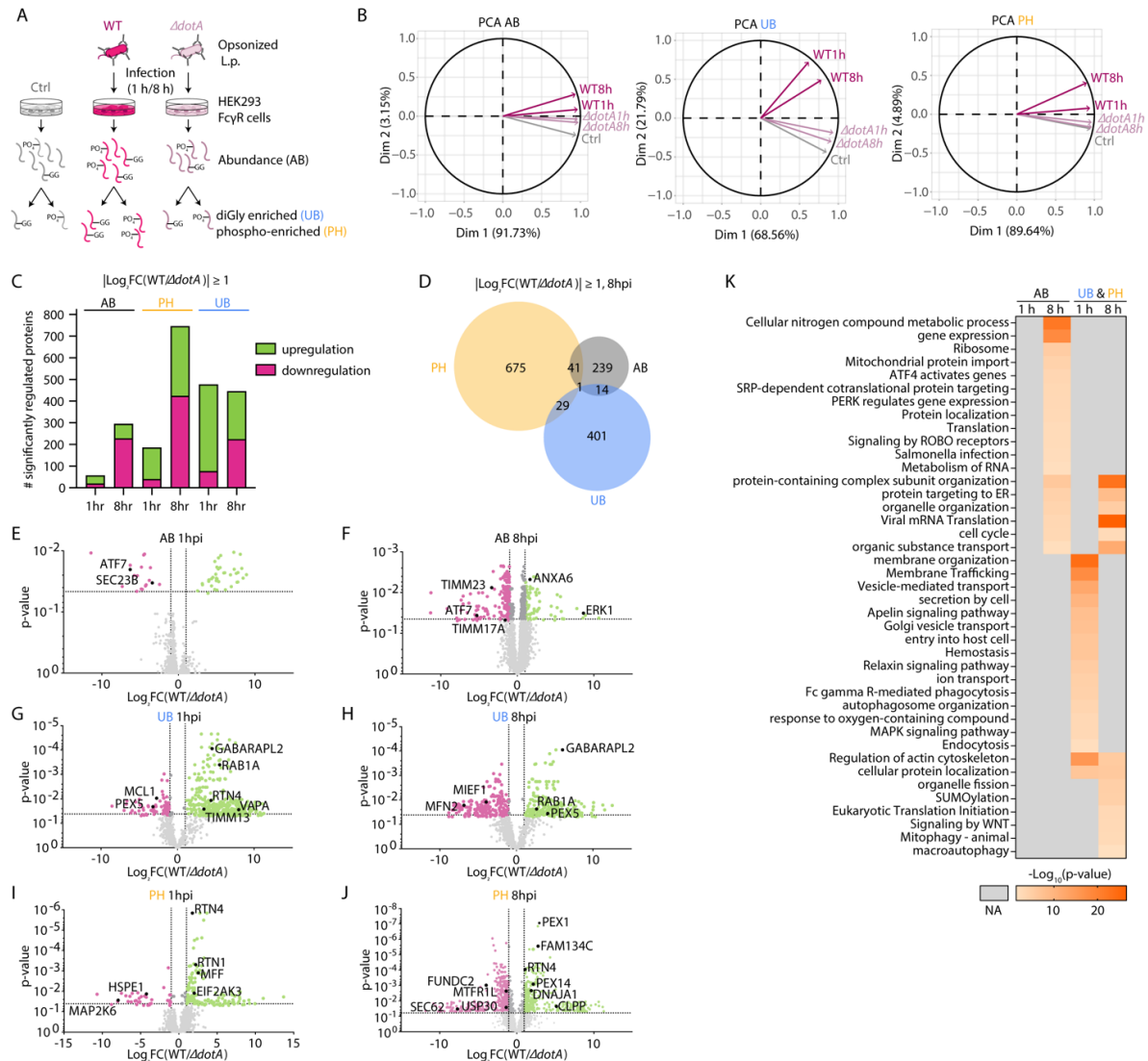
Figure 2.1: *L.p.* **infection induces T4SS-dependent proteomic changes in the host cell. (A)** Experimental design. HEK293 FcγR cells were left uninfected (Ctrl) or infected with the opsonized *L.p.* WT or *ΔdotA* strain for 1h or 8h (MOI 100). After tryptic digestion, extracted proteins were directly subjected to MS/MS analysis (abundance, AB) or further enriched for ubiquitinated (UB) and phosphorylated (PH) peptides prior to analysis. **(B)** Principal Component analysis of normalized MS Intensities of experimental conditions (control, *ΔdotA*-1h, *ΔdotA*-8h, WT-1h, WT-8h). PC1 and PC2 captured most of the variability. Loading variables are represented as vectors. The smaller angle between control and the mutant time points (*ΔdotA*-1h, *ΔdotA*-8h) implies a larger positive correlation between them, as oppose to a lower correlation (larger angle) between the Control and the WT strain, especially for the later time point (WT-8h). **(C)** Number of significantly regulated proteins in WT- *vs. ΔdotA*-infected cells (adj.-p-value ≤ 0.05, |Log_2FC| ≥ 1). Protein upregulations (abundance up, ubiquitination, or phosphorylation) are indicated in green, downregulations (abundance down, deubiquitination, or dephosphorylation) are indicated in purple. **(D)** Venn diagrams showing the overlap between significantly regulated proteins (adj.-p-value ≤ 0.05, |Log_2FC| ≥ 1) in the AB, UB and PH datasets in WT- *vs. ΔdotA*-infected cells (8hpi). *Figure caption continued on the next page.*

Figure caption continued from the previous page. **(E)-(J)** Volcano plots showing significantly up- (green dots) or down-regulated (purple dots) proteins in WT- *vs. ΔdotA*-infected cells (adj.-p-value ≤ 0.05, |Log$_2$FC(WT/*ΔdotA*)| ≥ 1). Grey dots: adj.-p-value > 0.05 and/or |Log$_2$FC(WT/*ΔdotA*)| < 1. Selected proteins are highlighted in black. (K) Gene ontology enrichment analysis of significantly regulated proteins in WT- *vs. ΔdotA*-infected cells (AB, or UB/PH combined) was performed with the g:Profiler g:GOSt tool (Raudvere et al., 2019). The heat map shows the most significantly overrepresented GO terms (Biological Processes, Reactome and KEGG pathways).

To compare changes in protein abundance, ubiquitination, or phosphorylation between the different samples (Ctrl, WT, *ΔdotA*), we calculated the Log$_2$ fold changes (Log$_2$FC), corresponding p-values, and adjusted p-values of all proteins/proteoforms between WT-infected and uninfected cells (WT/Ctrl), *ΔdotA*-infected and uninfected cells (*ΔdotA*/Ctrl), and WT- and *ΔdotA*-infected cells (WT/*ΔdotA*) at both timepoints using the artMS Bioconductor package (**Supplementary File 2**) (Jimenez-Morales et al., 2019). As expected, we encountered several quantifications in which a peptide was uniquely identified in only one of the conditions while missed in the other one ("missing values", e.g. a ubiquitinated peptide detected during WT but not *ΔdotA* infection). In our analyses, we largely consider these missing value events to be biologically significant, particularly in our PTM datasets, because *L.p.* secretes numerous ubiquitin ligases, deubiquitinases, kinases, and phosphatases with unknown targets (Michard and Doublet, 2015; Qiu and Luo, 2017b). To ensure that these events were factored into our analyses when appropriate, we used a suitable imputation strategy (see Methods) (Webb-Robertson et al., 2015). Broadly we found that WT *L.p.* induced hundreds of significant protein up- and downregulations (defined as protein with AB, UB, or PH change, |Log$_2$FC| ≥ 1, adj.-p-value ≤ 0.05) when compared to *ΔdotA L.p.* at both 1hpi and 8hpi (**Supplementary File 4** and **Fig 2.1C**). Importantly, proteins experiencing significant abundance, ubiquitination, or phosphorylation changes appear to be distinct populations, suggesting both that these PTMs do not lead to abundance changes during infection, and that abundance changes are not responsible for detected PTM changes (**Fig 2.1D**).

To understand how the secretion of *L.p.* effectors into the host cell reshapes its proteome, we first compared proteins with significant abundance regulation in WT vs. *ΔdotA*-infected cells (**Figs 2.1E** and **2.1F**). Early during infection (1hpi), few proteins experienced significant abundance changes (**Fig 2.1E** and **Supplementary File 4**). Of note were downregulations of several proteins, including the transcription factor ATF7 and SEC23B, a protein involved in ER-to-Golgi transport (**Fig 2.1E**). In contrast, the late host proteome response (8hpi) was characterized by a dramatic decrease in protein abundance in WT- *vs. ΔdotA*-infected cells (**Fig 2.1F** and **Supplementary File 4**). This result was expected as *L.p.* infection is known to inhibit host cell protein synthesis through the combined actions of bacterial effectors (Belyi et al., 2008, 2006; Cornejo et al., 2017; Fontana et al., 2011; Moss et al., 2019; Shen et al., 2009). However, a subset of these down-regulated proteins may also be actively degraded as part of the host cell response to infection, or by *L.p.* effectors such as bacterial ubiquitin ligases or proteases. Among the down-regulated proteins were TIMM23 and TIMM17, two crucial components of the inner mitochondrial membrane (IMM) protein import machinery. Strikingly, despite the general translation inhibition, the several proteins increased in abundance at this timepoint, suggesting that *L.p.* or the host may benefit from the selective translation of certain mRNAs (**Fig 2.1F** and **Supplementary File 4**). These proteins include the kinase ERK1, and the phospholipid-binding protein Annexin VI (**Fig 2.1F**).

We next compared the ubiquitinome and phosphoproteome in WT *vs. ΔdotA*-infected cells, we found that hundreds of ubiquitinated and phosphorylated proteins were differentially regulated upon WT infection when compared to the *ΔdotA* mutant at both infection timepoints (**Figs 2.1C, 2.1G-J** and **Supplementary File 4**). These proteins included known targets of *L.p.* effectors such as the ER-shaping proteins RTN4 and FAM134C, and the small GTPase RAB1 (Horenkamp et al., 2014; Kotewicz et al., 2017; Shin et al., 2020), but also novel hits such as proteins involved in mitochondrial protein import (TIMM13), mitochondrial dynamics and mitophagy (e.g. MIEF1,

MFN2, MTFR1L, FUND2C, GABARAPL2), peroxisomal proteins (e.g. PEX1, PEX5, PEX14) and the ER-resident UPR sensor EIF2AK3/PERK (**Figs 2.1G-J**). Strikingly, we note that the majority of imputations across the AB, PH, and UB datasets occurred in our ubiquitination dataset, in which almost 62% (1hpi) and 53% (8hpi) of significant ubiquitinations/deubiquitinations were imputed (**Supplementary Figure 2.1D**). This large quantity of imputations indicates unique and profound rewiring of the host-cell ubiquitinome during infection and is not entirely unsurprising given the many known and predicted secreted effector ubiquitin ligases and deubiquitinases (Qiu and Luo, 2017b).

To determine which biological processes and pathways were mainly affected upon *L.p.* infection in an T4SS-dependent manner, we performed a functional enrichment analysis of the significantly regulated proteins comparing WT *vs. ΔdotA*-infected cells (AB or UB/PH datasets combined). At the early infection timepoint, we did not find any significantly overrepresented terms in the AB dataset (**Fig 2.1K**). In contrast, at 8hpi, significantly regulated proteins were enriched for processes and pathways related to proteostasis. The UB/PH datasets showed significant overrepresentation of expected terms involved in *L.p.* entry into host cells at 1hpi (**Fig 2.1K**). At 8hpi, we found significantly enriched terms involved in organelle homeostasis. These results reflect the dynamic shift in biological processes and pathways targeted by *L.p.* in a T4SS-dependent manner during infection.

Taken together, *L.p.* rewires the host cell via changes in host cell protein abundance, ubiquitination, and phosphorylation. Using the *L.p.* WT strain and the *ΔdotA* mutant, we were able to differentiate between a general response to *L.p.* infection and an effector-driven, T4SS-dependent proteomic signature. Our analysis confirmed previously reported host proteins and pathways targeted by *L.p.,* and identified novel proteins/pathways regulated during *L.p.* infection.

2.3.2 Dynamic regulation of kinase activities during L.p. infection

Many cellular stress responses involve the activation of kinases through phosphorylation events. We used the open-source tool PhosFate Profiler (Ochoa et al., 2016) to infer differential host cell kinase activity in WT- *vs. ΔdotA*-infected cells based on the identified, significantly regulated phosphorylation sites. Visualization of the inferred kinase activities on the kinome tree with CORAL(Metz et al., 2018) revealed the regulation of all main kinase groups in response to *L.p.* WT infection, with the exception of the TK kinase family in which only few kinases were regulated (**Figs 2.2A, Supplementary Figure 2.2A** and **Supplementary File 5**). About one third of the kinases were differentially regulated at 1hpi and 8hpi, highlighting the dynamic nature of the kinase-mediated host cell response to the pathogen. For instance, cyclin-dependent kinase 2 (CDK2) showed increased predicted activity at 1hpi but decreased activity at 8hpi (**Figs 2.2A-B** and **Supplementary Figure 2.2A**). A similar trend was observed for BRSK2, a kinase involved in the regulation of cell cycle and ER-stress mediated apoptosis (Wang et al., 2012). At both infection timepoints, the kinase triad VRK1-PLK3-ERK7, which plays a role in Golgi disassembly (López-Sánchez et al., 2009), showed higher inferred activity in WT- *vs. ΔdotA*-infected cells (**Figs 2.2A-B** and **Supplementary Figure 2.2A**). Previous data had observed elevated MAPK activation during *L.p.* infection (Fontana et al., 2012; Shin et al., 2008). In agreement with this past work, our data showed elevated activity of the Jun kinase JNK2 at 1hpi and 8hpi. Accordingly, we observed the phosphorylation of its target c-Jun at serine 73 (Jaeschke et al., 2006; Kallunki et al., 1994) during the course of WT-infection, but not in *ΔdotA*-infected cells (**Fig 2.2C**). Holistically, a functional enrichment analysis of all kinases with predicted increased activity in WT *L.p.*-infected cells at both infection timepoints revealed the significant overrepresentation of pathways/processes involved in cell stress and organization (**Fig 2.2D**).
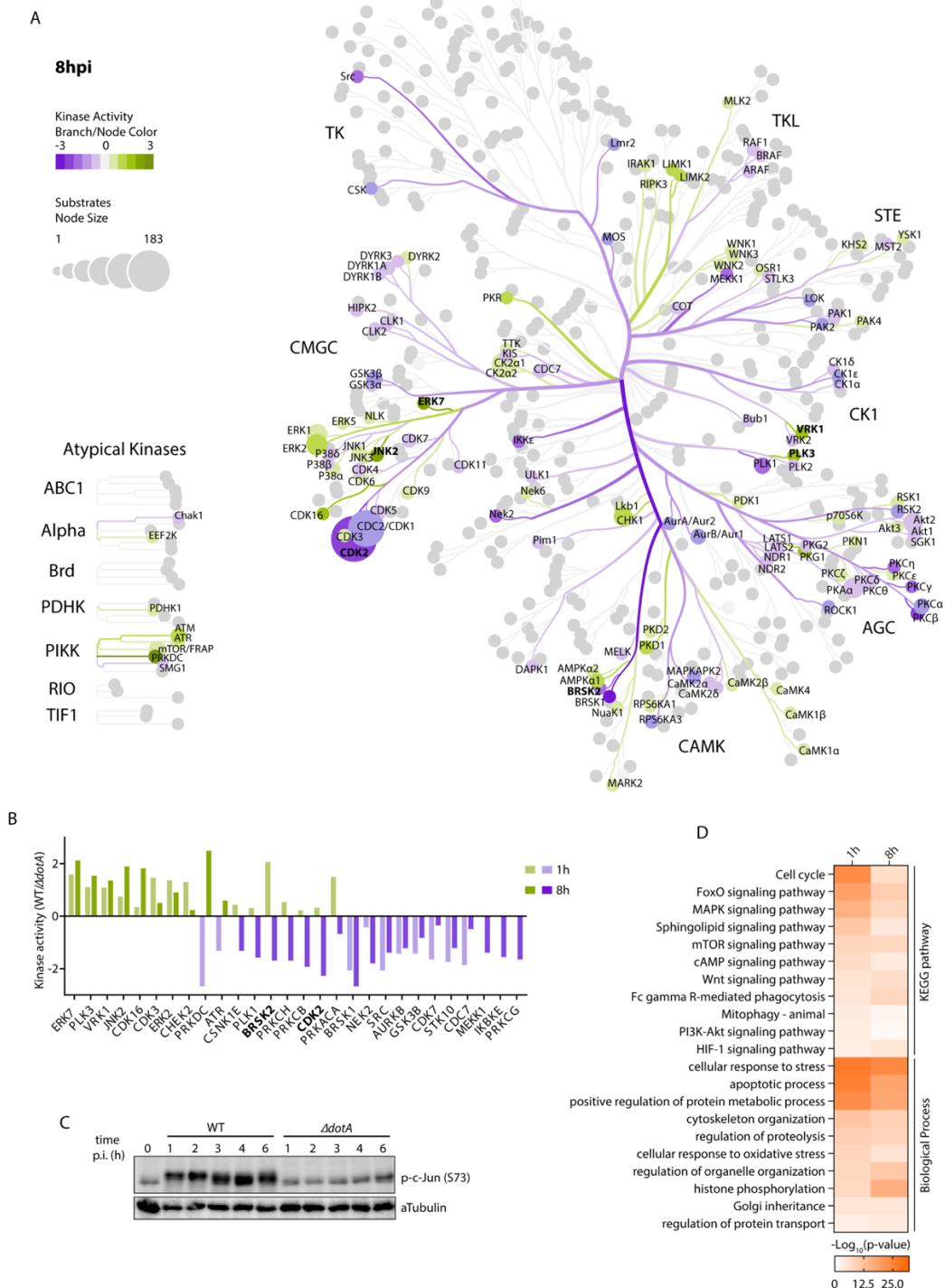
Figure 2.2: Dynamic regulation of kinase activities during *L.p.* infection. (A) Host cell kinase activities in WT- *vs*. *ΔdotA*-infected cells at 8hpi were inferred with PhosFate Profiler(Ochoa et al., 2016) based on regulated phosphorylated sites, and mapped on the kinase tree with CORAL (Metz et al., 2018). Kinase activity is indicated by the branch and node color, and the number of substrates by the node size. Names of kinase families are indicated around the tree. Kinases discussed in the text are highlighted in bold. **(B)** Inferred kinase activities of the most significantly regulated kinases (p-value ≤ 0.01) in WT- *vs*. *ΔdotA*-infected cells at 1hpi and 8hpi. Kinases discussed in the text are highlighted in bold. *Figure caption continued on the next page.*

Figure caption continued from the previous page. **(C)** Immunoblot analysis of phosphorylated c-Jun at serine 73 (p-c-Jun (S73)) and αTubulin (loading control) levels in HEK293 FcγR cells during infection with the *L.p.* WT- or Δ*dot*A strain (MOI 100). **(D)** Gene ontology enrichment analysis of kinases with predicted upregulated activities in WT- *vs.* Δ*dotA*-infected cells. Shown are the most significantly overrepresented pathways (KEGG pathways) and biological processes.

The analysis of the phosphoproteome with PhosFate Profiler also allows the prediction of the activities of protein complexes regulated by phosphorylation (Ochoa et al., 2016). As with the inferred kinase activities, some protein complexes showed a comparable predicted regulation early and late during infection, including the stress-induced, transcriptional Erα-c-Jun complex **(Supplementary Figure 2.2B** and **Supplementary File 5**). However, most protein complexes were regulated in an opposite manner at 1hpi and 8hpi. For instance, the RNF20-RNF40-UbE2E1 complex which mediates histone monoubiquitination (Zhu et al., 2005), shows a predicted decreased activity in WT-infected cells at 1hpi, but increased activity at 8hpi (**Supplementary Figure 2.2B**). In contrast, the BMI1-HPH1-HPH2 complex involved in repression of gene expression (Alkema et al., 1997) was predicted to be highly active at 1hpi, but down-modulated at 8hpi (**Supplementary Figure 2.2B**). These results give new insights into the dynamics of host cell kinase signaling and complex regulation in response to *L.p.* infection and highlight new biological pathways and processes that might be exploited by *L.p.* effectors.

2.3.3 *Spatiotemporal changes in host cell protein abundance, ubiquitination, and phosphorylation in response to L.p. infection*

To gain a spatiotemporal overview of the T4SS-dependent proteomics changes during *L.p.* infection, we mapped the numbers of significantly regulated proteins (AB, UB, and PH changes combined, $|Log_2FC| \geq 1$, adj.-p-value ≤ 0.05) on their predicted major subcellular localization according to their primary evidence code (ECO), or, if not available, to their documented subcellular localization in The Human Protein Atlas database (Thul et al., 2017). The predicted subcellular localizations with the highest levels of protein regulation were the nucleus, the cytosol,

and the plasma membrane both early and late during *L.p.* infection (100-500 regulated proteins, **Figs 2.3A-B).** When comparing the early and late infection time point, almost all subcellular compartments experienced increases in protein regulation, with the most dramatic regulatory increases induced in the nucleus (+307 proteins), the cytoplasm (+142 proteins), the nucleolus (+48 proteins) and in the mitochondria (+35 proteins) (**Figs 2.3A-B**).
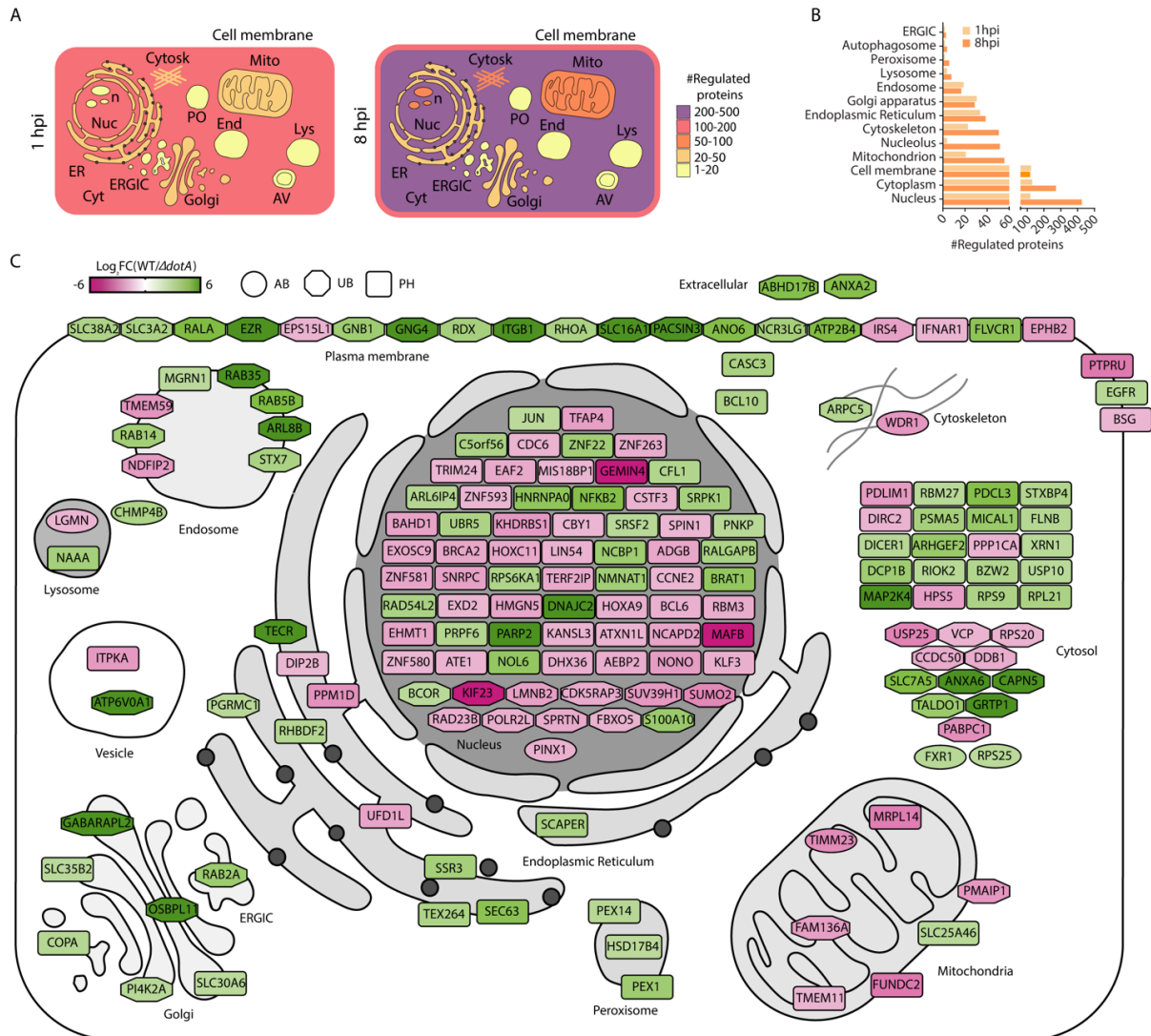
Figure 2.3: Spatiotemporal changes of the host cell proteome, ubiquitinome and phosphoproteome in response to *L.p.* WT infection. (A) The numbers of significantly regulated proteins (adj.-p-value ≤ 0.05, |Log2FC| ≥ 1) in WT vs. ΔdotA infected cells (AB, UB and PH combined) were quantified for and mapped on each predicted subcellular compartment. The number range of regulated proteins is indicated by the color code. Cytosk: cytoskeleton, Mito: mitochondria, PO: peroxisomes, n: nucleolus, Nuc: nucleus, ER: endoplasmic reticulum, ERGIC: ER-Golgi intermediate compartment, Cyt: cytosol, AV: autophagosome, End: endosome, Lys: lysosome. *Figure caption continued on the next page.*

28

Figure caption continued from the previous page. (B) Bar graph showing quantifications of panel (A). (C) Snapshot of WT-infected calls at 8hpi. Highly significantly regulated proteins (adj.-p-value ≤ 0.01, |Log$_2$FC(WT/ΔdotA)| ≥ 2) were mapped on the predicted host cell organelles according to their primary ECO with Cytoscape (Shannon et al., 2003). The Log$_2$FC values are indicated by a color scale (green: up-regulated, purple: down-regulated), the dataset is indicated by the shape of the icon (circle: AB, octagon: UB, rounded square: PH).

To obtain a more detailed picture of how host cell organelles are rewired at each infection timepoint, we mapped the top regulated proteins at 1hpi (adj.-p-value ≤ 0.01, |Log$_2$FC(WT/*ΔdotA)*| ≥ 1, 138 proteins total) and 8hpi (adj.-p-value ≤ 0.01, |Log$_2$FC(WT/*ΔdotA)*| ≥ 2, 196 proteins total) onto a visual depiction of the host cell (**Fig 2.3C** and **Supplementary Figure 2.3**). During early infection, the secretion of bacterial effectors prevents fusion of the phagosome enclosing *L.p.* with the endo-lysosomal compartment and leads to the recruitment of ER-derived vesicles that are required for the establishment of the LCV (Cornejo et al., 2017; Qiu and Luo, 2017b). In agreement with *L.p.*'s progression through the host cell, the top hits at 1hpi were mainly located in the cell membrane, the endosome, the ER and the Golgi apparatus (**Supplementary Figure 2.3**). Most of these top-regulated proteins at 1hpi (125/138) showed increased ubiquitination or phosphorylation in response to *L.p.* WT infection. These include proteins that are known to be ubiquitinated during infection, such as the GTPases RAB1A, RAB35, as well as proteins known to be phosphorylated, such as components of the ARP2/3 complex (Michard and Doublet, 2015; Mukherjee et al., 2011; Qiu et al., 2016). Other proteins, such as the vesicle-trafficking protein SEC22B, have been shown to be required for LCV formation (Arasaki and Roy, 2010; Kagan et al., 2004), but a modification of these proteins in response to infection has not been documented. In addition, the ER-shaping/ER-phagy proteins RTN1, RTN4, ATL3 and FAM134C were among the top regulated proteins and showed increased phosphorylation upon *L.p.* infection. These proteins were recently identified as phosphoribosyl-ubiquitinated targets of the non-canonical *L.p.* ubiquitin ligase SdeA (Kotewicz et al., 2017; Shin et al., 2020), suggesting a possible crosstalk with protein phosphorylation. Interestingly, we found modified proteins that have not been linked

to *L.p.* infection but might play a role for bacterial replication and/or be targets of *L.p.* effectors. For instance, proteins involved in mitochondrial membrane organization and ER-mitochondria tethering were regulated by phosphorylation (MFF, SLC25A46, VAPB, MMGT1) and deubiquitination (PMAIP1, MCL1) at 1hpi. Although the roles of these modifications are not known, they may reflect *L.p.*'s known regulation of host cell metabolism and mitochondrial morphology during infection.

In contrast to early infection, the top regulated hits at 8hpi – a timepoint when the LCV is established and resembles the rough ER – included fewer plasma membrane proteins and showed a broader distribution throughout the cell (**Fig 2.3C**). Most of these proteins were predicted to be in the nucleus (67/196). In accordance with the important role of the ER for *L.p.* replication, several ER proteins were among the highly regulated proteins. Interestingly, the recently discovered ER-phagy receptor TEX264, which is also an SdeA-mediated phosphoribosyl-ubiquitin target (An et al., 2019; Chino et al., 2019; Shin et al., 2020), was modified by phosphorylation in WT-infected cells, further highlighting a potential role of ER-phagy during *L.p.* infection. In addition, we observed increased phosphorylation of the ER translocon component SEC63 coinciding with recruitment of the rough ER to the LCV. Since SEC63 phosphorylation enhances translocon formation (Ampofo et al., 2013), this phosphorylation suggests that translocon formation and co-translational protein import may play key roles during *L.p.* infection. Analogous to the early infection timepoint, several mitochondrial proteins were among the top hits at 8hpi (TIMM23, FAM136A, MRPL14, TMEM11, PMAIP1, FUNDC2, SLC25A46), indicative of broadening regulation of mitochondria at later timepoints during infection. Taken together, the spatiotemporal analysis of host cell proteome changes during *L.p.* infection provides novel insights into the dynamic targeting of host cell organelles by *L.p.*.

2.3.4 L.p. induces hallmarks of a proteostatic mitochondrial stress response

We were particularly intrigued by the rewiring of mitochondrial during infection. Mitochondria are vital organelles with diverse functions, including energy generation and metabolism, calcium signaling, lipid and amino acid metabolism, innate immune signaling, bacterial clearance through reactive oxygen species (ROS) generation, and apoptotic signaling. It is therefore not surprising that many intracellular pathogens target mitochondria to benefit or protect themselves from these functions (Ramond et al., 2019; Tiku et al., 2020). Although the recruitment of mitochondria to the LCV was first described almost four decades ago (Horwitz, 1983), the functional consequences of this interaction and the role of mitochondria during *L.p.* infection remain largely elusive. A recent report suggests that the *L.p.* effector MitF modulates mitochondrial dynamics to shift mitochondrial metabolism towards a Warburg-like metabolism in macrophages, thereby promoting bacterial replication (Escoll et al., 2017). Other groups have reported that certain *L.p.* effectors can translocate into host cell mitochondria to modulate lipid metabolism and metabolite transport (Degtyar et al., 2009; Dolezal et al., 2012). Finally, it is known that WT *L.p.* suppresses mitochondrial ROS (Harada et al., 2007), inhibits cell death signaling (Arasaki et al., 2017; Banga et al., 2007; Laguna et al., 2006), and replicates more efficiently in mitochondrially diseased amoeba (Francione et al., 2009). Despite these advances, much is unknown about the roles mitochondria play during infection. We thus decided to better characterize changes in the mitochondrial proteome by analyzing the regulation of proteins with annotated mitochondrial localization, as determined by the MitoCarta3.0 database (Rath et al., 2020), in more detail.

When we compared the mitochondrial proteome in WT- and *ΔdotA*-infected cells, we found significant ($|Log_2FC(WT/\Delta dotA)| \geq 0.5$, adj.-p-value ≤ 0.05) abundance, ubiquitination, and phosphorylation changes at both 1hpi and 8hpi, with almost 4.5 times more regulatory events occurring 8hpi (**Fig 2.4A**). Intriguingly, we noticed that the 8hpi response to infection included numerous mitochondrial proteins with significant abundance decreases, potentially indicative of

mitochondrial dysfunction. To better characterize which mitochondrial pathways may be regulated at later timepoints during infection, we performed functional enrichment and network analyses on mitochondrial proteins experiencing significant abundance changes at 8hpi. Regulated proteins clustered strongly into 7 clearly defined functional enrichment groups composed almost exclusively of protein downregulations, the largest four containing mitochondrial translation machinery (e.g. MRPS7, MRPL14), protein import subunits (e.g. TIMM17A, TIMM23), oxidative phosphorylation (OXPHOS) subunits (e.g. COX6B1, NDUFA4), and mitochondrial RNA synthesis/processing proteins (e.g. PTCD1, ELAC2) (**Fig 2.4B**). In addition, we noticed downregulation of the mitochondrial inner membrane GTPase OPA1, which plays key roles in cristae maintenance and inner membrane fusion (Dotto et al., 2018). Upon several types of mitochondrial stress, long isoforms of OPA1 (L-OPA-1) are proteolytically processed into shorter isoforms (S-OPA-1), inhibiting mitochondrial fusion and promoting fission. Strikingly, the downregulation of OPA1, as well as mitochondrial translation and OXPHOS machinery, is the proteomic hallmark of a "core" mitochondrial stress response (MSR), induced in response to numerous forms of mitochondrial stress (Quirós et al., 2017). Although the downregulation of protein import machinery is not part of this "core" MSR, it is a known response to certain types of mitochondrial stress, particularly proteotoxic stress that triggers the mitochondrial unfolded protein response (UPR[mt]) (Arnould et al., 2015; Rainbolt et al., 2013).
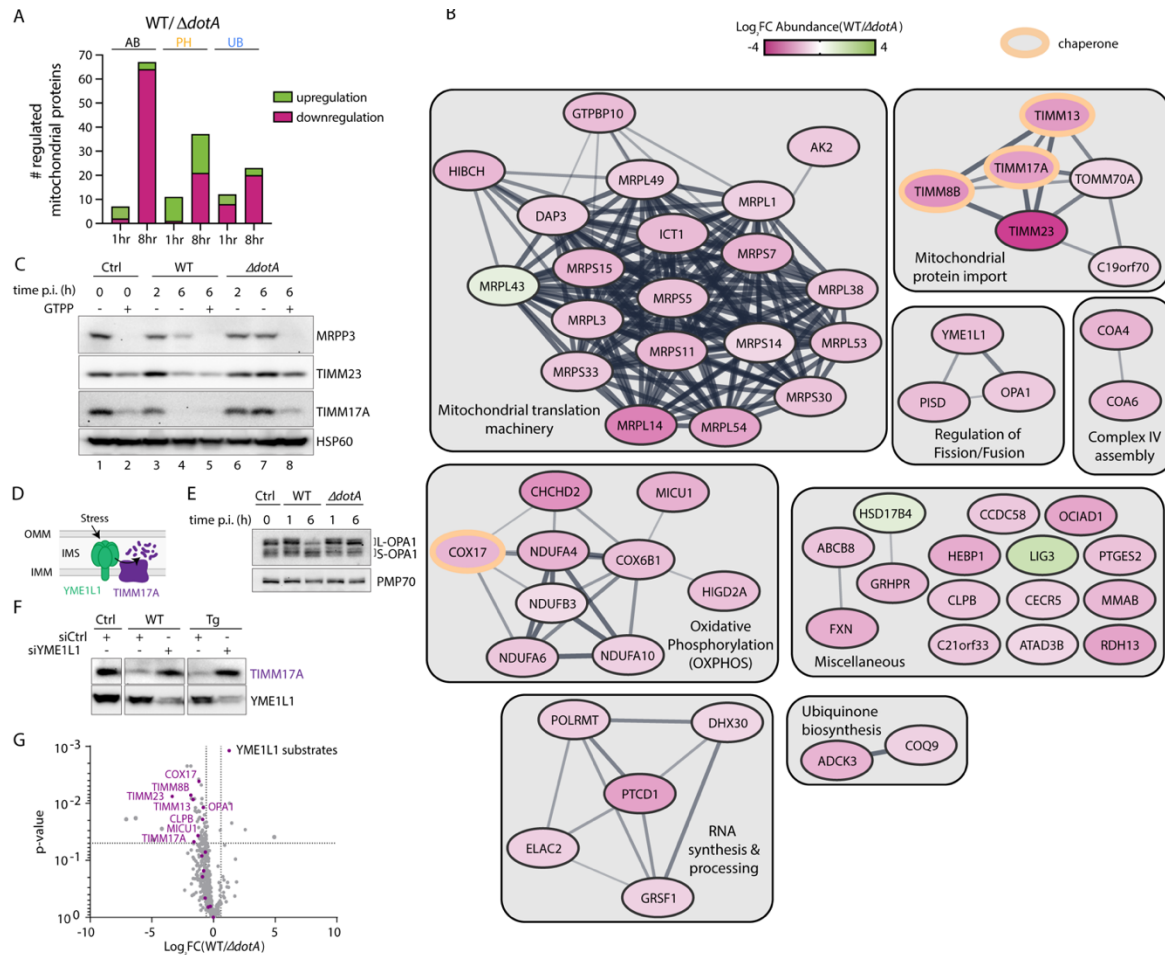
Figure 2.4: *L.p*. reshapes the mitochondrial proteome. (A) Number of mitochondrial proteins/proteoforms whose abundance (AB), ubiquitination (UB) or phosphorylation (PH) was regulated in WT- *vs. ΔdotA*-infected cells, (adj.-p-value ≤ 0.05, |Log$_2$FC| ≥ 0.5) at 1hpi and 8hpi. **(B)** Gene ontology enrichment and network analysis of mitochondrial proteins with significant abundance changes in WT- *vs. ΔdotA*-infected cells at 8hpi was performed with the Cytoscape stringApp.(Doncheva et al., 2019; Shannon et al., 2003) Clustering was performed using an MCL algorithm with an inflation value of 4. Colors represent protein upregulation (green) or downregulation (purple). Edges represent predicted functional associations. Clusters with overrepresented pathways or annotations from enrichment analyses are annotated. **(C)** Uninfected (Ctrl), WT- or *ΔdotA*-infected (MOI 25) HEK293 FcγR cells were treated with DMSO (-) for 2h or 6h, or GTPP (+, 10 μM) for 6h. Protein levels of the UPR^{mt} markers MRPP3, TIMM23, and TIMM17A (loading control: HSP60) were analyzed by immunoblot. **(D)** During different stress conditions, the i-AAA protease YME1L1 located in the IMM is activated and cleaves TIMM7A to decrease mitochondrial protein import, and processes OPA1. **(E)** HEK293 FcγR cells were left uninfected (Ctrl) or infected with *L.p.* WT or *L.p. ΔdotA* for 1h and 6h (MOI 25). Protein levels of OPA1 isoforms and PMP70 (loading control) were analyzed by immunoblot. L-OPA1: long OPA-1, S-OPA1: short OPA-1. n=2 biological replicates. **(F)** HEK293 FcγR cells were transfected with control siRNA or siRNA targeting YME1L1 and either left untreated, infected with WT *L.p.* (MOI 25) or treated with 10 μM thapsigargin (Tg, positive control) for 6h. TIMM17A and YME1L1 protein levels were analyzed by immunoblot. **(G)** Volcano plot showing all detected mitochondrial proteins WT- vs. ΔdotA-infected cells. Known stress-induced YME1L1 substrates(MacVicar et al., 2019) are highlighted in purple.

33

To confirm our proteomics and potential UPR[mt] induction, we compared the protein levels of several UPR[mt] related proteins in uninfected, WT- or *ΔdotA*-infected cells in absence or presence of gamitrinib-triphenylphosphonium (GTPP), a specific inhibitor of the mitochondrial chaperone HSP90/TRAP1 and inducer of the UPR[mt] (Kang et al., 2009; Münch and Harper, 2016; Siegelin et al., 2011). As previously reported, induction of the UPR[mt] with GTPP led to degradation of the mitochondrial ribonuclease P catalytic subunit (MRPP3, **Fig 2.4C**, lane 2 *vs.*1) (Münch and Harper, 2016). Similarly, infection with the *L.p.* WT strain, but not the *ΔdotA* strain, led to a robust reduction in MRPP3 levels at 6hpi (**Fig 2.4C**, lane 4 *vs.*1), which was further reduced upon additional treatment with GTPP (**Fig 2.4C**, lane 5 *vs.*1). Likewise, TIMM17A and TIMM23 protein levels were reduced in both GTPP-treated and WT-infected, but not in *ΔdotA*-infected cells. These results confirm the abundance decreases of TIMM17A and TIMM23 detected in our proteomics and provide further evidence of mitochondrial proteostatic stress during infection.

A key aspect of MSRs like the UPR[mt] is remodeling of the mitochondrial proteome by mitochondrial proteases (Ahola et al., 2019; Lebeau et al., 2018). Since numerous *L.p.* effectors are potent inhibitors of host cell translation, we investigated whether the downregulation of mitochondrial proteins was due to mitochondrial protease activation or global translation inhibition (Belyi et al., 2008, 2006; Cornejo et al., 2017; Moss et al., 2019; Shen et al., 2009). Specifically, we evaluated processing of L-OPA-1 and degradation of TIMM17A, known substrates of the stress-sensitive mitochondrial i-AAA protease YME1L1 (**Fig 2.4D**) (MacVicar et al., 2019; Rainbolt et al., 2013). Consistent with YME1L1 activation and mitochondrial fragmentation during infection, L-OPA-1 was cleaved into shorter isoforms (S-OPA-1) in T4SS-dependent manner (**Fig 2.4E**). In addition, siRNA-mediated knockdown of YME1L1 abrogated the degradation of TIMM17A during infection as well as during treatment with thapsigargin (Tg), a known inducer of YME1L1 (Rainbolt et al., 2013), suggesting that the downregulation of TIMM17A during *L.p.* WT infection requires active YME1L1 and that translation inhibition plays little or no role (**Fig 2.4F**). Indeed, the

abundance of several other recently discovered, stress-induced YME1L1 substrates (MacVicar et al., 2019) was down-regulated in *L.p.* WT infected cells (**Fig 2.4G**), providing further evidence of YME1L1 activation during infection. Altogether, these results demonstrate the presence of an active UPR^mt-like MSR during infection as indicated by the activation of YME1L1.

Our proteomics at 8hpi detected numerous mitochondrial proteins experiencing significant phosphorylation and ubiquitination changes (**Fig 2.4A**). To determine how the mitochondrial proteome is regulated by PTMs at 8hpi, we performed a functional enrichment and network analysis on these proteins (**Supplementary Figure 2.4A-B**). Interestingly, mitochondrial protein import, translation, and OXPHOS machineries were enriched in these networks as well, suggesting novel PTM-mediated mechanisms for regulation of these proteins during mitochondrial stress responses. PTM-mediated regulation was also enriched on proteins involved in the regulation of apoptosis and mitochondrial fission/fusion, consistent with known modulation of cell death processes and morphology during infection (**Supplementary Figure 2.4A-B**) (Arasaki et al., 2017; Banga et al., 2007; Degtyar et al., 2009; Dolezal et al., 2012; Laguna et al., 2006; Tiku et al., 2020).

In conclusion, combinatorial analysis of our datasets exposes a drastic remodeling of the mitochondrial proteome during infection in a T4SS-dependent manner. Notably, we show for the first time that WT *L.p.* infection leads to activation of a mitochondrial proteostatic stress response such as the UPR^mt. Our results build on past work demonstrating mitochondrial fragmentation and attenuated respiration during infection (Escoll et al., 2017), as these responses are frequently driven by stress.

2.3.5 *L.p. infection modulates the translational response to mitochondrial stress*

We next decided to explore the transcriptional response to mitochondrial stress during infection. Mitochondrial stress is one of numerous cellular stressors that induces a nuclear response through the integrated stress response (ISR), although many details of this mito-nuclear communication are not yet understood, and ISR-independent routes may exist (Anderson and Haynes, 2020; Callegari and Dennerlein, 2018; Lebeau et al., 2018; Mottis et al., 2019). Generally, it is thought that mitochondrial stress induces activation of one or multiple ISR kinase(s) (PERK, PKR, GCN or HRI), resulting in the phosphorylation of eIF2α at serine 51. This phosphorylation event leads to global translational attenuation while allowing the preferential translation of the transcription factors ATF3, ATF4, ATF5, and CHOP, as well as their downstream targets, which include themselves, the eIF2α phosphatase GADD34, and stress mitigating genes (cartoon in **Fig 2.5A**) (Pakos-Zebrucka et al., 2016). To evaluate mito-nuclear stress signaling during infection, we measured *ATF3*, *ATF4*, *ATF5*, *CHOP*, and *GADD34* transcript levels during infection by qPCR. In accordance with mito-nuclear stress signaling, transcripts for all of these genes were elevated in response to *L.p.* WT, but not *ΔdotA* infection (**Fig 2.5B**). *ATF4* and *CHOP* induction was noticeable from low to high multiplicities of infection (MOI), suggesting that mito-nuclear stress signaling was not an artifact of high MOI (**Supplementary Figure 2.5A**).
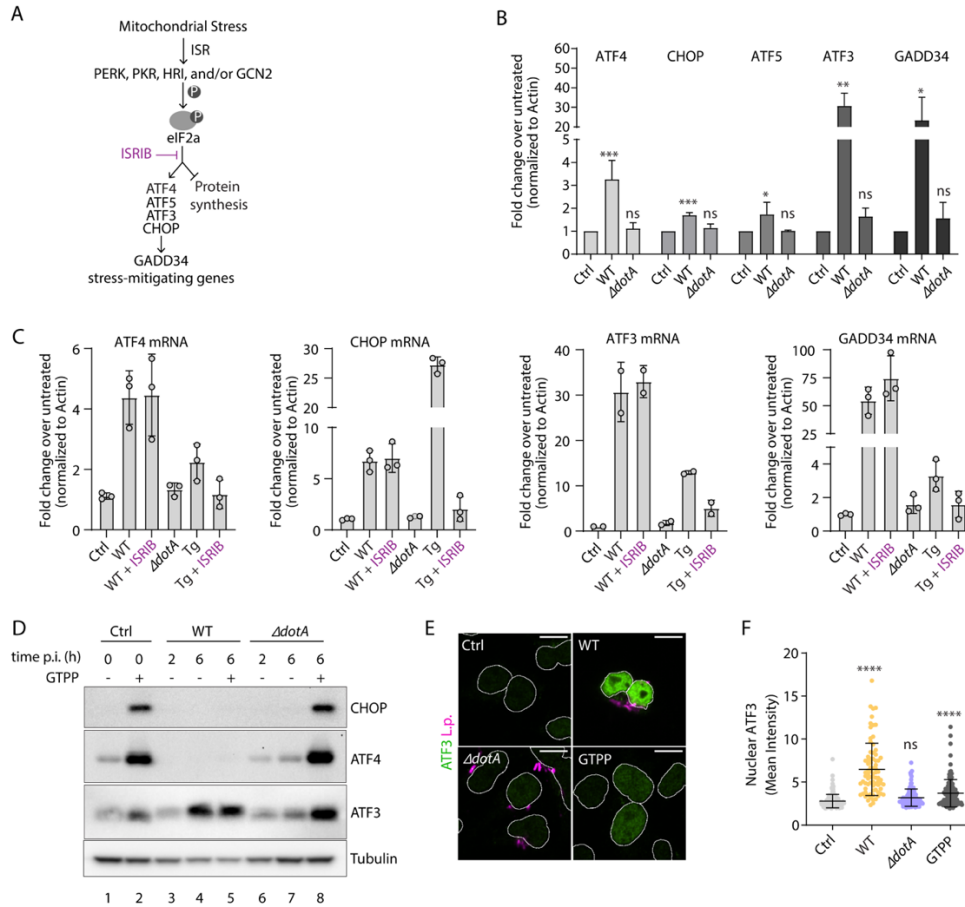
Figure 2.5: ***L.p.* infection modulates the mitochondrial stress response. (A)** Cartoon depicting signaling through the ISR during mitochondrial stress. **(B)** qPCR of *ATF4*, *CHOP*, ATF5, *ATF3* and *GADD34* in uninfected, WT- or *ΔdotA*-infected HEK293 FcγR (6hpi, MOI 10). Transcript levels were normalized to *Actin*. Shown are the mean levels relative to the control ± SEM of n = 2 biological replicates. Statistical differences were analyzed by one-way ANOVA and Tukey's multiple comparison test. *** p ≤ 0.001, ** p ≤ 0.01, * p ≤ 0.05, ns > 0.05. **(C)** HEK293 FcγR cells were infected with *L.p.* WT or ΔdotA (6h infection, MOI 100) in presence or absence of the inhibitor ISRIB (200 nM) for 6h. Thapsigargin (Tg, 10 µM, 6hr treatment) was used as a positive control. qPCR of ATF4, CHOP, ATF3 and GADD34 mRNA levels were analyzed by qPCR. Shown are the mean levels relative to the control ± SD of n = 3 or n = 2 (ATF3) biological replicates. **(D)** Uninfected (Ctrl), WT- or *ΔdotA*-infected (MOI 25) HEK293 FcγR cells were treated with DMSO (-) for 2h or 6h, or GTPP (+, 10 µM) for 6h. Protein levels of the transcription factors ATF3, ATF4, and CHOP (loading control: tubulin) were analyzed by immunoblot. **(E)** The levels of nuclear ATF3 in untreated (Ctrl), GTPP-treated (10 µM, 6h), *L.p.* WT- or Δdot-infected HEK293 FcγR cells (MOI 5, 6h) were analyzed by immunofluorescence microscopy. Cells were stained with Hoechst33342 to define the nuclear area (shown as outline), anti-ATF3 antibody (green) and anti-*L.p.* antibody (magenta). Scale bar: 10 µm. **(F)** The background corrected, nuclear ATF3 signal (mean intensity) was quantified by automated image analysis with CellProfiler (Carpenter et al., 2006). Each dot represents one cell. Shown is the mean ± SD of n ≥ 78 cells. Statistical differences were analyzed by one-way ANOVA and Tukey's multiple comparison test. p-value **** p ≤ 0.0001, p-value ** p ≤ 0.01, ns p > 0.05.

Since *L.p.* is a known manipulator of host cell stress responses, we decided to test whether ISR inhibition could abrogate stress gene induction during *L.p.* infection. In order to do this, we treated infected cells with or without the ISR inhibitor ISRIB (Sidrauski et al., 2013) (**Fig 2.5A**) and analyzed the mRNA levels of *ATF3*, *ATF4*, *CHOP* and *GADD34*. Much to our surprise, ISRIB did not abrogate robust induction of these transcripts upon *L.p.* infection **(Fig 2.5C)**. In contrast, ISRIB abolished the induction of the same genes upon treatment with Tg, a known activator of the ISR. Since ISRIB cannot block high or prolonged levels of ISR activation (Rabouw et al., 2019), these results suggest either that the ISR is not required for the transcriptional induction of *ATF3*, *ATF4, CHOP* and *GADD34*, or that ISR activation overpowers the inhibitory effects of ISRIB during infection. Indeed, our proteomic data and confirmatory western blotting do not detect appreciable phosphorylation of eIF2α during infection (**Supplementary File 2** and **Supplementary Figure 2.5B**), indicative of ISR-independent pathways leading to transcription factor induction.

Since *L.p.* is known to suppress CHOP translation during infection, we decided to determine whether *L.p.* induction of the transcription of the aforementioned genes leads to their translation in uninfected, WT- or *ΔdotA*-infected cells in absence or presence of GTPP. Consistent with UPR^{mt} and ISR activation, GTPP led to a strong increase in ATF4, CHOP protein levels in uninfected and *ΔdotA*-infected cells (**Fig 2.5D**, lane 2 *vs.* 1 and lane 8 *vs.* 6). ATF3, which is transcribed during the core MSR (Quirós et al., 2017) but does not yet have a characterized role, was also robustly translated in GTPP-treated uninfected and *ΔdotA*-infected cells, suggesting that it may play some role in the UPR^{mt}. Strikingly, the induction of CHOP and ATF4 at the protein level was completely suppressed in WT-infected cells treated with or without GTPP (**Fig 2.5D**, lane 5 *vs.* 2). In contrast, ATF3 was strongly induced in WT-infected cells regardless of GTPP treatment. Since ATF4 and CHOP translation is required for the upregulation several mitochondrial stress-mitigating genes including the mitochondrial chaperonins Hsp10 and Hsp60 (Horibe and Hoogenraad, 2007; Quirós et al., 2017; Zhao et al., 2002), this translational

suppression suggests that *L.p.* infection induces a mitochondrial stress response but modulates downstream mitigation of that stress mediated through the ISR.

Given that *L.p.* strongly inhibits global protein translation via multiple effectors (Belyi et al., 2008, 2006; Cornejo et al., 2017; Moss et al., 2019; Shen et al., 2009), we were intrigued by the selective translation of ATF3 during infection. ATF3 is a bZIP domain transcription factor implicated in numerous multiple cellular stress responses that can either activate or repress transcription of its target genes (Jadhav and Zhang, 2017). ATF3 is known to be transcribed during some types of mitochondrial stress (Quirós et al., 2017), and has been shown to repress the transcription of PINK1, an important player in mitophagy, highlighting its potential role for mitochondrial homeostasis (Bueno et al., 2018). Given the extensive manipulation of stress responses during infection, we decided to verify that translated ATF3 translocates to the nucleus. As expected, nuclear ATF3 was significantly enhanced in cells treated with gamitrinib-triphenylphosphonium (GTPP) (**Figs 2.5E-5F**) (Kang et al., 2009; Münch and Harper, 2016; Siegelin et al., 2011). Nuclear ATF3 induction was even higher in cells infected with the *L.p.* WT strain, but not significantly induced in *ΔdotA*-infected cells. These results suggest that ATF3-mediated transcription programs are likely active during infection.

In short, *L.p.* induces an effector-driven mitochondrial stress response that induces changes in the abundance, ubiquitination, and phosphorylation of several proteins involved in mitochondrial proteostasis. This stress response shares similarities with the UPR^{mt} and results in the activation of the mitochondrial protease YME1L1, thereby downregulating the mitochondrial protein import, gene expression, OXPHOS, and fusion machinery. Intriguingly downstream nuclear targets ATF3, ATF4, ATF5, CHOP, and GADD34 are transcribed in the presence of the ISR-inhibitor ISRIB. Despite the transcription of these genes, *L.p.* infection suppresses the translation of ATF4 and CHOP, two central transcription factors of ISR-dependent stress responses, but allows for

the translation and activation of ATF3. This selective translation of ATF3 undoubtedly modulates adaptive responses to mitochondrial stress during infection, although further work is needed to determine its mechanism.

2.4   Discussion

In this study, we used a global proteomics approach to identify novel host cell signaling pathways, organelles and proteins that are regulated during *L.p.* infection through the secretion of bacterial effectors. To our knowledge, this is the most comprehensive resource of the regulation and/or modification of host cell proteins upon *L.p.* infection to date. Our analysis includes the quantification of changes in host cell protein abundance, ubiquitination, and phosphorylation. We confirmed proteomic changes known to occur during infection, but also revealed novel exciting leads. For example, we found that peroxisomal proteins are regulated during *L.p.* infection (**Figs 2.3 and Supplementary Figure 2.3**), suggesting a previously unexplored role of peroxisomes during this process. Our analysis also highlighted the nucleolus as a potential major target of *L.p.* effectors (**Figs 2.3A-B**), an organelle that has recently been implicated in the resistance to bacterial pathogens (Tiku et al., 2018). Interestingly, the *L.p.* effector RomA/LegAS4 has been proposed to modulate nucleolar function through the modification of chromatin in regions encoding ribosomal RNA genes (Li et al., 2013; Rolando et al., 2013), further suggesting that the nucleolus is rewired during *L.p.* infection through the actions of one or more bacterial effectors and/or as part of the host cell response. Our study serves as a platform to gain more insights into the regulation of organelles targeted by *L.p.* effectors.

Our data reveal that the mitochondrial proteostasis network is perturbed and regulated during *L.p.* infection in a T4SS-dependent manner. Due to the downregulation of mitochondrial protein import machinery (**Fig 2.4**), this response shares similarities with the UPR^{mt}, a homeostatic stress

signaling response induced upon accumulation of misfolded proteins in the mitochondrial matrix (Shpilka and Haynes, 2017). We have several non-mutually exclusive hypotheses regarding why *L.p.* infection may induce an MSR. First, it has been shown that the UPR^{mt} is induced as an adaptive response in cells experiencing the Warburg effect (Kenny et al., 2019), suggesting that the previously reported infection-induced shift in mitochondrial metabolism (Escoll et al., 2017) might be upstream of a UPR^{mt}-like stress response in infected cells. Second, *L.p.*'s need for amino acids, lipids, and other metabolites to survive and replicate intracellularly (Best and Kwaik, 2018; Kowalczyk et al., 2021; Price et al., 2011) may overtax host cell mitochondria, resulting in stress. Third, effector-mediated inhibition of host cell protein synthesis during *L.p.* infection might contribute to the induction of a mitochondrial stress response (Andréasson et al., 2019). Finally, given that translation of ATF4 and CHOP is blocked, key transcription programs leading to mitochondrial homeostasis are also likely blocked (Horibe and Hoogenraad, 2007; Quirós et al., 2017; Zhao et al., 2002). This suggests that the translocation of bacterial effectors into host cell mitochondria may have evolved to intentionally induce mitochondrial stress and disease, potentially allowing *L.p.* to avoid bactericidal ROS production and to preferentially rewire the metabolism of the host cell. Determining how and why an MSR is induced during infection is an promising area of future research that may provide insights into both pathogenic and host cell mechanisms.

 Much to our surprise, we found the downstream transcriptional response to mitochondrial stress to be highly modulated during infection. In line with a mitochondrial stress response, infection induced the transcription of classic ISR-activated target genes including *ATF3*, *ATF4*, *ATF5*, *CHOP*, and *GADD34* (Guo et al., 2020; Quirós et al., 2017; Samluk et al., 2019). Unexpectedly, we found their induction to occur even in the presence of the ISR inhibitor ISRIB. Since ISRIB is not able to overcome prolonged or high levels of ISR activation, this result may suggest that ISRIB is an insufficient inhibitor of ISR activation during infection (Rabouw et al., 2019). Alternatively,

our data showing no appreciable increase in eIF2α phosphorylation during infection (**Supplementary Figure 2.5B**) lead us to favor an alternate hypothesis: that expression of these genes may be triggered by yet undefined ISR-independent signaling routes. Among the large arsenal of secreted effectors, it is possible that *L.p.* secretes one or several effectors to directly induce transcription of these genes, potentially by histone modification or by binding directly to promoter sequences. Several lines of evidence also support the presence of signaling routes that operate in tandem with the ISR during the UPR^mt to contribute to gene induction (Horibe and Hoogenraad, 2007). Notably, despite being one of numerous stressors that can activate the ISR, the UPR^mt is the only known stressor capable of inducing upregulation of mitochondrial chaperonins (Münch and Harper, 2016), suggestive of additional and unknown signaling factors. In addition, up-regulation of CHOP upon UPR^mt induction with GTPP or the LonP protease inhibitor CDDO does not seem to require any individual ISR kinase, suggesting the involvement of multiple ISR kinases or potentially an ISR-independent route to CHOP induction (Fessler et al., 2020; Münch and Harper, 2016). Indeed, past work has found that the induction of CHOP during the UPR^mt is entirely dependent on the presence of an AP-1 site (bound by c-Jun) in the CHOP promoter (Horibe and Hoogenraad, 2007). Pharmacological inhibition of MEK/JNK2 signaling, which subsequently prevents phosphorylation and activation of c-Jun, is also sufficient to block transcription of mitochondrial proteases during the UPR^mt (Horibe and Hoogenraad, 2007). Since c-Jun is also capable of inducing ATF3 transcription (Fu and Kilberg, 2013), it is possible that *L.p.*-induced mitochondrial stress induces JNK2 activation and c-Jun phosphorylation (**Figs 2.2B-C**), which then leads to CHOP and ATF3 transcription. More experimentation is required to determine if JNK2 signaling may also explain the transcription of ATF4, ATF5, and GADD34 during infection, and also how UPR^mt/JNK signaling synergizes with UPR^mt/ISR signaling in uninfected conditions. Additionally, we note here that numerous non-mitochondrial cellular stressors can lead to JNK signaling and/or ATF3 transcription (Ku and Cheng, 2020; Meng and

Xia, 2011), thus more work is needed to determine if ATF3 transcription during infection is solely downstream of mitochondrial stress.

In addition to our interest in transcriptional modulation during infection, we were particularly intrigued by the selective translation of ATF3 despite the suppression of ATF4 and CHOP translation upon *L.p.*-induced stress. Canonically, eIF2α phosphorylation during the ISR leads to global translation attenuation of most mRNAs and "privileged" translation of mRNAs such as *ATF3*, *ATF4*, *ATF5*, *CHOP*, and *GADD34* due to the presence of upstream open reading frames (uORFs) in their 5' untranslated regions (Anderson and Haynes, 2020; Pakos-Zebrucka et al., 2016). Based on current knowledge, the privileged translation of solely ATF3 mRNAs amongst this set of known uORF-containing mRNAs is unprecedented and indicates that *L.p.* induces a novel form of privileged translation during infection based on still-undiscovered regulatory elements in ATF3 mRNA. In addition, the functionality of ATF3 as a transcription factor is highly dependent on its dimerization with itself (transcriptionally repressive) or with other transcription factors like CHOP or c-Jun (transcriptionally activating) (Hai et al., 1999). Given the phosphorylation and activation of c-Jun during infection, it would be intriguing to determine whether ATF3/c-Jun transcription programs are active during infection, and if so, the role that these programs play during infection for the host cell or for *L.p.*'s pathogenesis.

2.5   Additional data and discussion

2.5.1   *Legionella does not induce a proteostatic MSR in U937 monocytes*

Mitochondria are central players in immune signaling and play key roles in the activation, differentiation, survival of immune cells (Tiku et al., 2020). Although HEK293 cells are capable of some forms of innate immune signaling, they are deficient in numerous immune sensors and responses, such as STING, TLRs, and cytokine secretion (Burdette et al., 2011; Ferreira et al.,

43

2020; Hornung et al., 2002). In order to assess the influence of immune signaling on the infection-induced MSR observed in HEK293 cells, we infected undifferentiated U937 cells and evaluated MSR induction via Western Blot. As seen in HEK293 cells, we noticed robust cleavage of long isoforms of OPA1 at 8hpi, as well as phosphorylation of c-Jun (**Figure 2.6**). Surprisingly, we did not observe degradation of the mitochondrial protein import channel TIMM23, or the mitochondrial ribonuclease subunit MRPP3. These results suggest that a proteostatic stress response like the UPRmt is not induced during infection of undifferentiated U937 cells. The cleavage of long OPA1 isoforms, however, suggests the presence of mitochondrial protease activation as well as unopposed mitochondrial fission (Zemirli et al., 2018). Past work has demonstrated that mitochondrial fragmentation occurs during *Legionella* infection of macrophages and is stimulated by the secreted effector MitF/LegG1 (Escoll et al., 2017). More work is required to determine if OPA1 cleavage is the product of a broader MSR potentially triggered by MitF activity, or if OPA1 cleavage and mitochondrial fission occurs in the absence of MSR signaling.
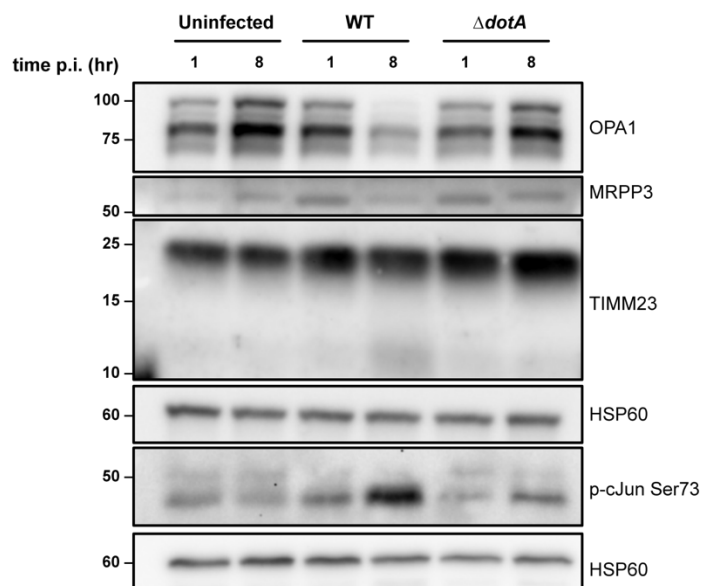
Figure 2.6: *Legionella* **does not induce a proteostatic MSR in U937 monocytes.** Undifferentiated U937 cells were infected with the indicated *Legionella* strains at an MOI of 50 and were analyzed by immunoblot.

2.5.2 Lpg2444-induced fusion is mitoprotective against the mitochondrial uncoupler CCCP

In our preprint manuscript published on bioRxiv, we show that the secreted *Legionella* effector Lpg2444 localizes to mitochondria, induces massive mitochondrial fusion, and antagonizes mitochondrial depolarization and fragmentation upon treatment with the decoupling agents CCCP or GTPP (Noack et al., 2020). As is true with many secreted *Legionella* effectors, the Lpg2444 sequence shows no homology with known proteins, and thus provides no clues regarding the mechanisms underlying the phenotypes observed during Lpg2444 overexpression.

In order to better assess how Lpg2444 expression confers resistance to depolarization, we decided to assess OPA1 cleavage and ATF4 upregulation in HEK293 cells transfected with GFP-Lpg2444 upon treatment with decoupling agents. As expected, GFP transfected control cells showed robust cleavage of L-OPA-1 and strong upregulation of ATF4 (**Figure 2.7**). This response is consistent with mitochondrial stress protease activation, which leads to cleavage of L-OPA-1 as well as the signaling protein DELE1, whose export from the mitochondria activates the ISR (Guo et al., 2020; Quirós et al., 2017). Surprisingly, GFP-Lpg2444 transfected cells showed robust cleavage of L-OPA-1 but attenuated upregulation of ATF4. This result suggests that Lpg2444 cannot block mitochondrial stress protease activity, but attenuates the signaling of stress signals from the mitochondria through some alternate mechanism.
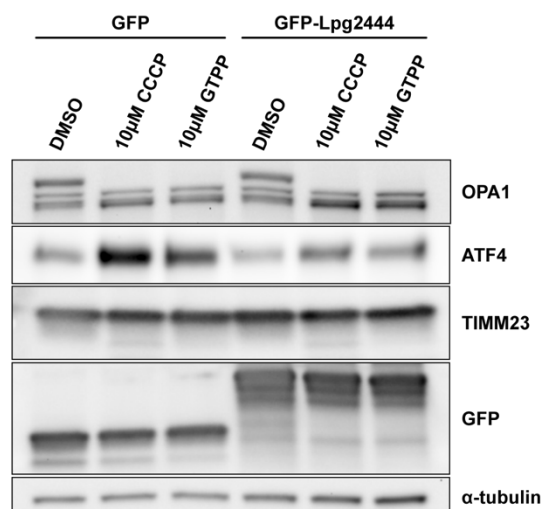
Figure 2.7: Expression of Lpg2444 attenuates ATF4 upregulation. HEK293 cells were transfected with either GFP or GFP-Lpg2444 and then treated with DMSO, 10μM CCCP, or 10μM GTPP for 6 hours. Cells were then lysed and analyzed via immunoblot.

Since mitochondrial fusion is associated with stress resistance, we decided to test if inducing mitochondrial hyperfusion by alternate mechanisms could phenocopy the attenuation of stress signaling observed during GFP-Lpg2444 overexpression. Indeed, past work has shown that overexpression of the mitochondrial fusion regulators mitofusin 1 (Mfn1) and mitofusin 2 (Mfn2) can result in extremely hyperfused mitochondria, similar to those seen during Lgp2444 overexpression (Eura, 2003; Noack et al., 2020). In order to test if Mfn1 and Mfn2 overexpression might phenocopy Lpg2444 overexpression, we transfected HeLa cells with GFP-Mfn1 (Addgene #141154) or mCherry-Mfn2 (Addgene #141156) and assessed mitochondrial morphology. As expected, both GFP-Mfn1 and mCh-Mfn2 expression resulted in mitochondrial hyperfusion (**Figure 2.8A**) similar to that seen during GFP-Lpg2444 expression. We next transfected HEK293 cells with GFP-Lpg2444, GFP-Mfn1, of mCh-Mfn2 and evaluated L-OPA-1 cleavage and ATF4 upregulation after treatment with CCCP. In line with mitochondrial fusion attenuating stress signaling from mitochondria, expression of GFP-Lpg2444, GFP-Mfn1, and mCh-Mfn2 decreased the expression of ATF4 in the presence of CCCP, despite cleavage of L-OPA-1 (**Figure 2.8B**).

This suggests that an underlying mechanism to Lpg2444-induced stress resistance is its ability to hyperfuse mitochondria.
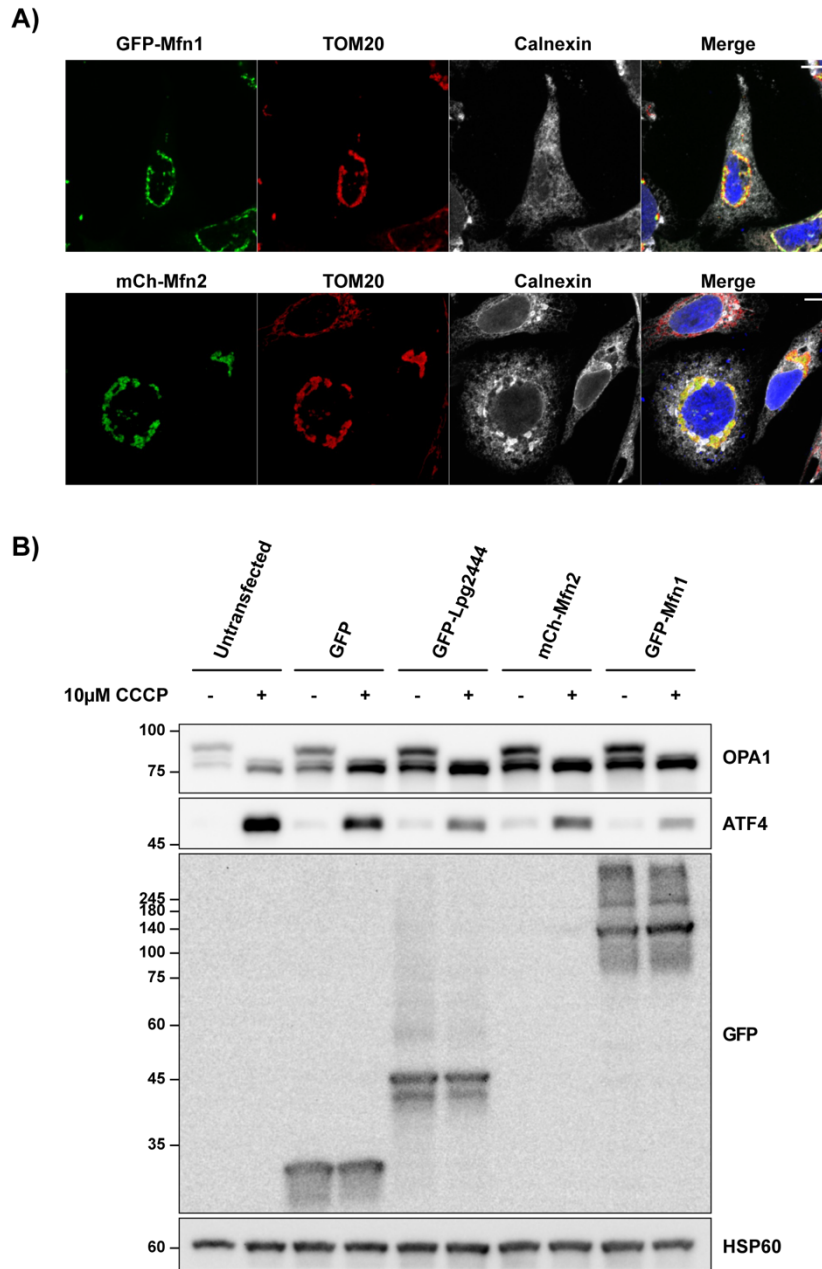
Figure 2.8: Overexpression of mitofusins phenocopies mitochondrial hyperfusion and stress resistance observed during Lpg2444 expression. (A) HeLa cells were transfected with GFP-Mfn1 or mCh-Mfn2, fixed, and stained for the indicated structures. Merge also contains DAPI stain. **(B)** HEK293 cells were transfected with the indicated construct, treated with 10μM CCCP for 4 hours, and analyzed via immunoblot. An anti-mCherry immunoblot is missing validating expression of the mCh-Mfn2 strain.

We next sought to identify the connection between mitochondrial hyperfusion and resistance to stress signaling during membrane depolarization. In our preprint, we show that GFP-Lpg2444 transfected HEK293 cells experience a less membrane depolarization during CCCP treatment compared to GFP-transfected control cells (Noack et al., 2020). This data is in line with past work that has demonstrated hyperfused mitochondria to have higher OXPHOS efficiency, and therefore a better ability to resist membrane decoupling (Giacomello et al., 2020; Westermann, 2012). In contrast, our data showing cleavage of L-OPA-1 isoforms during CCCP treatment of GFP-Lpg2444 transfected cells suggests that mitochondrial stress proteases are fully active, despite the lesser degree of membrane depolarization. Since mitochondrial stress proteases are known to be responsive to changes in membrane potential (Rainbolt et al., 2016), and cleavage of DELE1 is a prerequisite for mitochondrial stress signaling through the ISR (Guo et al., 2020), we hypothesized that mitochondrial stress proteases may be capable of selectively cleaving some targets (i.e. L-OPA-1) prior to DELE1 depending on the degree of membrane depolarization. In order to test this hypothesis, we employed a HEK293T cell line stably expressing DELE1-mClover in a safe harbor locus (Gift of Dr. Martin Kampmann's lab at UCSF). This cell line was successfully used in past research to monitor DELE1 cleavage during mitochondrial stress (Guo et al., 2020). We then transfected these cells with either mCherry or mCherry-Lpg2444, treated them with a gradient of CCCP concentrations for 4hr, and assessed the cleavage of L-OPA-1 and DELE1 via Western blot. As expected, CCCP treatment at increasing concentrations lead to increasing OPA1 and DELE1 cleavage, as well as increased upregulation of ATF4 (**Figure 2.9**). Surprisingly, longer exposures exposed a small fraction of uncleaved L-OPA-1 and DELE1 in the mCh-Lpg2444 transfected during 7.5μM CCCP treatment. This result suggests that mitochondrial stress proteases cannot preferentially cleave L-OPA1 prior to DELE1, and that mitochondrial stress protease activation is lesser in mCh-Lpg2444 transfected cells.
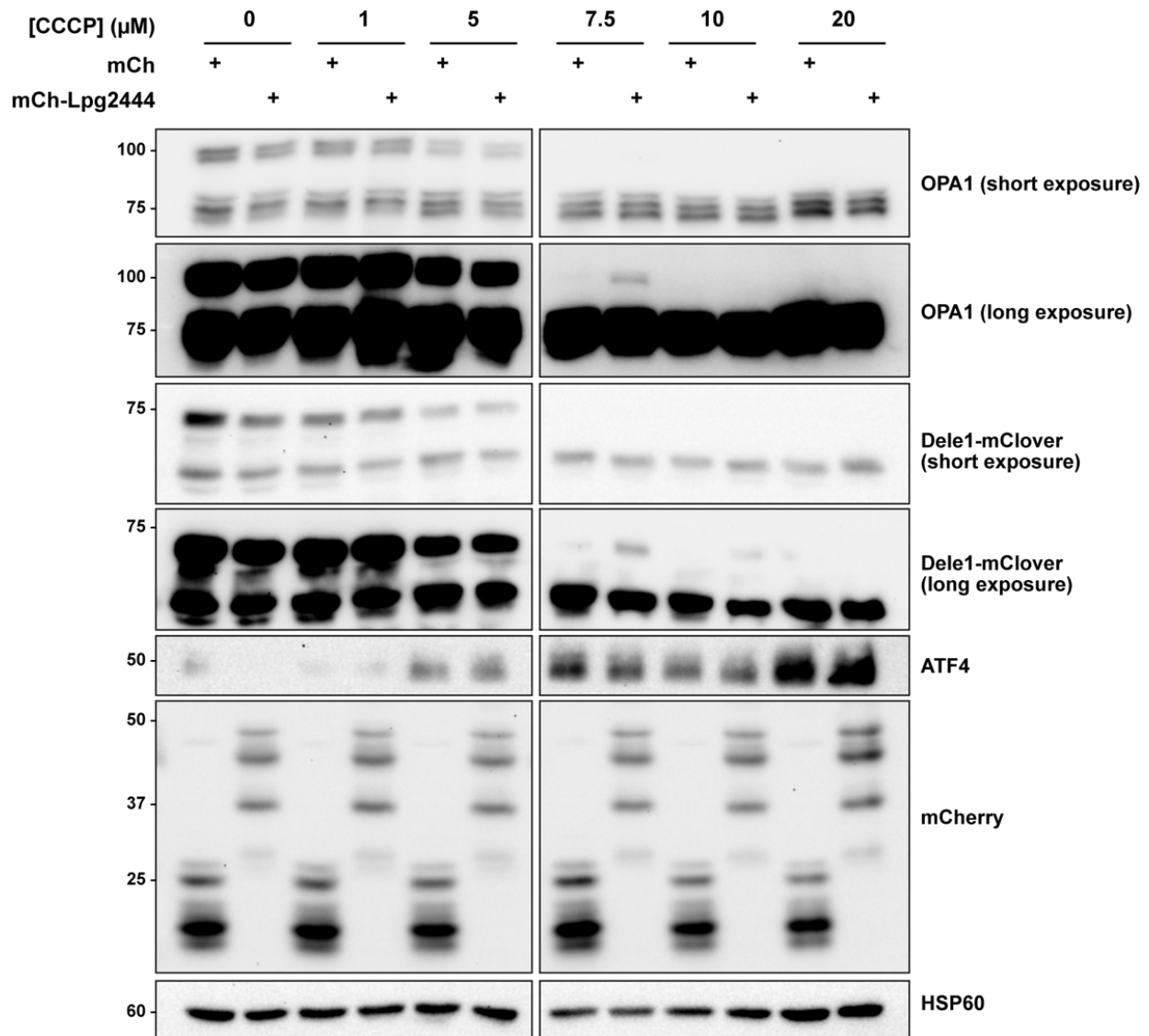
Figure 2.9: Lpg2444 attenuates mitochondrial depolarization during CCCP treatment. HEK293T DELE1-mClover cells (Gift from Dr. Martin Kampmann) were transfected with mCherry or mCherry-Lpg2444 and treated with the indicated concentration of CCCP for 4 hours. Samples were analyzed via immunoblot.

Altogether, our data support a model in which Lpg2444-induced hyperfusion confers resistance to CCCP due to a higher baseline membrane potential and/or greater ability for mitochondrial OXPHOS machinery to resist depolarization. Although our initial result (**Figure 2.6**) seemed to indicate differences in ATF4 upregulation despite complete cleavage of L-OPA1, we note that mitochondrial stress protease activation appears to be incredibly sensitive to increasing CCCP concentrations (**Figure 2.9**). Capturing slight differences in protease activation (as evaluated by

49

uncleaved substrates) requires careful Western blotting and long exposure time. As demonstrated by our work, these slight differences in protease activation can result in drastic differences in ATF4 upregulation between control and Lpg2444-transfected cell lines.

2.5.3   Lpg2444 cannot rescue mitochondrial fusion in fusion machinery KO cell lines

We next decided to explore the mechanisms by which Lpg2444 localizes to mitochondria. In our preprint, we show that Lpg2444 has a putative C-terminal membrane anchor/C-terminal domain. In order to test if the C-terminal region of Lpg2444 is responsible for mitochondrial targeting and hyperfusion, we created a truncation mutant of Lpg2444 containing the C-terminal half of the protein (Lpg2444$_{104-205}$-GFP), and ectopically expressed it this construct in HeLa cells. Lpg2444$_{104-205}$-GFP was capable of both mitochondrial localization and hyperfusion (**Figure 2.10A**), suggesting that the N-terminal region may be dispensable for function.

Since ectopic expression of Lpg2444 leads to the hyperfusion of mitochondria, we decided to test if Lpg2444 could rescue the activity of mitochondrial proteins involved in fusion. In order to test for this activity, we transfected GFP-Lpg2444 into WT, Mfn1$^{-/-}$, Mfn2$^{-/-}$, OPA1$^{-/-}$ MEF cells (Gift from Dr. Jodi Nunnari) and used immunofluorescence microscopy to evaluate the hyperfusion of mitochondria. In all cases, Lpg2444 was unable to induce fusion of fragmented mitochondria in the three knockout cell lines, suggesting that Lpg2444 does not possess intrinsic membrane fusion activity (**Figure 2.10B**). Several additional observations arose from this experimentation. First, in OPA1$^{-/-}$ MEFs, we noticed GFP-Lpg2444 rings surrounding mitochondria. This suggests that Lpg2444 may have a mitochondrial outer membrane localization, although more work is required to confirm this. Second, GFP-Lpg2444 expression did not induce the strong hyperfusion phenotype in WT MEFs that is observed in HEK293 and HeLa cells. While this may be a product of lower expression level, it also indicates that MEF cells may be more resistant to the fusion-inducing activities of Lpg2444.
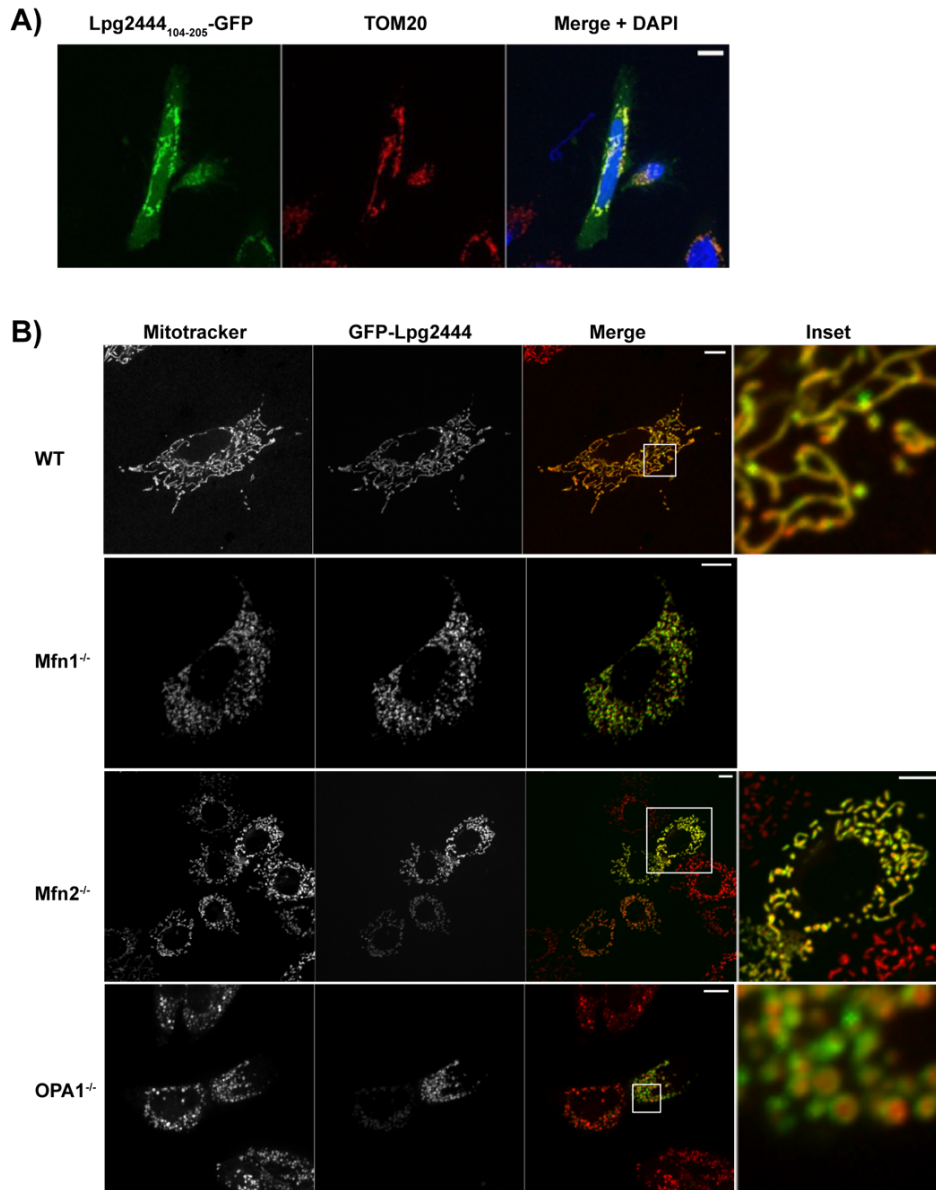
Figure 2.10: Lpg2444 localizes to mitochondria via C-terminal determinants and cannot rescue fusion activity of the mitofusins or OPA1. (A) HeLa cells were transfected with Lpg2444104-205-GFP, fixed, and immunostained. **(B)** MEF cells (Gift from Dr. Jodi Nunnari) were transfected with GFP-Lpg2444, stained with Mitotracker Far Red FM, and imaged.

2.5.4 Lpg2444: Conclusion and future directions

Although the activity of Lpg2444 remains elusive, progress was made towards its characterization. Since *Legionella* infection induces mitochondrial fission in human macrophages (Escoll et al., 2017), we suspect it is unlikely that Lpg2444 confers resistance to mitochondrial

stress during infection through some fusion based mechanism. Our work suggests that Lpg2444 localizes to mitochondria through C-terminal sequence determinants, and may be localized to the outer mitochondrial membrane. Attempts to determine the localization of Lpg2444 during infection were unsuccessful (data not shown), however, so it remains to be determined if Lpg2444 possesses mitochondrial localization during infection. Intriguingly, bioinformatic analysis from Dr. Nnejiuwa U. Ibe, a previous graduate student in the lab, determined that Lpg2444 shares homology with zinc metalloproteases (see Dr. Nneji Ibe Dissertation, Table 3.1). Although protease activity was not tested in the experimentation in this study, it is a promising direction for future work towards the characterization of this effector.

2.5.5   *Pitfalls of using the ΔdotA-WT log2FC values for analysis*

In the analysis presented in this chapter, we used the Δ*dotA*-WT comparison to analyze our data to determine changes in the host cell proteome induced by secreted *Legionella* effectors. This comparison was used in lieu of the WT-Control comparison, in which peptide counts detected from WT infected samples are compared to peptide counts in uninfected control cells. The use of the Δ*dotA*-WT comparison has one key advantage: the elimination of regulatory events common to both Δ*dotA* and WT infections from downstream analyses, as log2FC values for these events will fall below the cutoff of ±1. Although this is helpful in the enrichment of regulatory events induced by *Legionella* effectors rather than events induced through innate immune reaction to the presence of a bacterial pathogen, there are two important considerations to keep in mind. First, the underlying mechanisms behind a certain shared regulatory change (i.e. a protein upregulation) can potentially be dramatically different between Δ*dotA* and WT infections. Second, imputed regulatory events can falsely be interpreted as upregulations, for example, when they are actually downregulations. More specifically, when using the Δ*dotA*-WT comparison, a regulatory event considered an imputed downregulation during WT infection is an event for which peptides were undetected in WT samples, but detected in Δ*dotA* samples. However, an alternate

hypothesis exists, in which peptides were detected in Δ*dotA* samples due to an imputed upregulation during Δ*dotA* infection. To resolve between these hypotheses, the detection or absence of the peptides in the control condition ultimately determines if the regulatory event was an imputed downregulation during WT infection, or an upregulation during Δ*dotA* infection. Due to the prevalence of imputed values in our dataset, we chose to reanalyze the data using both the WT-Control and Δ*dotA*-Control comparisons in **Chapter 3**. Although this is a more intensive process, and regulatory events must be checked against between the two infection conditions prior to making a claim about effector dependence, it more accurately captures changes on the host cell induced by WT or Δ*dotA* infection.

2.6   Materials and methods

2.6.1   Cell lines

HEK293T cells (female), HEK293 cells (female) stably expressing the Fcγ receptor IIb (HEK293 FcγR cells) (Gifts from the lab of Dr. Craig Roy at Yale University) were cultured in Dulbecco's Modified Eagle's Medium (DMEM, GIBCO) containing 10% fetal bovine serum (FBS, VWR). U937 cells were cultured in RPMI containing 10% FBS. HEK293 DELE1-mClover cells (Gift from the lab of Dr. Martin Kampmann at UCSF) were cultured in DMEM containing 10% FBS. Mouse embryonic fibroblast WT, Mfn1$^{-/-}$, Mfn2$^{-/-}$, OPA1$^{-/-}$ (Gifts from the lab of Dr. Jodi Nunnari at UC Davis) were cultured in DMEM containing 10% FBS. All cells were incubated at 37°C and 5% CO_2.

2.6.2   Bacterial Strains

The *L.p.* strains LP01 WT and LP01 *ΔdotA* (Gifts from the lab of Dr. Craig Roy at Yale University) were cultivated on Charcoal Yeast Extract (CYE) agar plates or ACES Yeast Extract (AYE) medium.

2.6.3   Infection of cultured mammalian cells with L.p.

Infections with *L.p.* were performed as previously described (Treacy-Abarca and Mukherjee, 2015). *L.p.* heavy patches grown for 48 h on CYE plates were used for overnight liquid cultures in AYE medium supplemented with 0.33 mM Fe(NO$_3$)$_2$ and 3.3 mM L-cysteine until reaching an OD600 of ~3. *L.p.* from the overnight culture was enumerated and the appropriate amount was opsonized with *L.p.*-specific antibodies at a dilution of 1:2000 in cell growth medium for 20 min. HEK293 FcγR were grown on poly-lysine coated cell culture plates to a confluency of 80% and infected with the *L.p.* WT strain or the isogenic *ΔdotA* mutant strain at an MOI of 1-100 as indicated. The infection was synchronized by centrifugation of the plates at 500xg for 5 min. Cells were washed three times with warm PBS after 1 h of infection and fresh growth medium was added. Cells were collected for down-stream processing at the indicated timepoints.

2.6.4 Sample preparation for proteomics analysis

HEK293 FcγR infected for 1 h or 8 h with the *L.p.* WT strain or the isogenic *ΔdotA* mutant were infected at an MOI of 100. Uninfected HEK293 FcγR cells were included as a control. Cells were washed with ice-cold PBS, collected and the pellet was frozen at -80°C. Cell pellets were lysed by probe sonication in three pulses of 20% amplitude for 15 s in a lysis buffer consisting of: 8 M urea, 150 mM NaCl, 100 mM ammonium bicarbonate, pH 8; added per 10 ml of buffer: 1 tablet of Roche mini-complete protease inhibitor EDTA free and 1 tablet of Roche PhosSTOP. In order to remove insoluble precipitate, lysates were centrifuged at 16,100 g at 4˚C for 30 min. A Bradford Assay (Thermo) was performed to measure protein concentration in cell lysate supernatants. 6 mg of each clarified lysate was reduced with 4 mM tris(2-carboxyethyl)phosphine for 30 min at room temperature and alkylated with 10 mM iodoacetamide for 30 min at room temperature in the dark. Remaining alkylated agent was quenched with 10 mM 1,4-dithiothreitol for 30 min at room temperature in the dark. The samples were diluted with three starting volumes of 100 mM ammonium bicarbonate, pH 8.0, to reduce the urea concentration to 2 M. Samples were incubated with 50 µg of sequencing grade modified trypsin (Promega) and incubated at room temperature with rotation for 18 hr. The sample pH was reduced to approximately 2.0 by the addition of 10% trifluoroacetic acid (TFA) to a final concentration of 0.3% trifluoroacetic acid. Insoluble material was removed by centrifugation at 16,000 g for 10 min. Peptides were desalted using SepPak C18 solid-phase extraction cartridges (Waters). The columns were activated with 1 ml of 80% acetonitrile (I), 0.1% TFA, and equilibrated 3 times with 1 ml of 0.1% TFA. Peptide samples were applied to the columns, and the columns were washed 3 times with 1 ml of 0.1% TFA. Peptides were eluted with 1.2 ml of 50% I, 0.25% formic acid. Peptides were divided for global protein analysis (10 µg), phosphopeptide enrichment (1 mg), or diGly-enrichment (remaining sample), and lyophilized.

2.6.5   Phosphopeptide enrichment by immobilized metal affinity chromatography

Iron nitriloacetic acid (NTA) resin were prepared in-house by stripping metal ions from nickel nitroloacetic acid agarose resin with 100 mM ethylenediaminetetraacetic acid, pH 8.0 four times. Resin was washed twice with water and 100 mM iron(III) chloride was applied four times. The iron-NTA resin was washed twice with water and once with 0.5% formic acid. Iron- NTA beads were resuspended in water to create a 25% resin slurry. 60 µl of Fe-NTA resin slurry was transferred to individual Silica C18 MicroSpin columns (The Nest Group) pre-equilibrated with 100 µl of 80% CAN, 0.1% TFA on a vacuum manifold. Subsequent steps were performed with the Fe-NTA resin loaded above the Silica C18 columns. Dry peptide samples were resuspended in a solution of 200 µl 75% I 0.15% TFA. Peptide samples were mixed twice with the Fe-NTA resin, allowing the peptides to incubate for 2 minutes between each mixing step. The resin was rinsed four times with 200 µl of 80% I, 0.1% TFA. In order to equilibrate the columns, 200 µl of 0.5% formic acid was applied twice to the resin and columns. Peptides were eluted from the resin onto the C18 column by mixing and incubating the Fe-NTA resin with 200 µl of 500 mM potassium phosphate, pH 7.0 for 2 minutes. The elution step was repeated once. Peptides bound to the C18 column were washed three times with 200 µl of 0.5% formic acid. The C18 columns were removed from the vacuum manifold and eluted twice by centrifugation at 1000g with 75 µl of 50% I, 0.25% formic acid. Peptides were dried with a centrifugal adaptor and stored at -20˚C until analysis by liquid chromatograph and mass spectrometry.

2.6.6   Di-glycine peptide enrichment by immunoprecipitation

Peptide samples were subjected to ubiquitin remnant immunoaffinity. 10 uL of PTMScan® Ubiquitin Remnant Motif (K-ε-GG) Antibody Bead Conjugate purification (Cell Signaling) slurry was used per 1 mg peptide sample. Ubiquitin remnant beads were washed twice with IAP buffer, then split into individual 1.7 mL low bind tubes (Eppendorf) for binding with peptides. Peptides were dried with a centrifugal evaporator for 12 hours to remove TFA in the elution. The lyophilized peptides were resuspended in 1 ml of IAP buffer (50 mM 4- morpholinepropnesulfonic acid, 10

mM disodium hydrogen phosphate, 50 mM sodium chloride, pH 7.5). Peptides were sonicated and centrifuged for 5 minutes at 16,100g. The soluble peptide supernatant was incubated with the beads at 4°C for 90 minutes with rotation. Unbound peptides were separated from the beads after centrifugation at 700g for 60 seconds. Beads containing peptides with di-glycine remnants were washed twice with 500 µL of IAP buffer, then washed twice with 500 µL of water, with a 700g 60s centrifugation to allow the collection of each wash step. Peptides were eluted twice with 60 µL of 0.15% TFA. Di-glycine remnant peptides were desalted with UltraMicroSpin C18 column (The Nest Group). Desalted peptides were dried with a centrifugal adaptor and stored at -20°C until analysis by liquid chromatograph and mass spectrometry.

2.6.7   Mass spectrometry data acquisition and analysis

Samples were resuspended in 4% formic acid, 4% acetonitrile solution, separated by a reversed-phase gradient over a nanoflow column (360 µm O.D. x 75 µm I.D.) packed with 25 cm of 1.8 µm Reprosil C18 particles with (Dr. Maisch), and directly injected into an Orbitrap Fusion Lumos Tribrid Mass Spectrometer (Thermo). Total acquisition times were 120 min for protein abundance, 100 min for phosphorylation, and 70 min for ubiquitylation analyses. Specific data acquisition settings are detailed in **Supplementary File 3**. Raw MS data were searched with MaxQuant against both the human proteome (UniProt canonical protein sequences downloaded January 11, 2016) and the *Legionella Pneumophila Philadelphia* proteome (downloaded July 17, 2017). Peptides, proteins, and PTMs were filtered to 1% false discovery rate in MaxQuant (Cox and Mann, 2008).

2.6.8   Functional enrichment and network analysis

For **Figure 2.1K**, a list of all significantly regulated proteins (adj.-p-value ≤ 0.05, |Log$_2$FC| ≥ 1) in WT *vs. ΔdotA*-infected cells in the AB dataset or in the combined UB/PH datasets was analyzed for significantly overrepresented gene ontology (GO) terms (Biological Processes) and biological pathways (KEGG, Reactome) with the g:Profiler g:GOSt tool (Raudvere et al., 2019). The g:SCS algorithm was selected for multiple testing correction. The *Homo sapiens* genome (only annotated

genes) was selected as the background gene list. For **Fig 2.2D**, a list of all kinases with predicted up-regulated activity in WT *vs. ΔdotA*-infected cells was analyzed for significantly overrepresented biological pathways (KEGG) and gene ontology (GO) terms (Biological Processes) using the stringApp in Cytoscape (Doncheva et al., 2019; Shannon et al., 2003). The false-discovery rate (FDR) was used for multiple testing correction. The *Homo sapiens* genome (only annotated genes) was used as the background gene list. For **Figs 2.4B, Sup Fig 2.4A**, and **Sup Fig 2.4B,** a list of significantly regulated mitochondrial proteins/proteoforms (adj.-p-value ≤ 0.05, $|Log_2FC|$ ≥ 0.5) in WT *vs. ΔdotA*-infected cells was analyzed for significantly overrepresented gene ontology (GO) terms, biological pathways, INTERPRO Protein Domains and Features and UniProt Keywords using the stringApp in Cytoscape (Doncheva et al., 2019; Shannon et al., 2003). The FDR was used for multiple testing correction. Mitochonodrial localization was determined using the MitoCarta 3.0 database (Rath et al., 2020). The *Homo sapiens* genome (only annotated genes) was used as the background gene list.

2.6.9 *Prediction of kinase activity and complex regulation*

Kinase activities and complex regulation were inferred from all significantly regulated phosphosites (adj.-p-value ≤ 0.05, $|Log_2FC|$ ≥ 1) in WT *vs. ΔdotA*-infected using PhosFate Profiler (Ochoa et al., 2016). The inferred kinase activities (branch color), p-values (node color) and substrate numbers (node size) were mapped on the human kinome tree with CORAL(Metz et al., 2018) for data visualization.

2.6.10 *Subcellular mapping of proteomics data*

For **Figs 2.3A-B**, the number of significantly regulated proteins (adj.-p-value ≤ 0.05, $|Log_2FC|$ ≥ 1) in WT *vs. ΔdotA*-infected cells (AB, UB and PH datasets combined) in each subcellular compartment was quantified based on their primary ECO or, if not available, on their documented subcellular localization in The Human Protein Atlas database (http://www.proteinatlas.org) (Thul et al., 2017). The range of regulated proteins was assigned to a color range and mapped on the host cell using a custom-designed template in Adobe Illustrator. For **Figs 2.3C** and **Sup Fig 2.3**,

a list of significantly regulated proteins (adj.-p-value ≤ 0.01, |Log$_2$FC| ≥ 1 (**Sup Fig 2.3**) or 2 (**2.3C**)) in WT *vs. ΔdotA*-infected cells (AB, UB and PH) with their primary subcellular annotation was imported into Cytoscape(Doncheva et al., 2019; Shannon et al., 2003) and proteins were colored according to their Log$_2$FC value. The outline of each represented protein reflects the regulated dataset (circle: AB, octagon: UB, rounded square: PH). The resulting graphics were then imported into custom-designed templates in Adobe Illustrator.

2.6.11 Cell lysis and immunoblot analysis

HEK293 FcγR cells grown on poly-lysine coated plates were treated as indicated, washed three times with ice-cold PBS and harvested with a cell scraper. The cell pellets were frozen at -80°C. Cell pellets were resuspended in RIPA buffer supplemented with cOmplete Protease Inhibitor Cocktail (Roche) and PhosSTOP (Roche) and lysed under constant agitation for 30 min at 4°C. Cell debris was removed by centrifugation at 12,000xg for 20 min at 4°C. Protein concentration was measured using the DC Protein Assay (Bio-Rad) or the Pierce™ BCA Protein Assay Kit (Thermo Fisher Scientific). For each sample, 20-30 µg of proteins were denatured in SDS sample buffer/5% β-mercaptoethanol at 95°C for 5 min, loaded on 8-12% SDS-polyacrylamide gels and separated by SDS-PAGE. Proteins were transferred to PVDF membranes (0.45 µm, Millipore) at 30 V, 4°C for 16 h. Membranes were washed with PBS-T (PBS/ 0.1% Tween-20 (Thermo Fisher Scientific)), blocked with 5% Blotting Grade Blocker Non Fat Dry Milk (Bio-Rad) for 1 h at room temperature and incubated with the primary antibodies diluted in blocking buffer/0.02% (w/v) sodium azide overnight at 4°C. The primary antibodies were diluted as follows: ATF3 1:1000 (Cell Signaling Technology), TIMM17A 1:1000 (Proteintech), OPA-1 1:1000 (Cell Signaling Technology), MRPP3 1:1000 (Proteintech), TIMM23 1:1000 (Proteintech), CHOP 1:500 (Cell Signaling Technology), ATF4 1:1000 (Cell Signaling Technology), HSP60 1:20000 (Proteintech), alpha-Tubulin 1:5000 (Proteintech), Phospho-c-Jun (Ser73) 1:1000 (Cell Signaling Technology), Phospho-eIF2a (Ser51) 1:1000 (Cell Signaling Technology), PEX14 1:2000 (Proteintech). Membranes were washed three times with PBS-T and incubated with Goat Anti-Mouse IgG (H+L)

HRP Conjugate (Thermo Fisher Scientific), Goat Anti-Rabbit IgG (H+L) (Thermo Fisher Scientific), HRP Conjugate, or Protein A HRP conjugate (Cell Signaling Technology) diluted at 1:5000 in blocking buffer for 45 min at room temperature. After three washes with PBS-T, membranes were incubated with Amersham ECL Western Blotting Detection Reagent (Global Life Science Solutions) for 1 min and imaged on a ChemiDoc Imaging System (BioRad).

2.6.12 RT-qPCR

HEK293 FcγR cells were grown on poly-lysine coated 6-well plates or 350 mm dishes and treated as indicated. After treatment, the medium was removed, and cells were lysed in TRIzol reagent for 5 min at room temperature. RNA was extracted using the Direct-zol RNA Miniprep Plus kit (Zymo Research) according to the manufacturer's instructions. For each sample, 500 ng RNA were used for cDNA synthesis with the SuperScript III kit (Invitrogen) using oligo(dT)20 primers. Transcript levels were analyzed by qPCR using the BioRad iTaq SYBR Green kit. For each reaction, 5 ng of cDNA was used. Three technical replicates for each sample were analyzed on the BioRad CFX384 Touch™ Real-Time PCR Detection System. Data were processed using the $\Delta\Delta C_t$ method.

2.6.13 Immunofluorescence

HEK293 FcγR or HeLa FcγR cells were grown on poly-lysine coated coverslips in 24well cell culture plates. Cells were treated as indicated, washed three times with PBS and fixed in 4% paraformaldehyde/PBS for 15 min at room temperature. All further steps were done at room temperature as well. Cells were then permeabilized with 0.1% Triton X-100/PBS for 20 min followed by blocking with 1% BSA/PBS for 1h. Cells were stained with primary antibodies diluted in 1% BSA/PBS for 1h, washed three times with PBS and stained with secondary antibodies diluted in 0.2% BSA/PBS for 45 min. Cells were then stained with Hoechst33342 at 1:2000 in PBS for 10 min and washed three times with PBS. Coverslips were dipped three times into purified ddH$_2$O to remove salts, dried and mounted on microscopy glass slides with Prolong Diamond antifade 5 (Thermo Fisher Scientific). Slides were cured overnight at room temperature and

imaged the next day on a spinning disk Eclipse Ti2-E inverted microscope (Nikon). The following

antibody dilutions were used: primary antibodies: ATF3 1:100 (Cell Signaling Technology), *L.p.*

1:2000 (Thermo Fisher Scientific), TOM20 1:200 (BD Biosciences); secondary antibodies: Goat

anti-Rabbit IgG (H+L) Highly Cross-Adsorbed Secondary Antibody, Goat anti-Mouse IgG (H+L)

Highly Cross-Adsorbed Secondary Antibody, Alexa Fluor 633 1:500 (Thermo Fisher Scientific) or

Alexa Fluor 488 1:500 (Thermo Fisher Scientific).

2.6.14 Cell transfections

Transfections of HEK293 and HeLa cells were performed with jetPRIME (Polyplus). HEK293

FcγR or HeLa FcγR cells were grown to 60% confluency and transfected according to the

manufacturer's recommendations. For transfection of plasmid DNA, 0.25 µg DNA was used for

24well plates, 1 µg DNA for 60 mm plates and 10 µg DNA for 150 mm plates. 24h after

transfection, cells were treated as indicated and analyzed or harvested. MEF cells were grown to

50-70% confluency in 35 mm glass bottom dishes and were transfected with Lipofectamine 2000

(Invitrogen).

2.6.15 Quantification and Statistical Analysis

Statistical analysis of quantifications obtained from MaxQuant was performed with the artMS

Bioconductor package (version 0.9) (Jimenez-Morales et al., 2019). Each dataset (proteome

phosphoproteome, and ubiquitinome) was analyzed independently. Quality control plots were

generated using the artMS quality control functions. The site-specific relative quantification of

posttranslational modifications required a preliminary step consisting of providing the ptm-

site/peptide-specific annotation ("artmsProtein2SiteConversion()" function). artMS performs the

relative quantification using the MSstats Bioconductor package (version 3.14.1) (Choi et al.,

2014). Contaminants and decoy hits were removed. Samples were normalized across fractions

by median-centering the Log_2-transformed MS1 intensity distributions (**Sup Fig 2.1B**). Log_2FC for

protein/sites with missing values in one condition but found in $\geq$2 biological replicates of the other

condition of any given comparison were estimated by imputing intensity values from the lowest

observed MS1-intensity across sample peptides (Webb-Robertson et al., 2015); p-values were randomly assigned between 0.05 and 0.01 for illustration purposes. Statistically significant changes were selected by applying a Log_2FC (>1.0 or <−1.0) and adjusted p-value (<0.05). Statistical analysis of imaging, qPCR and flow cytometry data was performed with GraphPad Prism 8. Comparisons of data were performed by one-way ANOVA and Tukey's multiple comparison test or by unpaired, two-tailed t-tests as indicated. p-values: ns $p > 0.05$, * $p \leq 0.05$, $p \leq 0.01$ **, $p \leq 0.001$ ***, $p \leq 0.0001$ ****.

2.6.16 *Data Availability*

The mass spectrometry data files (raw and search results) have been deposited to the ProteomeXchange Consortium (http://proteomecentral.proteomexchange.org) via the PRIDE partner repository with the dataset identifier PXD019217 (Vizcaíno et al., 2016).

2.7   Acknowledgements

2.8   Author Contributions

Conceptualization, S.M., V.B, J.N., D.J-M., D.L.S., and N.J.K.; Methodology, S.M., J.N., E.S., G.J., D.J-M., D.L.S., and N.J.K.; Data Curation, V.B., D.J-M., D.L.S., and J.N.; Validation, J.N., V.B.; Formal Analysis, V.B., D.J-M. and J.N.; Investigation, V.B., J.N., T.M.; Writing – V.B., J.N., T.M., S.M., D.L.S., and D.J-M.; Visualization, J.N, V.B., D.J.-M.; Funding Acquisition, S.M., D.L.S., and N.J.K.; Resources, S.M., D.L.S., and N.J.K.; Supervision, S.M., D.L.S., and N.J.K..

2.9 Supplementary Figures
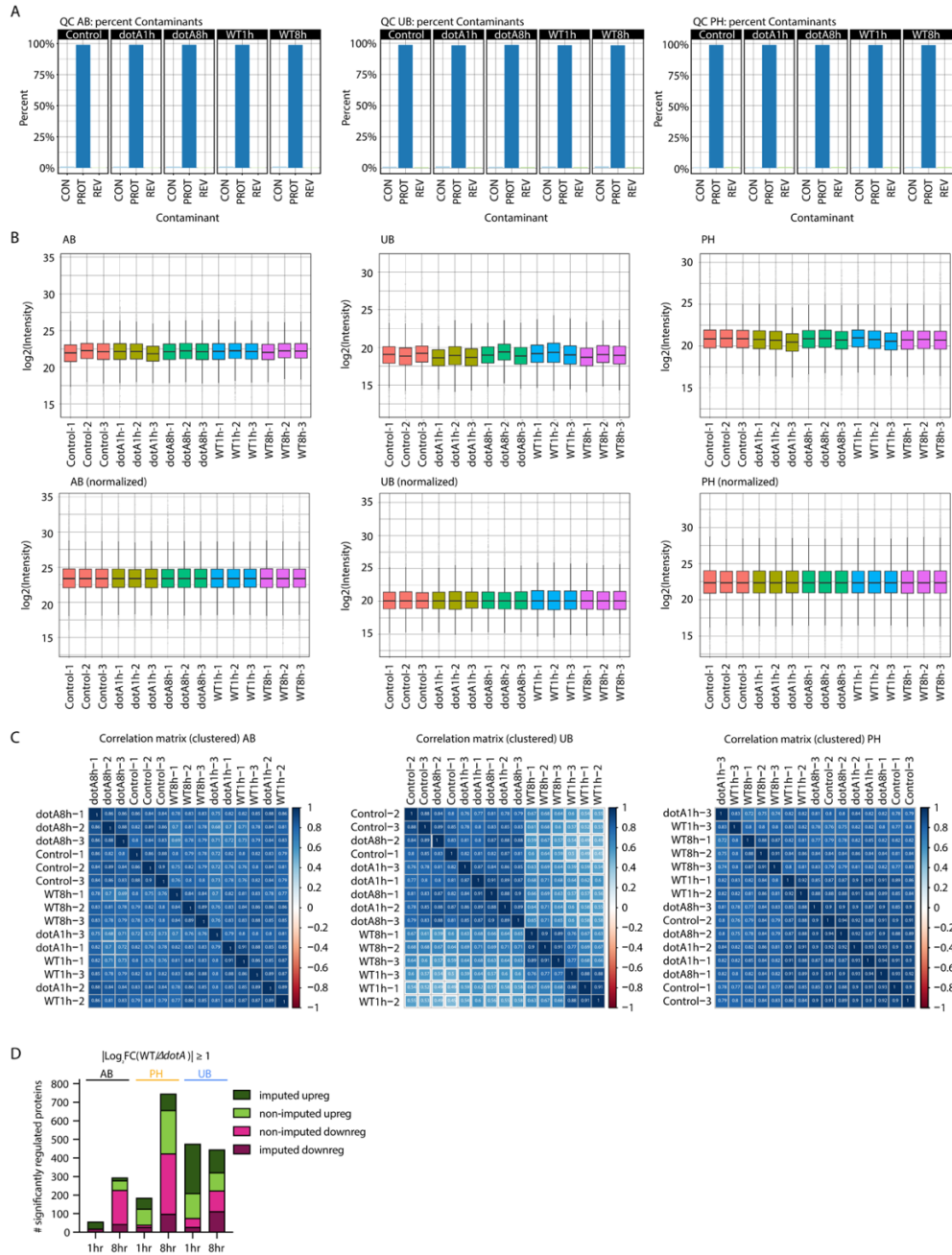
Supplementary Figure 2.1: Quantification and quality control plots of proteomics data. Related to Figure 2.1. Quality control plots for each dataset (AB, UB, PH) were generated using the artMS Bioconductor package (version 0.9) (Jimenez-Morales et al., 2019). **(A)** Percent of contaminants (CON), proteins (PROT) and reversed sequences (REV) in each experimental condition (control, dotA-1h, dotA-8h, WT-1h, WT-8h) were quantified to adjust the false-discovery-rate (FDR). **(B)** Samples were normalized across fractions by median-centering the Log2-transformed MS1 intensity distributions. **(C)** Correlation matrices showing the clustering of the different experimental conditions. **(D)** Elaboration on Figure 1C that differentiates between imputed regulations (darker shades) and non-imputed regulations (lighter shade).
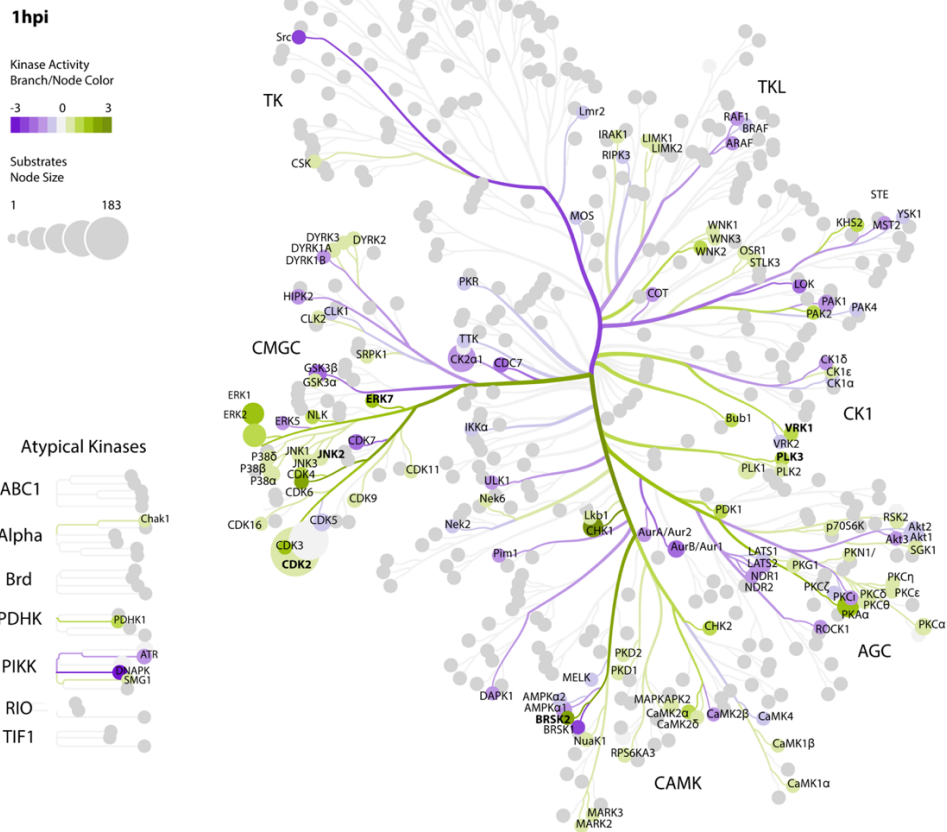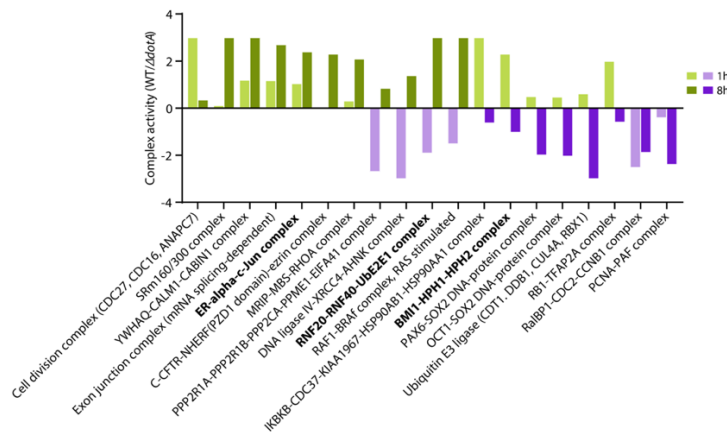
Supplementary Figure 2.2: Prediction of complex regulation in *L.p.* infected cells. Related to Figure 2.2. (A) Host cell kinase activities in WT- *vs. ΔdotA*-infected cells at 1hpi were inferred with PhosFate Profiler (Ochoa et al., 2016) based on regulated phosphorylated sites, and mapped on the kinase tree with CORAL (Metz et al., 2018). Kinase activity is indicated by the branch and node color, and the number of substrates by the node size. Names of kinase families are indicated around the tree. Kinases discussed in the text are highlighted in bold. **(B)** Based on the prediction of kinase activities, activities of protein complexes regulated by phosphorylation were inferred with PhosFate Profiler (Ochoa et al., 2016). The bar graph shows the most significantly regulated complexes (p-value ≤ 0.01) in WT- *vs. ΔdotA*-infected cells. Complexes discussed in the text are highlighted in bold.
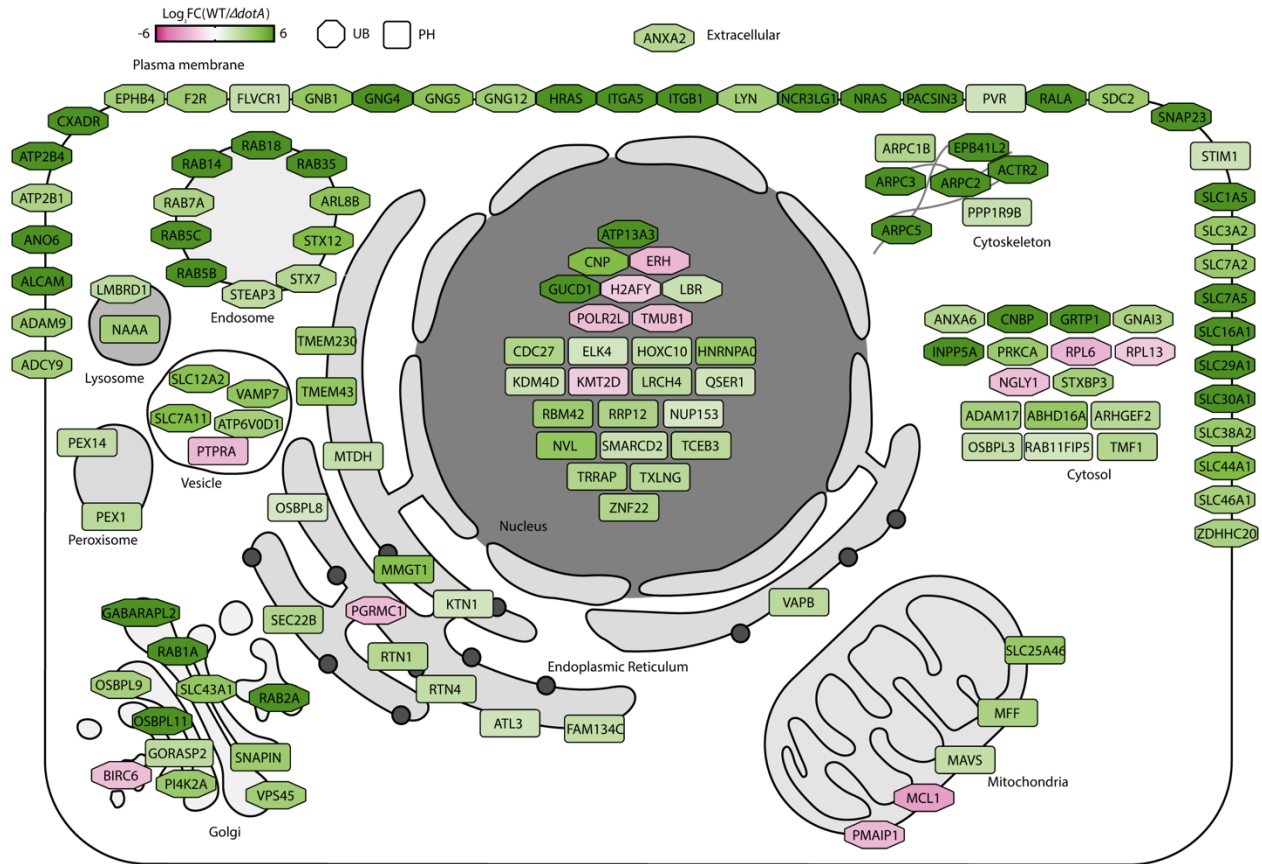
Supplementary Figure 2.3: Effector-dependent spatiotemporal proteomic changes at 1hpi. Related to Figure 2.3. Highly significantly regulated proteins (adj. p-value $\leq$ 0.01, |Log$_2$FC(WT/$\Delta dotA$)| $\geq$ 1) were mapped on the host cell organelles according to their primary ECO. The Log$_2$FC(WT/$\Delta dotA$) values are indicated by a color scale (green: up-regulated, purple: down-regulated), the dataset is indicated by the shape of the icon (octagon: UB, rounded square: PH). AB was not regulated at this significance cut-off.
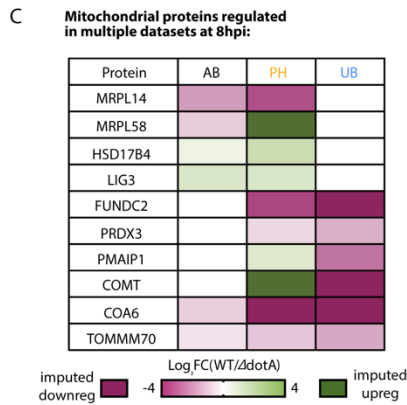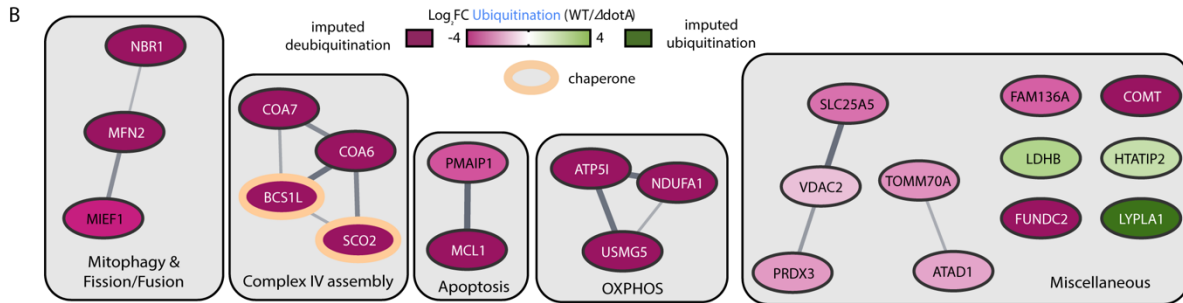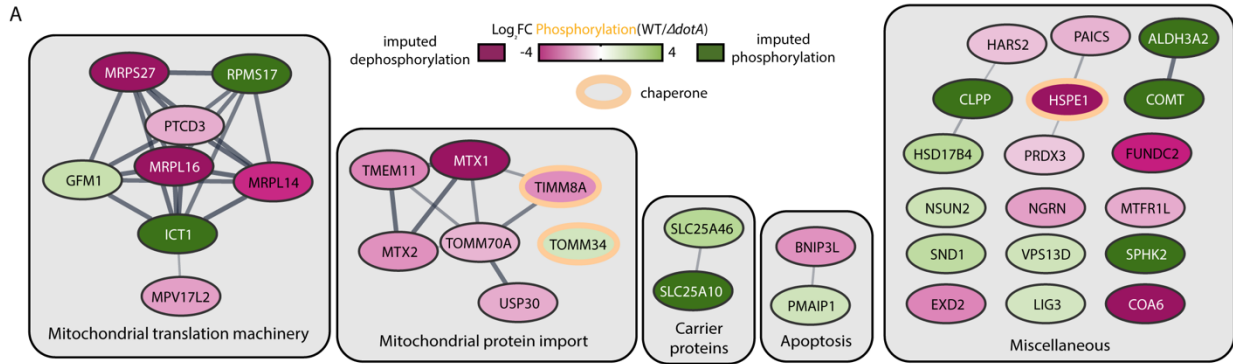
Supplementary Figure 2.4: TS44-dependent changes in the mitochondrial proteome in response to *L.p.* infection. Related to Figure 2.4. (A) Gene ontology enrichment and network analysis of mitochondrial proteins with significant phosphorylation changes in WT- *vs*. *ΔdotA*-infected cells at 8hpi was performed with the Cytoscape stringApp (Doncheva et al., 2019; Shannon et al., 2003). Clustering was performed using an MCL algorithm with an inflation value of 4. Colors represent protein upregulation (green) or downregulation (purple). Imputed phosphorylations and desphosphorylations were included in these analyses and are indicated in dark green and dark purple, respectively. Edges represent predicted functional associations. Clusters with overrepresented pathways or annotations from enrichment analyses are annotated. **(B)** Same as in (A) except for mitochondrial proteins with ubiquitination changes. **(C)** Mitochondrial proteins experiencing significant regulation across multiple datasets at 8hpi.
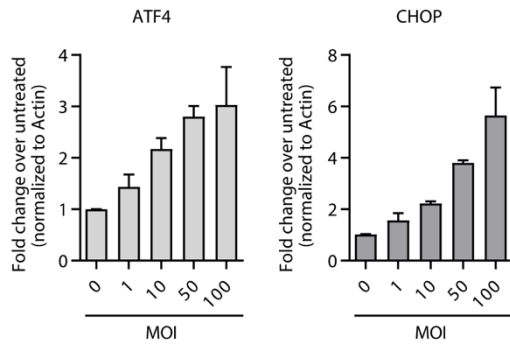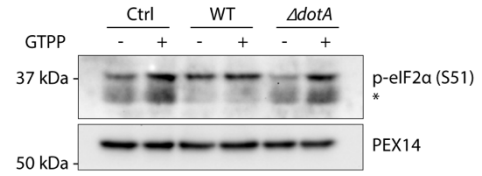
Supplementary Figure 2.5: Induction of mitochondrial stress markers during *L.p.* infection. Related to Figure 2.5. (A) HEK293 FcγR cells were infected with the indicated MOIs for 6h and transcript levels of *ATF4* and *CHOP* were analyzed by qPCR. Shown are the mean levels relative to the control ± SEM of n = 2-3 biological replicates. **(B)** Uninfected (Ctrl), WT- or *ΔdotA*-infected (MOI 25) HEK293 FcγR cells were treated with DMSO (-) for 6h, or GTPP (+, 10 μM) for 6h. Protein levels of p-eIF2α and PEX14 (loading control) were analyzed by immunoblot.

Chapter 3: Cross-family small GTPase ubiquitination by the intracellular pathogen *Legionella pneumophila*

3.1 Abstract

The intracellular bacterial pathogen *Legionella pneumophila* (*L.p.*) manipulates eukaryotic host ubiquitination machinery to form its replicative vacuole. While nearly 10% of *L.p.*'s arsenal of ~330 secreted effector proteins have been biochemically characterized as ubiquitin ligases or deubiquitinases, a comprehensive measure of temporally resolved changes in the endogenous host ubiquitinome during infection has not been undertaken. To elucidate how *L.p* hijacks ubiquitin signaling within the host cell, we undertook a proteome-wide analysis of changes in protein ubiquitination during infection. We discover that *L.p.* infection results in increased ubiquitination of host proteins regulating subcellular trafficking and membrane dynamics, most notably 63 of ~160 mammalian Ras superfamily small GTPases. We determine that these small GTPases undergo non-degradative ubiquitination, and link their ubiquitination to recruitment to the *Legionella*-containing vacuole membrane. Finally, we find that the bacterial effectors SidC/SdcA play a central role in cross-family small GTPase ubiquitination, and that these effectors function upstream of SidE-family ligases in the poly-ubiquitination and retention of GTPases in the LCV membrane. This work highlights the extensive reconfiguration of host ubiquitin signaling by bacterial effectors during infection and establishes simultaneous ubiquitination of small GTPases across the Ras superfamily as a novel consequence of *L.p.* infection. Our findings position *L.p.* as a tool to better understand how small GTPases can be regulated by ubiquitination in uninfected contexts.

3.2 Introduction

Legionella pneumophila (*L.p.*) is an intracellular bacterial pathogen that has proved to be a master manipulator of its eukaryotic hosts. It is the causative agent of Legionnaires' disease, a severe

pneumonia that affects immunocompromised patients upon exposure to contaminated aerosols. In the context of human disease, *L.p.* infects alveolar macrophages, but its preferred hosts include a wide range of protozoa, demonstrating the bacterium's ability to manipulate conserved eukaryotic processes to promote pathogenesis (Best and Kwaik, 2018; Gomez-Valero and Buchrieser, 2019). Phagocytosis by a permissive host cell triggers a complex pathogenic program in which *L.p.* avoids clearance by the endolysosomal system and instead remodels its plasma membrane-derived phagosome into an endoplasmic reticulum (ER)-like compartment called the *Legionella*-containing vacuole (LCV) (Hubber and Roy, 2010). Pathogenesis is mediated by an enormous arsenal of over 330 bacterial proteins ("effectors") injected into the host cell cytosol by *L.p.'s* Dot/Icm type IV secretion system (T4SS). Characterization of effector function has revealed numerous host targets, including membrane trafficking, autophagy, translation, and protein homeostasis (Lockwood et al., 2022; Qiu and Luo, 2017a). Despite these advances, many aspects of *L.p.*-mediated pathogenesis remain elusive, including the functions and targets of most effectors. Studying the effects of these proteins on host cell pathways offers a great potential for the discovery of novel pathogenic and cell biological mechanisms.

Among the many host cell proteins targeted by *L.p.*, small GTPases in the Ras superfamily have long been of interest. Small GTPases are found across eukaryotes, and subfamily members regulate essential cellular functions such as cell proliferation (e.g., Ras), intracellular membrane traffic (e.g., Rab, Arf), cytoskeletal structure (e.g., Rho, Rac), and nuclear import/export (e.g. Ran) (Cherfils and Zeghouf, 2013). Despite having disparate cellular functions, these proteins share a similar bimodal activity cycle: an active, membrane associated, GTP-bound state that allows for the interaction with GTPase-specific binding partners, and an inactive, cytosolic, GDP-bound state. The small GTPase activity cycle is highly regulated - GDP release is mediated by guanine nucleotide exchange factors (GEFs), and GTPase activity and subsequent inactivation is stimulated by GTPase activating proteins (GAPs) (Cherfils and Zeghouf, 2013). GTPase activity,

membrane association, and binding interactions can be further regulated by post-translational modifications (PTMs), providing an additional layer of modular control (Homma et al., 2021; Lei et al., 2021; Osaka et al., 2021). Given the essential roles small GTPases play in the eukaryotic cell and the diversity of regulatory mechanisms used to control GTPase function, pathogens often target GTPases through direct binding interactions and post-translational modifications (Aktories and Schmidt, 2014), and *L.p.* is no exception. The activity of small GTPases in the early secretory pathway, including Arf1, Sar1, and Rab1, has long been associated with formation of the LCV (Derré and Isberg, 2004; Kagan et al., 2004; Kagan and Roy, 2002). In addition, numerous effectors have been characterized with the ability to bind or post translationally modify various small GTPases, as well as recruit or remove small GTPases from the LCV membrane (Ingmundson et al., 2007; Kawabata et al., 2021; Machner and Isberg, 2006; Mukherjee et al., 2011; Müller et al., 2010; Murata et al., 2006; Nagai et al., 2002; Schoebel et al., 2011). Developing an understanding of how small GTPases are regulated during *L.p.* infection has informed a broader understanding of GTPase membrane targeting determinants as well as GTPase regulation via PTMs (Goody et al., 2017), positioning *L.p.* well as a tool to interrogate small GTPase regulatory mechanisms.

Another central element of *L.p.* pathogenesis is the manipulation of host cell ubiquitin signaling (Luo et al., 2021). Ubiquitin is a small, highly conserved, globular protein employed as a PTM to regulate a multitude of eukaryotic cellular processes, including protein degradation/turnover, cell cycle, innate immune signaling, and endocytosis (Komander and Rape, 2012; Yau and Rape, 2016). Ubiquitin is covalently attached to substrate protein lysines using ATP and the sequential activity of ubiquitin-activating (E1), ubiquitin-conjugating (E2), and ubiquitin ligase (E3) enzymes, and can be removed by deubiquitinating enzymes (DUBs). Lysines can be modified with a single ubiquitin (mono-ubiquitination) or with polymeric ubiquitin chains (poly-ubiquitination), resulting in

a vast array of regulatory outcomes depending on the site of ubiquitination, the ubiquitin chain length, and the linkage pattern of the ubiquitin chain that is formed (Komander and Rape, 2012). Almost 30 translocated *L.p.* effectors have been characterized to possess either ubiquitin ligase or deubiquitinase activity – a remarkable fact considering that ubiquitin is a eukaryotic protein (Luo et al., 2021). These include the paralogous ligases SidC and SdcA, which promote the recruitment of as yet unknown ubiquitinated substrates and ER-membranes to the LCV (Hsu et al., 2014; Luo and Isberg, 2004; Ragaz et al., 2008). SidC/SdcA also play a role in the ubiquitination of two small GTPases important for *L.p.* pathogenesis, Rab1 and Rab10, although how SidC/SdcA are involved and the consequences of ubiquitination on Rab1/10 are not yet known (Horenkamp et al., 2014; Jeng et al., 2019; Liu et al., 2020). The repertoire of secreted ubiquitin ligases also includes the SidE family (SidE, SdeA, SdeB, SdeC), which catalyze non-canonical phosphoribosyl-ubiquitination, entirely bypassing the host E1-E2-E3 cascade (Bhogaraju et al., 2016; Qiu et al., 2016). A growing list of *L.p.* DUB effectors includes LotC/Lem27, which may regulate the deubiquitination and recruitment of Rab10 (Liu et al., 2020). The tight relationship between *L.p.* pathogenesis and ubiquitin has been further demonstrated by studies connecting host ubiquitin pathways to efficient translocation of effectors through the Dot/Icm T4SS (Ong et al., 2021), ubiquitin binding to the activation of the effector VpdC involved in vacuolar expansion (Li et al., 2022), and effector secretion to the suppression of ubiquitin-rich DALIS structures involved in antigen presentation by immune cells (Ivanov and Roy, 2009).

Thus far, one study has attempted to develop a global understanding of changes in the host ubiquitinome during infection using a proteomic approach. This study revealed that *L.p.* utilizes the ubiquitin-proteasome system to downregulate innate immunity pathways and mTOR signaling during infection (Ivanov and Roy, 2013). However, the proteomic approach used relied on stable cell lines expressing tagged ubiquitin, which are prone to non-specific ubiquitination (Emmerich and Cohen, 2015; Peng et al., 2017). Modern ubiquitinomics approaches instead rely upon

diGlycine enrichment, which can be used to detect endogenous ubiquitination events in the absence of tagged ubiquitin overexpression (Mertins et al., 2013; Xu et al., 2010). This technique has been employed to perform global analyses of host cell ubiquitinome changes during *Salmonella* Typhimurium and *Mycobacterium tuberculosis* infections (Budzik et al., 2020; Fiskin et al., 2016), but has not yet been used for *L.p.*-infected cells. In addition, because distinct subsets of effectors function during early and late stages of *L.p.* infection (Oliva et al., 2018), a dynamic, temporal profile of host protein ubiquitination changes has been needed to more deeply understand the regulatory mechanisms at play during infection. We set out to provide an unbiased global analysis of ubiquitin dynamics during *L.p.* infection, identifying key proteins and processes targeted during *L.p.* infection for ubiquitination and deubiquitination.

To identify proteins with changing ubiquitination status across the span of *L.p.* infection, we undertook a proteome-wide analysis of protein ubiquitination at 1- and 8-hours post-infection using diGlycine enrichment and mass spectrometry. Additionally, we quantified protein abundance for the pre-enriched samples as a quality control, and to identify potential degradative versus non-degradative signaling ubiquitination. Strikingly, we discovered that at least 63 of approximately 160 mammalian small GTPases across all subfamilies are ubiquitinated, but not degraded, during infection in a process dependent upon bacterial effector secretion. Importantly, a growing body of work has found that many small GTPases in the Ras superfamily can be regulated via ubiquitination outside of the context of infection, resulting in profound impacts on their activity consequential for human disease (Lei et al., 2021). This suggests that *L.p.* may co-opt existing host regulatory mechanisms to control small GTPase function for its own benefit - an exciting prospect, given that the mechanisms and consequences of ubiquitination remain poorly defined for many small GTPases. Additionally, the degree of simultaneous cross-family small GTPase ubiquitination observed in our proteomics is, to our knowledge, unprecedented. We determine that small GTPases are targeted with both mono- and high molecular weight

polyubiquitination during *L.p.* infection, and that ubiquitination is likely non-degradative. Using the small GTPases Rab1, Rab5, and Rab10 as test cases, we demonstrate that robust recruitment of these GTPases to the LCV membrane is a requirement for their ubiquitination. We find that effectors SidC and SdcA are necessary for the ubiquitination of Rab5 and GTPases beyond the Rab subfamily, including RhoA and HRas. . Intriguingly, SidC/SdcA are also required for Rab5 recruitment to LCV, suggesting a complex interplay between SidC/SdcA activity, small GTPase membrane association, and ubiquitination. Finally, we determine that effectors in the SidE family function downstream of SidC/SdcA to promote Rab1 and Rab5 poly-ubiquitination, which facilitates their retention in the LCV membrane. Altogether, our data suggest that *L.p.* modulates small GTPases during infection through the concerted activity of several effectors, resulting in prolific, cross-family small GTPase ubiquitination and retention of GTPases at the LCV membrane. Our work positions *L.p.* as a tool to better understand how small GTPases can be regulated by ubiquitination in uninfected contexts.

3.3 Results

3.3.1 *L.p. infection induces T4SS-dependent ubiquitinome changes in the host cell*

To identify host cell components and pathways targeted with ubiquitin during *L.p.* infection, we performed a global proteomics analysis of protein ubiquitination changes in *L.p.*-infected cells. We chose HEK293 cells stably expressing the FcγRIIb receptor (HEK293 FcγR cells), as HEK293 FcγR have been used extensively in previous studies of *L.p.* pathogenesis and efficiently internalize antibody-opsonized *L.p*. (Black et al., 2019; Moss et al., 2019; Mukherjee et al., 2011; Qiu et al., 2016; Treacy-Abarca and Mukherjee, 2015). Cells were left uninfected or infected with either wild-type (WT) *L.p.* or the non-pathogenic *L.p.* Δ*dotA* strain (**Fig 3.1A**). For temporal resolution, infected cells were lysed at 1- or 8-hours post infection (hpi). Extracted proteins from these five conditions (uninfected control, WT 1hr, WT 8hr, Δ*dotA* 1hr, Δ*dotA* 8hr) were trypsinized

and processed with diGlycine (diGly) remnant enrichment, which is found upon protein modification with ubiquitin. While diGly enrichment also captures peptides modified with the ubiquitin-like proteins NEDD8 and ISG15, these peptides make up only a small fraction of the total enriched pool (~5%) (Kim et al., 2011). It is important to note that this enrichment strategy can identify only canonically ubiquitinated sites; phosphoribosyl ubiquitination mediated by the SidE family will not be detected. Enriched peptides were then subjected to mass spectrometric analysis and quantified with appropriate adjustments made based on quality control metrics (see Materials and Methods, **Supplementary File 3**, **Sup Fig 3.1-1A-B**). Peptide intensities between all three biological replicates per condition showed a robust reproducibility with correlation coefficients ranging from 0.80 to 0.91 (**Sup Fig 3.1-1C**). To capture the overall similarities and differences between the five experimental conditions, we performed a Principal Component Analysis (PCA). PCA identified a larger correlation between uninfected control and Δ*dotA* relative to WT (**Sup Fig 3.1-1D**). This indicates that, as expected, most changes in the ubiquitinome during infection are driven by effector secretion from *L.p.* WT.
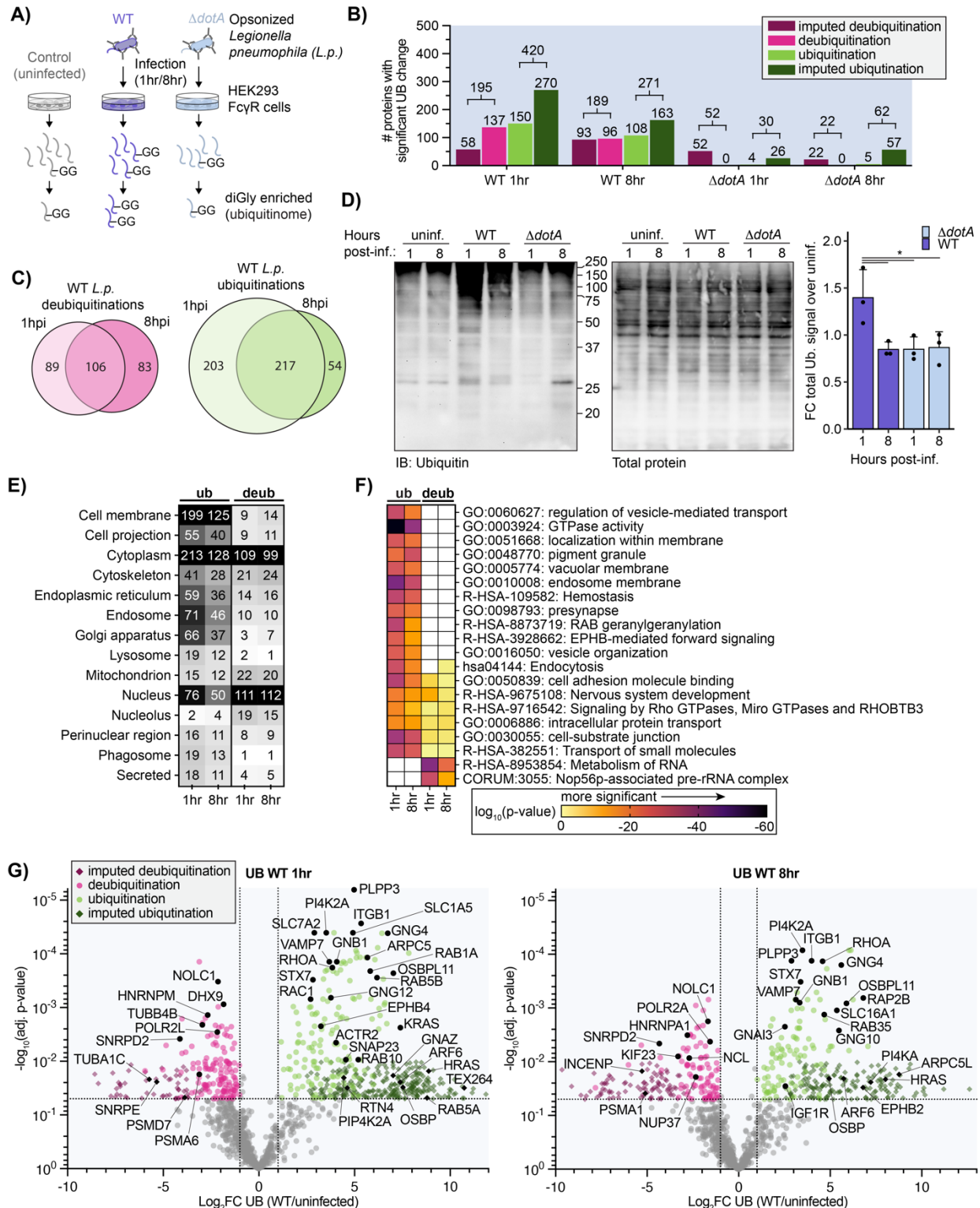
Figure 3.1: *L.p.* infection induces T4SS-dependent ubiquitinome changes in the host cell.
(A) Schematic of experimental procedures. (B) Counts of proteins with a significant increase
(green) or decrease (magenta) in ubiquitination compared to uninfected control for the indicated
infection conditions. *Figure caption continued on the following page.*

Figure caption continued from previous page. (Significance threshold for all subsequent analysis: |log2(FC)|>1, p<0.05, see note in text on use of imputation in this dataset). (C) Overlap of proteins with a significant increase (green) or decrease (magenta) in ubiquitination compared to uninfected control in the 1-hour vs 8-hour WT *L.p.* infected conditions. (D) Immunoblot analysis of the total pool of ubiquitinated proteins in HEK293T FcγR cells infected with WT or Δ*dotA L.p.* for 1 or 8 hours, or left uninfected. Invitrogen No-Stain protein labeling reagent was used to quantify total protein before immunoblot analysis. Total ubiquitin signal was first normalized to total protein for each sample, then the fold change over the appropriate uninfected sample was calculated. Data was subjected to a one-way ANOVA followed by a post-hoc Tukey-Kramer test for pairwise comparisons (* = p<0.05, n=3). (E) Subcellular localization analysis of proteins with a significant increase or decrease in ubiquitination compared to uninfected control during WT *L.p.* infection for 1 or 8 hours. (F) Pathway and protein complex analysis of proteins with a significant increase or decrease in ubiquitination compared to uninfected control during WT *L.p.* infection for 1 or 8 hours. Terms not significantly enriched for a given experimental condition are represented by white boxes. Analysis performed using Metascape (see methods). (G) Volcano plot representation of all ubiquitinome data in WT vs uninfected comparison at 1- and 8-hours post-infection. Imputed values are shown as diamonds. Significance threshold is indicated by the dotted line.

We next determined how ubiquitination was changing for individual proteins between the different conditions. We calculated the Log2 fold changes (Log2FC), corresponding p-values, and adjusted p-values for all detected proteins across all pairwise combinations of conditions (uninfected, WT and Δ*dotA* infected). Unsurprisingly, we encountered many instances in which a peptide was uniquely detected in one of the conditions while missed in the other one (e.g., a novel protein ubiquitination detected in WT infected but not uninfected control cells). Log2FC and adjusted p-values were calculated for these events using a suitable imputation strategy in which the missing peptide intensity value was assigned from the threshold of detection (see Methods). The full dataset for changes in protein ubiquitination, as well as a dataset containing changes at specific diGly sites (ubiquitin sites tab) can be found in **Supplemental Table 2.** In our subsequent analyses, we focused on four comparisons: WT1hr-Control, WT8hr-Control, Δ*dotA*1hr-Control, and Δ*dotA*8hr-Control (hereafter referred to as WT1hr, WT8hr, Δ*dotA*1hr, and Δ*dotA*8hr). Significant ubiquitination was determined using joint thresholds of |Log2FC| ≥ 1, adj.-p-value < 0.05.

Using these significance criteria, we analyzed changes in host protein ubiquitination during WT and Δ*dotA* infections. In accordance with the strong WT *L.p.*-induced ubiquitination signature shown by our PCA, we detected hundreds of proteins with significant ubiquitination changes during WT *L.p.* infection, in stark contrast to the few changes induced during Δ*dotA* infection (**Fig 3.1B**). The number of ubiquitinated proteins was highest early in WT *L.p.* infection, with 420 proteins ubiquitinated at 1hpi and 271 at 8hpi. In addition, we note that 80% (217 of 271) proteins ubiquitinated at 8hpi were also ubiquitinated at 1hpi, demonstrating a high degree of overlapping ubiquitination at early and late timepoints **(Fig 3.1C)**. Analysis of total ubiquitinated proteins during infection by Western blotting confirms our proteomic data, showing significantly higher levels of ubiquitinated proteins during WT infection compared to Δ*dotA*, as well as a decrease in ubiquitination at 8hpi (**Fig 3.1D**).

To better understand which subcellular compartments were most targeted with ubiquitination or deubiquitination, we used subcellular localization identifiers from UniProt to tabulate the number of significantly regulated proteins per compartment (**Fig 3.1E**). In addition, we performed biological pathway and protein complex enrichment (**Fig 3.1F, Supplemental Table 6)**. Subcellular localization analysis demonstrated the ubiquitination of hundreds of proteins with cytosolic or cell membrane localization, as well as endosomes, the endoplasmic reticulum, and the Golgi apparatus **(Fig 3.1E)**. Closer study of the enrichment results reveals increased ubiquitination in pathways supporting secretory and endocytic membrane trafficking, cytoskeletal dynamics, and membrane biology **(Fig 3.1F)**. Several of the most strongly enriched terms related to small GTPases and GTPase activity, namely "GTPase activity" and "RAB geranylgeranylation". Further analysis of ubiquitinated proteins revealed proteins in almost all subfamilies of the Ras superfamily of small GTPases, including RAB, RAS, RHO/RAC, RAN, ARF/SAR GTPases (**Fig 3.1G, Supplemental Table 2**). While *L.p.* effectors are known to manipulate several of these small GTPases during infection, including Arf1, Rap1, Rab1, Rab10, Rab33b, and Ran (Jeng et

al., 2019; Liu et al., 2020; Nagai et al., 2002; Qiu et al., 2016; Rothmeier et al., 2013; Schmölders et al., 2017; Steiner et al., 2018), the targeting of numerous small GTPases with ubiquitination is unprecedented. Regulatory small GTPase ubiquitination is known to occur in uninfected contexts (Lei et al., 2021), suggesting possible widespread manipulation of small GTPase signaling during *L.p.* infection. GTPase ubiquitination during WT infection extended to numerous heterotrimeric G proteins (**Fig 3.1G**). This included alpha (GNA11/13/I1/I2/I3/O1/Q/Z), beta (GNB1/2/4), and gamma (GNG4/5/7/10/12) subunits, as well as several regulators of heterotrimeric G protein signaling (RGS17/19/20). Although the role of heterotrimeric G protein signaling has not been studied extensively in the context of *L.p.* infection, it is known that G proteins are important for phagocytosis of *L.p.* in amoeba (Fajardo et al., 2004) and that multiple G proteins are found on the surface of the LCV in proteomic datasets (Hoffmann et al., 2014). Ubiquitination of heterotrimeric G protein subunits can result in a wide variety of signaling outcomes (Dewhurst et al., 2015; Dohlman and Campbell, 2019; Torres, 2016), suggesting *L.p.* or the host cell may modify G protein signaling via ubiquitination during infection.

We also detected ubiquitination on other proteins or pathways known to be targeted by *L.p.* effectors but not known to be targeted with ubiquitination. These include numerous regulators of the actin cytoskeleton (ARPC1B/2/5/5L, ACTR2/3, BAIAP2), proteins involved in lipid exchange (OSBP, OSBPL3/8/9/11, PITPNA), lipid kinases (PI4KA, PI4K2A, PIP4K2A), as well as SNARES and membrane fusion regulators (STX3/6/7/10/12, SNAP23/29, VAPA, NAPA, VAMP7). Also ubiquitinated during infection were several proteins known to be modified with non-canonical ubiquitination by the SidE family of *L.p.* effectors – which is not detected by the diGly enrichment technique used here – including the ER-shaping proteins RTN4, FAM134C, and TEX264 (Shin et al., 2020). In addition, we identified ubiquitination on protein targets previously unknown to play roles in *L.p.* infection, including solute carrier transporters, tyrosine (EPHB1/2/4, FGFR2, IGF1R)

and serine/threonine-protein kinases (LIMK1, PKN2, TNIK, MINK1), and integrins (ITGA3/B1/B1BP1/B3).

In addition to protein ubiquitination, *L.p.* infection induced the deubiquitination of hundreds of proteins at both 1hpi (195 proteins) and 8hpi (189 proteins) (**Fig 3.1B**). Of these, 106 proteins were deubiquitinated at both timepoints, suggesting that early and late infection deubiquitination is targeted to many of the same proteins (**Fig 3.1C**). Unlike the strong ubiquitination of cell membrane proteins, proteins deubiquitinated during WT infection primarily localized to the nucleus and the cytoplasm (**Fig 3.1E**). Pathway enrichment analysis of deubiquitinated proteins showed minimal overlap with pathways targeted by ubiquitination, suggesting that protein populations targeted for ubiquitination and deubiquitination during infection are distinct (**Fig 3.1F**). In line with a distinct, nuclear-enriched deubiquitination response, enrichment analysis primarily described deubiquitinated proteins with the two terms "Metabolism of RNA" and "Nop56p-associated pre-rRNA complex". These enrichments are driven in part by deubiquitination of numerous spliceosome proteins (HNRNPA1/C/K/M/U, SNRPD2/D3/E, SF3B3/B6), as well as transcription regulators (DHX9, POLR2A/2L) and the multifunctional proteins nucleolin (NCL) and NOLC1 (**Fig 3.1G**). Although none of these proteins are known targets of *L.p.* effectors, host cell transcription is known to be modulated by the *L.p.* effectors LegAS4/RomA (Rolando et al., 2013), LphD (Schator et al., 2023), LegA3/AnkH (Dwingelo et al., 2019), and SnpL (Schuelein et al., 2018) through a variety of mechanisms, suggesting that *L.p.* may employ additional effectors to target nuclear function. Intriguingly, we also observed the deubiquitination of numerous subunits of the proteasome (PSMA1/A6/B3/C1/C3/C5/D1/D7, ADRM1), which is known to be important for *L.p.* infection (Dorer et al., 2006; Price et al., 2011). We also noticed deubiquitination of several regulators of the RAN GTPase (RANBP2, RCC1) and associated proteins such as nuclear pore complex (NUP37/85/188, TPR), tubulin subunits (TUBA1C, TUBB, TUBB4B), the microtubule stabilizer CKAP2, and microtubule associated proteins (PCM1, INCENP, KIF23, CEP131). The

deubiquitination of these proteins is intriguing because *L.p.* is known to activate the Ran GTPase – promoting microtubule polymerization and LCV motility – with the effectors LegG1 and PpgA (Rothmeier et al., 2013; Simon et al., 2014; Swart et al., 2020). Altogether, *L.p.* induces the deubiquitination of hundreds of proteins over the course of infection on a population distinct from proteins targeted with ubiquitination.

In contrast to WT infection, Δ*dotA* induced few changes in both protein ubiquitination and deubiquitination at both 1 and 8hpi (**Fig 3.1B, Sup Fig 3.1-2**). The few changes that did occur during Δ*dotA* infection primarily occurred in the nucleus, cytoplasm, and cell membrane (**Sup Fig 3.1-2D**), and were described by terms known to relate to bacterial infection such as "Bacterial invasion of epithelial cells", "PID NFkappaB Canonical Pathway", "lytic vacuole" and "PCP/CE pathway" (planar cell polarity pathway) (**Fig 3.1-2E**) (Tran et al., 2014). The enrichment of these terms during Δ*dotA* infection indicates a strong antibacterial host response which is absent during WT *L.p.* infection, and serves as a confirmation that our proteomic analysis aligns with the biology of the system.

Given the tight relationship between protein ubiquitination and degradation, we compared host cell protein ubiquitin changes to changes in abundance. To do this, we analyzed our pre-diGly enriched cell lysates via mass spectrometry and quantitated changes in host protein abundance. As with our ubiquitinomics, peptide intensities showed robust reproducibility and PCA distinctly separated WT infected cells from uninfected and Δ*dotA* infected cells (**Sup Fig 3.1-3**). Log2 fold changes, corresponding p-values, and adjusted p-values for all detected proteins across all pairwise combinations of conditions were computed and analyzed and can be found in **Supplemental File 2 (abundance tab)** and **Sup Fig 3.1-4A-D.** To compare protein ubiquitination and abundance changes, we plotted ubiquitination Log2FC values against abundance Log2FC for all detected proteins at 1hpi and 8hpi (**Sup Fig 3.1-4E**). As above, we used a significance

cutoff of |Log2FC| ≥ 1, adj.-p-value < 0.05 to determine proteins significantly changing in abundance, ubiquitination, or both abundance and ubiquitination. Importantly, few proteins experienced significant changes in both abundance and ubiquitination simultaneously. This result serves as a quality control that changes in abundance are not responsible for detected changes in ubiquitination and suggests that ubiquitination largely does not result in protein abundance changes during infection.

3.3.2 *L.p. infection results in the ubiquitination of multiple Ras superfamily small GTPases*

Among the many ubiquitin-regulated pathways and proteins during infection, we were particularly intrigued by the ubiquitination of many small GTPases in the RAS superfamily. Previous studies have shown that *L.p.* uses ubiquitin to modify select small GTPases in the Rab subfamily. Two Rab proteins known to play important roles in pathogenesis, Rab1 and Rab10, are ubiquitinated during infection in a process dependent upon the paralogous effectors SidC and SdcA (Horenkamp et al., 2014; Jeng et al., 2019; Kagan et al., 2004). In addition, Rab33b is phosphoribosyl ubiquitinated by the SidE family of ligases (Qiu et al., 2016). Although the consequences of Rab1/10/33b ubiquitination are not known, both SidC/SdcA and SidE family effectors are associated with timely LCV formation, suggesting small GTPase ubiquitination may be part of a central *L.p.* pathogenesis program. Additionally, although small GTPases are known to be regulated by ubiquitination outside the context of infection, the simultaneous cross-family ubiquitination of these proteins is unprecedented and suggests that *L.p.* may exploit a GTPase regulatory mechanism common to the entire superfamily (Lei et al., 2021). Thus, we further investigated *L.p.*-induced cross-family small GTPase ubiquitination to learn more about *L.p.* pathogenesis, but also GTPase regulation more broadly.

We first identified the number and family range of small GTPases ubiquitinated during infection in our ubiquitin site dataset (**Supplemental File 2 - ubiquitin_sites tab**). Small GTPases in the Ras superfamily accounted for 132 of 868 significant ubiquitination sites (15.21%) at 1hpi, and 77 of 532 (14.47%) significant ubiquitination sites at 8hpi (**Fig 3.2A, Sup Fig 3.2-1**). Ubiquitination sites were detected on at least 63 of the approximately 163 known mammalian Ras superfamily small GTPases, falling on members of the ARF, RAN, RHO/RAC, RAS, and RAB subfamilies (**Sup Fig 3.2-2**). Many of these ubiquitination sites were imputed, suggesting that the ubiquitination of these proteins may result from *L.p.* effector activity (**Sup Fig 3.2-2**). While several of the small GTPases ubiquitinated during infection are known to be regulated by ubiquitin outside of the context of infection, these ubiquitination events are often transient and hard to detect (Duncan et al., 2022; Lachance et al., 2013; Sapmaz et al., 2019; Shin et al., 2017), suggesting that *L.p.* infection may ubiquitinate small GTPases at a higher frequency or with a greater stability than observed in uninfected cells. In contrast to WT infection, Δ*dotA* infection induced ubiquitination of few small GTPases, consistent with cross-family small GTPase ubiquitination being a process induced by secreted effectors.
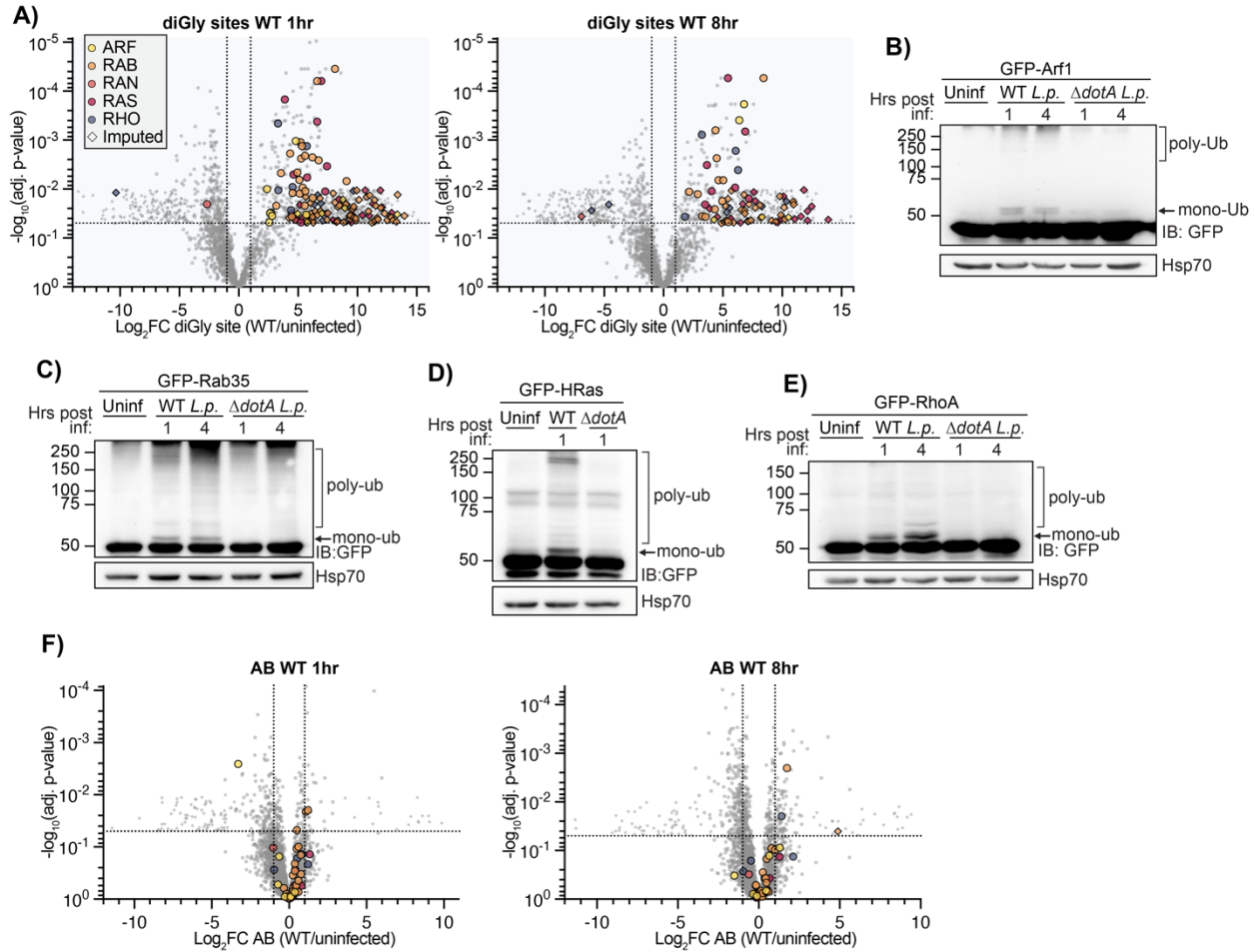
Figure 3.2: Small GTPases across the Ras superfamily are ubiquitinated during WT *L.p.* infection. **(A)** Volcano plot representation of diGlycine site dataset for WT *L.p.* vs. uninfected comparison at 1- and 8-hours post-infection. Each point represents a unique diGlycine enriched peptide; for some GTPases, multiple peptides were detected. Imputed values are shown as diamonds, and Ras superfamily subfamilies are differentiated by color. Significance threshold is shown by the dotted line. **(B)-(E)** Immunoblot analysis of lysates prepared from HEK293T FcγR cells transiently transfected with the indicated GFP-tagged small GTPase, then infected with either WT or Δ*dotA L.p.* for 1 or 4 hours, or left uninfected. Blots were probed with anti-GFP and anti-Hsp70 antibodies. **(F)** Volcano plot representation of abundance dataset as in (A).

Since our diGly enrichment ubiquitinomics strategy precludes determination of ubiquitin chain length, we assessed the ubiquitination of multiple Ras superfamily small GTPases via Western blot. We transfected HEK293T FcγR cells with a panel of GFP-tagged or Flag-tagged GTPases and infected them with WT or Δ*dotA L.p.*. We expected ubiquitinated GTPases to show the

appearance of bands in multiples of ~8.5kDa (molecular weight of a ubiquitin moiety) above the major, non-ubiquitinated species. Indeed, numerous GTPases in the ARF (ARF1, ARF6), RAS (HRas, Rap1, Rap2B), RHO (RhoA, RhoB, RhoC, RhoQ), and RAB (Rab6A, Rab9A, Rab20, Rab35) subfamilies showed a prominent mass shift consistent with mono-ubiquitination during WT but not Δ*dotA* infection (**Fig 3.2B-E, Sup Fig 3.2-3**). In many circumstances, we noticed multiple mass shifts above the unmodified band, as well as the accumulation of high molecular weight species. These bands are consistent with the conjugation of either extended polyubiquitin chains, or multiple monoubiquitin moieties to distinct lysine residues on these small GTPases (poly-monoubiquitination). The accumulation of both mono- and high molecular weight ubiquitinated species is also consistent with past experimentation on Rab1/10 ubiquitination during infection (Horenkamp et al., 2014; Jeng et al., 2019; Liu et al., 2020). Altogether, our results confirm the cross-family GTPase ubiquitination observed in our mass spectrometric data, and suggest that small GTPases are targeted for both mono- and poly-ubiquitination during infection.

To determine if cross-family small GTPase ubiquitination may promote degradation, we mined our AB dataset for changes in small GTPase abundance during infection (**Fig 3.2F**). Of the many detected GTPases, almost all fell below both the adj. p-value and the Log2FC significance cutoffs, suggesting that GTPases do not significantly change in abundance during infection. This result is consistent with past work demonstrating that *L.p.*-induced Rab1 ubiquitination is removed at later time points during infection in a proteasome-independent process (Horenkamp et al., 2014), and with past work on non-degradative small GTPase monoubiquitination (Kholmanskikh et al., 2022; Sapmaz et al., 2019). Consistent with this insight from our proteomics analysis, we do not see a decrease in small GTPase abundance across the time course of infection by Western blot for all small GTPases tested (**Fig 3.2B-E, Sup Fig 3.2-3, Fig 3.5**).

We next decided to explore small GTPase sequence and structure for clues regarding the impacts of ubiquitination. Towards this end, we aligned the sequences of the significantly ubiquitinated GTPases, annotated regions of interest, and marked all unique ubiquitination or deubiquitination sites from both 1 and 8hpi (**Sup Fig 3.3-1 – full alignment, Fig 3.3A – Rab1A only**). Regions of interest include: (1) the five conserved G boxes important for contact with GTP/GDP, (2) the Switch I and Switch II regions important for interaction between active GTPases and their downstream binding partners, (3) the C-terminal hypervariable domain (HVD) typically responsible for proper membrane targeting and subcellular localization, and (4) the five alpha helices and six beta sheets characteristic of most Ras superfamily small GTPases. We next defined 10 regions based on these conserved structural and functional elements. Within each region, we counted the number of WT *L.p.*-induced ubiquitin sites (**Fig 3.3B**). Surprisingly, most of the ubiquitination did not occur in Switch I / II regions (regions #3 and #5), known to be targeted with PTMs by many pathogens, including *L.p.*, to block interaction between active GTPases and their downstream binding partners (Aktories and Schmidt, 2014). Instead, 92 of 138 unique ubiquitination sites (~67%) were detected within the three C-terminal regions: the α4 helix (region #8, 35 sites), G5 box lysine (region #9, 21 sites), and α5/C-terminal hypervariable domain (region #10, 36 sites) (**Fig 3.3B**). Intriguingly, most work on small GTPase ubiquitination in uninfected contexts has determined ubiquitination to primarily fall within these regions (Kholmanskikh et al., 2022; Osaka et al., 2021; Steklov et al., 2018), suggesting that *L.p.* infection hijacks GTPase regulatory regions also targeted in the absence of infection.
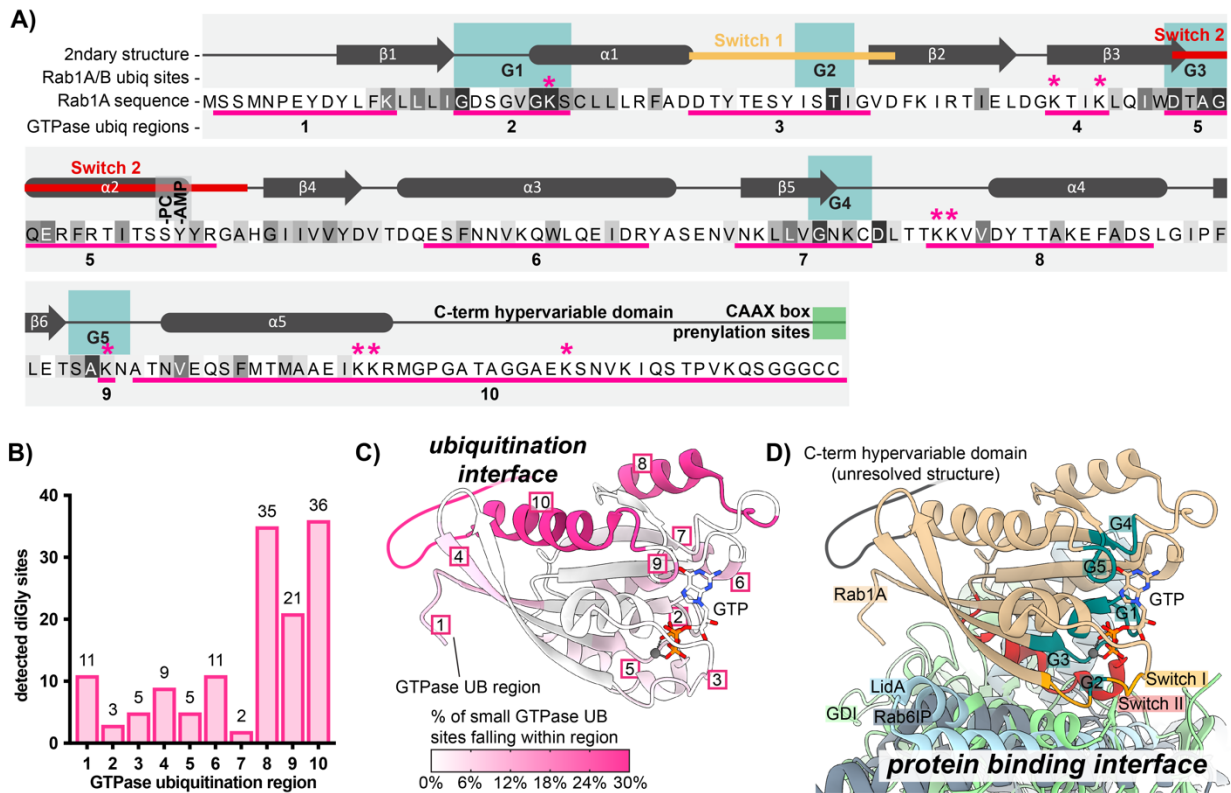
Figure 3.3: Small GTPase ubiquitinations cluster in the C-terminal region. (A) Schematic of small GTPase structural and functional regions, using Rab1A as an example. Regions frequently ubiquitinated across detected small GTPases are underlined in pink and numbered 1-10. Sequence colored by conservation within the small GTPase superfamily, from white (non-conserved) to black (extremely highly conserved residue); see full alignment in **Fig 3S1**. The "*" symbol indicates ubiquitination sites detected for Rab1A or Rab1B. The site of phosphocholination by *L.p.* effector AnkX (S79) is annotated as "-PC", while the site of AMPylation by *L.p.* effector DrrA (Y80) is marked as "-AMP". **(B)** Pooled counts of significant ubiquitinations detected in ubiquitination regions defined in (A) across all 63 ubiquitinated small GTPases. **(C)** Structure of Rab1A with the 10 structural/functional regions indicated. Regions are colored by percentage of detected small GTPase ubiquitin sites falling within a given region. **(D)** Alignment of structures for human Rab1A (tan) in complex with *L.p.* effector LidA (light blue), mouse Rab6 bound to its effector Rab6IP (gray), or yeast Rab1 homologue YPT1 bound to GDI (light green). Important structural and functional domains of Rab1A are colored and labeled. PDB accession numbers: 3TKL (Rab1A:LidA), 2BCG (YPT1:GDI), and 3CWZ (Rab6:R6IP1).

We next mapped ubiquitinated regions onto the structure of the small GTPase Rab1 (**Fig 3.3C, pink regions**). To visualize the relationship between these ubiquitinated regions, key functional regions, and protein binding interfaces, we also aligned the structure of Rab1 to structures of GTPases bound to several types of partners, including Rab1 bound to the *L.p.* secreted Rab-binding effector LidA, yeast YPT1 (Rab1 homologue) bound to GDI, and mouse Rab6 bound to

Rab6-interacting protein 1 (R6IP1) (**Fig 3.3D**). As expected, LidA, GDI, and R6IP1 predominantly form contacts with GTPases around the Switch I / II regions. To our surprise, the dominantly ubiquitinated regions #8, #9, and #10, localize to the distal face of Rab1, opposite protein binding regions. This result implies that cross-family small GTPase ubiquitination may not directly block GTPase-protein binding interactions, and instead, affect other intrinsic GTPase properties, such as membrane association, GTP/GDP binding, or GTP hydrolysis, or may affect protein binding interactions through an allosteric mechanism.

3.3.3 LCV-localized pools of Rab1 are targeted for ubiquitination

We next interrogated the driving forces behind small GTPase ubiquitination during infection more directly. Based on previous studies, we hypothesized that small GTPase ubiquitination may be spatially restricted to LCV-membrane localized pools of these proteins. First, past work on Rab1 has shown its ubiquitination at 1hpi and deubiquitination by 8hpi, which correlates with Rab1 LCV recruitment and removal (Horenkamp et al., 2014; Ingmundson et al., 2007; Kagan et al., 2004). Second, the effectors SidC/SdcA are known to control both Rab10 LCV recruitment and ubiquitination, suggesting a functional link between these two processes (Jeng et al., 2019; Liu et al., 2020). Finally, it is well established that the LCV accumulates ubiquitinated proteins throughout the first 6 to 8 hours of infection, indicating that the LCV membrane may be a site of ubiquitin ligase activity (Dorer et al., 2006; Ivanov and Roy, 2009).

In order to test our hypothesis, we manipulated the recruitment of Rab1 to the LCV during infection and assessed changes in Rab1 ubiquitination. Recruitment of Rab1 was manipulated by altering the activity of the *L.p.* effector DrrA (also known as SidM), which recruits Rab1 to the LCV at early timepoints during infection via the activity of a Rab1-specific GEF domain and retains Rab1 in the LCV membrane via the activity of its AMP-transferase, or AMPylation domain (Hardiman and Roy, 2014; Müller et al., 2010; Murata et al., 2006). Past work has demonstrated that a DrrA genomic

deletion *L.p.* strain *ΔdrrA* displays considerably reduced Rab1 recruitment to the LCV, and that DrrA AMPylation activity is required, as complementation with AMPylation-dead DrrA D110,112A fails to rescue Rab1 recruitment (Hardiman and Roy, 2014). Consistent with Rab1 LCV recruitment and retention being tied to its ubiquitination, we found considerably reduced levels of Rab1 mono- and polyubiquitination during infection with *L.p.* *ΔdrrA* and *L.p.* *ΔdrrA* + pDrrA D110,112A compared to *L.p.* WT (**Fig 3.4A-B**, quantitated as % change in normalized Rab1 monoubiquitination)*. Ubiquitination was rescued by complementation of *L.p.* *ΔdrrA* with a plasmid expressing WT DrrA. In contrast, DrrA knockout and AMPylation mutant strains had no effect on the ubiquitination of Rab10, suggesting that DrrA does not control the ubiquitination of GTPases not targeted by its GEF domain (**Sup Fig 3.4-1A-B**).
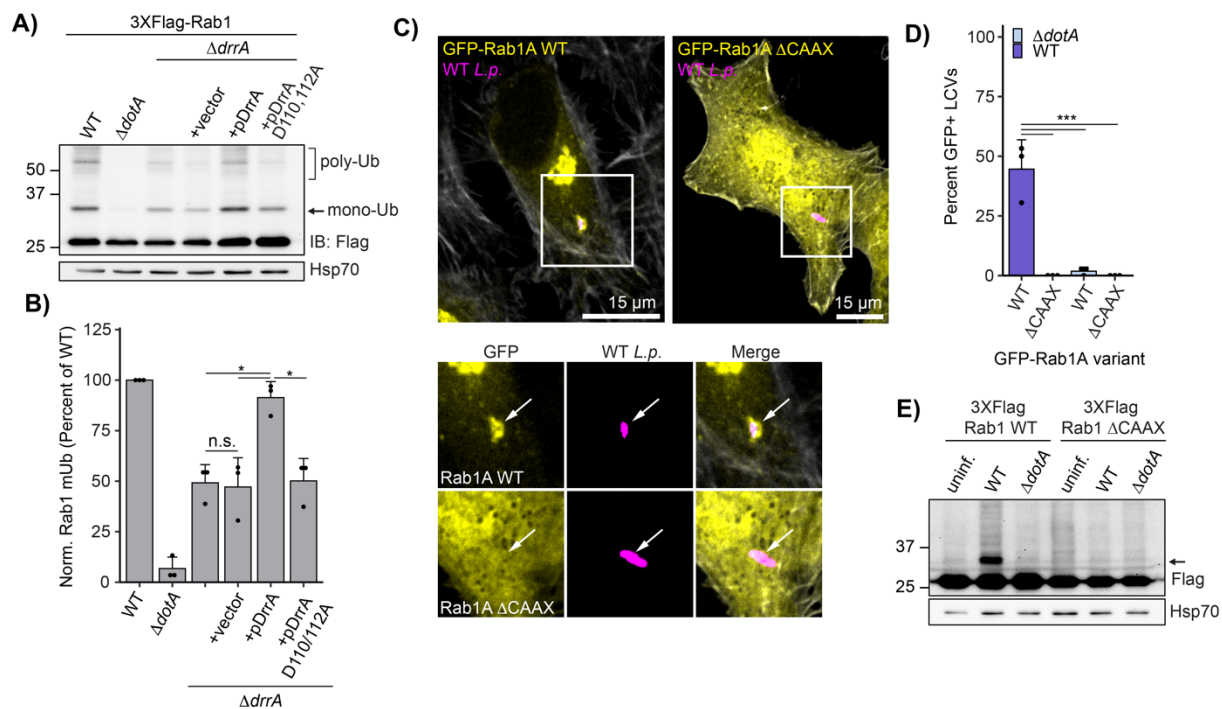
Figure 3.4: Rab1A is monoubiquitinated at the LCV membrane. (A) Immunoblot analysis of lysates prepared from HEK293T FcγR transfected with 3XFlag Rab1A and infected with a *ΔdrrA* *L.p.* strain panel (WT, *ΔdotA*, *ΔdrrA*, and *ΔdrrA* complemented with empty vector or plasmid encoded DrrA WT or D110, 112A) for 1 hour (MOI=50). Monoubiquitinated Rab1 indicated with an arrow. **(B)** Quantification of biological replicates (N=3) of experiment shown in (A). Normalized Rab1A monoubiquitination intensity was calculated as a percentage of WT *L.p.* infection levels (see Methods). *Figure caption continued on the following page.*

Figure caption continued from the previous page. **(C)-(D)** Immunofluorescence analysis of EGFP Rab1A WT or ΔCAAX LCV recruitment. HeLa FcγR cells were transfected with indicated construct, then infected for 1 hour with either WT or Δ*dotA L.p.* (MOI=1), fixed, and stained with anti-*Legionella* antibody. (C) Representative images, and (D) quantification of EGFP positive LCVs (percent of total scored per biological replicate, n=3, 25 LCVs scored/replicate). **(E)** Immunoblot analysis of monoubiquitination of Rab1A WT vs ΔCAAX during *L.p.* infection . HEK293T FcγR cells were transfected with either 3X Flag Rab1A WT or ΔCAAX, then infected with WT or Δ*dotA L.p.* for 1 hour (MOI=50), or left uninfected. Lysates were probed with anti-Flag antibody. Monoubiquitinated Rab1 indicated with an arrow. *For all graphs:* bars represent mean value, error bars represent standard deviation. Individual points are values from each biological replicate. *Statistical analysis of Western blot quantification*: one-way ANOVA followed by Tukey-Kramer post-hoc test for each pair of means. * = $p<0.05$, n.s. = $p>0.05$.

To further interrogate the relationship between Rab1 recruitment to the LCV membrane and its ubiquitination, we sought to prevent Rab1 association with membranes entirely. To this end, we generated a lipid anchor mutant of Rab1 by deleting its two prenylation sites: the C-terminal cysteines C204 and C205 (known as the CAAX box). As expected, Rab1 ΔCAAX showed fully cytosolic localization compared to the predominantly Golgi-localized WT Rab1 and was not recruited to the LCV membrane (**Fig 3.4C-D**). Consistent with LCV-membrane recruitment being a prerequisite for Rab1 ubiquitination, Rab1 ΔCAAX ubiquitination was entirely abolished during infection (**Fig 3.4E**). We note a similar loss of ubiquitination upon deletion of the Rab10 CAAX motif (**Sup Fig 3.4-1C**). Collectively, our data suggest that only LCV-localized pools of Rab1 are targeted for ubiquitination, and that membrane recruitment may be a prerequisite for infection-induced small GTPase ubiquitination.

3.3.4 Early endosomal GTPase Rab5 is recruited to the LCV and targeted for ubiquitination

Note: Experimentation and analysis performed by Adriana Steinbach redacted from Dissertation and summarized below.

Key Findings: The early endosomal GTPase Rab5 is ubiquitinated and recruited to the LCV during WT *L.p.* infection. As with Rab1/10, ΔCAAX mutation of Rab5 abrogates ubiquination entirely. Rab5 accumulation does not result in the recruitment of EEA1, suggesting that Rab5

accumulation does not result in increased trafficking of the LCV into the endosomal compartment. Overexpression of Rab5 decreases bacterial burden but does not increase the association of LAMP1 with the LCV, suggesting that Rab5-induced antagonization of infection does not occur through a mechanism of increased lysosomal trafficking.

3.3.5 Bacterial effectors SidC/SdcA are necessary but not sufficient for Rab5A monoubiquitination, and control Rab5A recruitment to the LCV

Next, we sought to identify bacterial effectors required for Rab5A ubiquitination. Previous studies have shown that bacterial effector paralogs SidC and SdcA are required for Rab1 (Horenkamp et al., 2014) and Rab10 (Jeng et al., 2019) ubiquitination. To determine if SidC/SdcA play similar roles in Rab5 ubiquitination, we infected HEK293T FcγR cells expressing Flag-Rab5A with SidC/SdcA knockout and complemented strains. Indeed, infection with a SidC/SdcA genomic deletion strain (*L.p.* Δ*sidC/sdcA*) fails to induce Rab5A ubiquitination, as indicated by the loss of mono-ubiquitinated species (**Fig 3.5A-B**). Transformation of the Δ*sidC/sdcA* strain with a plasmid encoding either SdcA or SidC is sufficient to rescue Rab5A monoubiquitination, suggesting that these effectors are functionally redundant in this context.
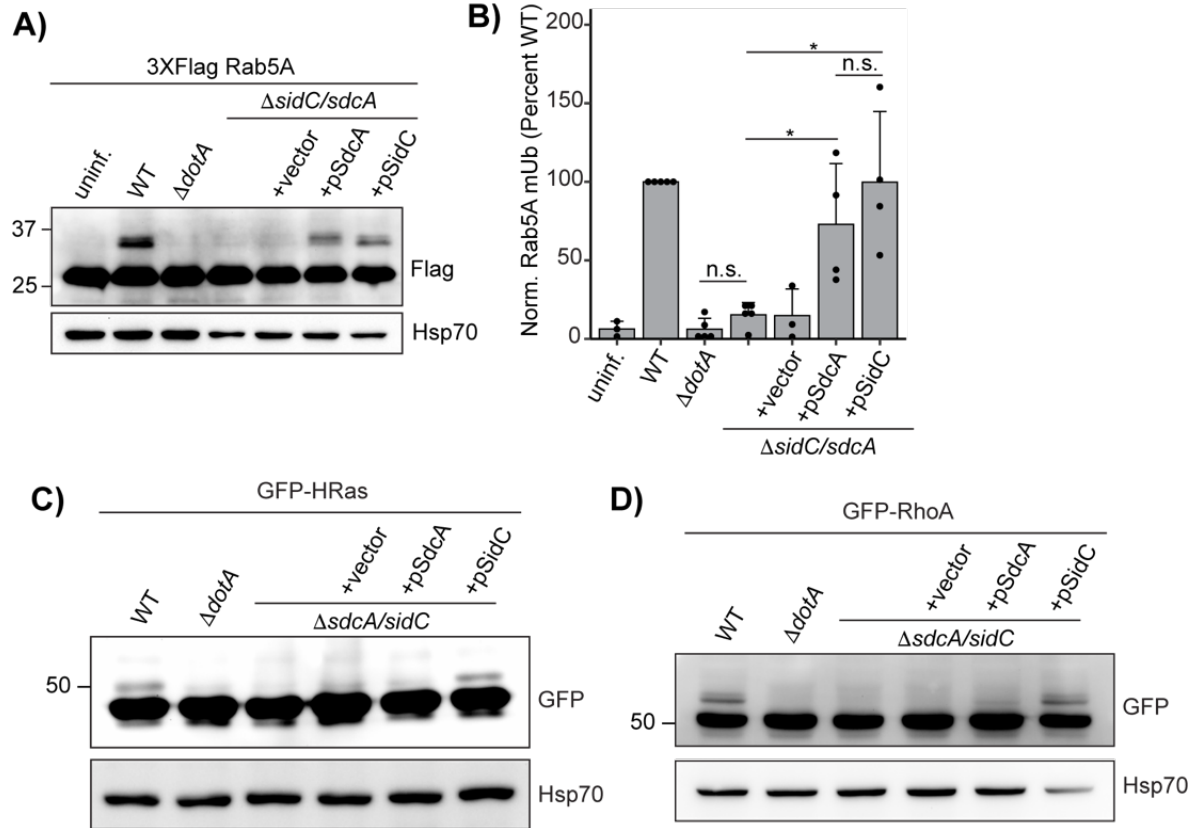
Fig 3.5: Bacterial effectors SidC/SdcA play a central role in small GTPase ubiquitination. **(A)** Immunoblot analysis of Rab5A monoubiquitination during infection with Δ*sidC/sdcA L.p.* strain panel (WT, Δ*dotA*, Δ*sidC/sdcA*, and Δ*sidC/sdcA* transformed with vector or plasmid expressing SdcA or SidC). HEK293T FcγR cells transfected with 3XFlag Rab5A were infected with the indicated strain or left uninfected. Cells were lysed at 4 hours post infection and probed with anti-Flag antibody. **(B)** Quantification of biological replicates (N=3-5) of experiment shown in (A). Normalized Rab5A monoubiquitination intensity was calculated as a percentage of WT *L.p.* infection levels (see Methods). Data was subjected to a one way ANOVA followed by a post-hoc Tukey-Kramer test for pairwise comparisons (* = p<0.05, n=3-4). **(C)** and **(D)** Ubiquitination of HRas and RhoA is differentially dependent and SidC and SdcA. HEK293T cells transiently expressing the indicated GFP-tagged small GTPase were infected with the Δ*sidC/sdcA L.p.* strain panel as in (A). Cells were infected for 1 hr and lysates probed with anti-GFP antibody. *Statistical analysis of LCV scoring quantification:* G test of independence was performed on pooled counts (positive vs. negative) from all biological replicates. Upon verifying significance (p<0.05), pairwise comparisons between strains were evaluated by post-hoc G-test using the Bonferroni-adjusted p-value as a significance threshold (p = 0.003). * = p<0.003, ** = p<0.0003, *** = p<0.00003, n.s. = p>0.003.

Note: Experimentation and analysis performed by Adriana Steinbach redacted from Dissertation

and summarized below.

Key Findings: Ectopic expression of the bacterial effectors and E3 ligases SidC/SdcA cannot induce ubiquitination of Rab5. SidC/SdcA regulate the recruitment of Rab5 to the LCV but do not promote recruitment of LAMP1.

3.3.6   SidC/SdcA promote small GTPase ubiquitination beyond the Rab subfamily

With the finding that SidC/SdcA regulate Rab5 ubiquitination, in addition to past work demonstrating their role in Rab1/10 ubiquitination, we hypothesized that SidC/SdcA may play a role in small GTPase ubiquitination beyond the Rab subfamily. To evaluate the role SidC/SdcA may play in cross-family small GTPase ubiquitination more broadly, we transfected HEK293T FcγR cells with GFP-tagged HRas and RhoA constructs and infected with SidC/SdcA knockout and complemented strains. Strikingly, infection with *L.p.* Δ*sidC/sdcA* abolished ubiquitination of both GTPases, while complementation of *L.p.* Δ*sidC/sdcA* with a plasmid encoding SidC but not SdcA rescued ubiquitination (**Fig 3.5C-D, Sup Fig 3.5-1A-B**). This result implicates SidC/SdcA in cross-family small GTPase ubiquitination more broadly. It also suggests that SidC/SdcA may play overlapping but distinct roles in small GTPase ubiquitination, as the ubiquitination of Rab1 seems to be primarily dependent upon the activity of SdcA (Horenkamp et al., 2014) (**Sup Fig 3.5-1C-D**), and the ubiquitination of Rab5 appears to be equally dependent upon SidC and SdcA (**Fig 3.5A-B**).

3.3.7   SidE family-mediated polyubiquitination facilitates small GTPase membrane retention

We next sought to identify additional effectors involved in small GTPase ubiquitination. Specifically, we were intrigued by recent work that has linked both the LCV recruitment and ubiquitination of Rab33b to the activity of non-canonical ligase effectors in the SidE family (SidE, SdeA, SdeB, SdeC) (Kawabata et al., 2021), leading us to hypothesize that the SidE family may play similar roles to SidC/SdcA in the recruitment and ubiquitination of small GTPases during

infection. To test if SidE family effectors influence Rab1 and Rab5 ubiquitination, we assessed Rab1/5 ubiquitination in HEK293T FcγR cells infected with WT *L.p.*, Δ*dotA*, and SidE family knockout or complemented strains. Strikingly, SidE family knockout showed no effect on Rab1 or Rab5 mono-ubiquitination but diminished high molecular weight poly-ubiquitinated species (**Fig 3.6A, Sup Fig 3.6-1A-B)**. Notably, SidC/SdcA knockout abrogates both mono- and polyubiquitination for Rab5 (**Fig 3.6A**) and Rab1 (**Sup Fig 3.6-1C**), suggesting that SidE-mediated poly-ubiquitination may lie downstream of SidC/SdcA activity.

Work performed by Ady Steinbach: We next assessed if the SidE family of effectors is necessary for Rab5 recruitment to the LCV. Immunofluorescence analysis shows that the Δ*sidE/sdeABC* LCV fails to accumulate endogenous Rab5A at one hour post-infection, whereas an Δ*sidE/sdeABC*strain complemented with SdeB expressing plasmid robustly recruits Rab5A (**Fig 3.6C-D**). This result suggests that Rab5 monoubiquitination, which is unaffected by the absence of SidE-family effectors, is not sufficient to retain Rab5 in the LCV membrane.

With poly-ubiquitination but not mono-ubiquitination associated with the retention of Rab5 in the LCV membrane, we hypothesized that poly-ubiquitinated GTPases may associate more stably with cellular membranes. To test this hypothesis, we performed subcellular fractionations of cells expressing Flag-Rab1 or Rab5 and infected with *L.p.* WT or Δ*dotA*. Monoubiquitinated species of both Rabs distributed between the membrane and the cytosol, whereas the higher molecular weight polyubiquitinated species specifically enriched in the membrane fraction (**Fig 3.6E-F**). Taken together, these data are consistent with a model in which SidC/SdcA mediated monoubiquitination is a prerequisite for Rab5 polyubiquitination by the SidE family of effectors, which in turn anchors the small GTPase to the LCV membrane (**Fig 3.6G**).
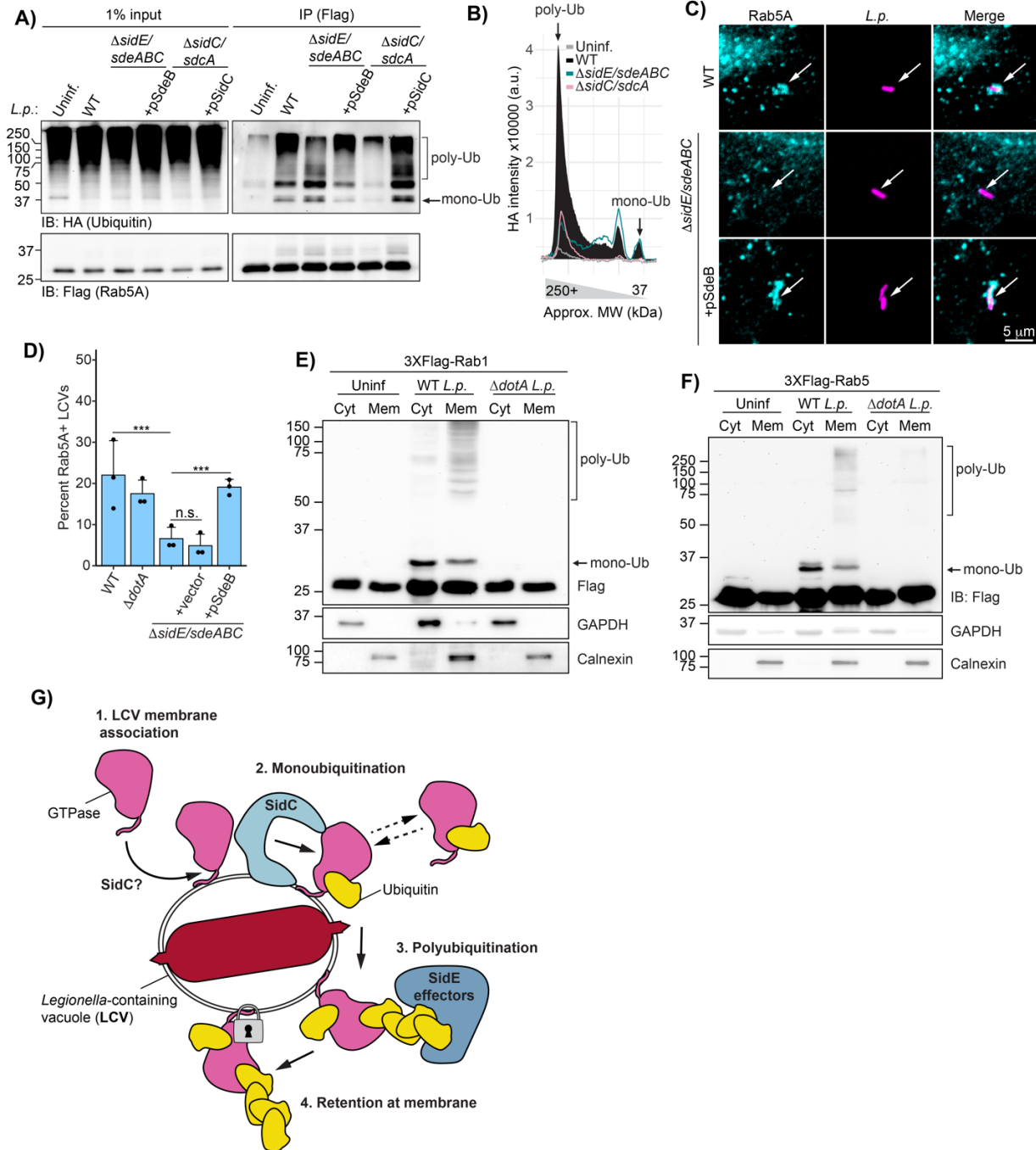
Figure 3.6: SidE family mediated polyubiquitination is downstream of monoubiquitination and anchors Rabs to the membrane. (A)(B) Immunoblot analysis of Flag-Rab5A immunoprecipitation from cells infected with SidE family and SidC/SdcA strain panel. HEK293T FcγR cells transfected with 3XFlag Rab5A and HA-ubiquitin were infected with *L.p.* WT, Δ*sidE/sdeABC*, Δ*sidC/sdcA,* and appropriate plasmid complemented strains for 4 hours or left uninfected. After Flag pulldown, input and IP samples were probed with anti-HA and anti-Flag antibodies. (**B**) Plot profiles of HA signal shown in IP panel in (A) for uninfected and *L.p.* WT, Δ*sidE/sdeABC*, and Δ*sidC/sdcA* infected samples. *Figure caption continued on the next page.*

94

Figure caption continued from the previous page. (**C**) Representative images of Rab5A LCV recruitment levels for the Δ*sidE/sdeABC* strain panel as observed by immunofluorescence. HeLa FcγR cells were infected with indicated strain for 1 hour, fixed, and probed with anti-*Legionella* and anti-Rab5A antibodies. (**E**) Quantification of biological replicates (N=3) of experiment shown in (D). 60-120 LCVs were scored per replicate as positive or negative for Rab5A recruitment, and the percent Rab5A+ LCVs was calculated per replicate. (**E**) and (**F**) immunoblot analysis of cellular fractionations performed on HEK293T FcγR cells transiently expressing the indicated Flag-tagged Rab and infected with *L.p.* WT or Δ*dotA*, or left uninfected. Cells were infected for 1 (E) or 4 (F) hours. (**G**) Schematic working model of small GTPase mono- and poly-ubiquitination. *Statistical analysis of LCV scoring quantification:* G test of independence was performed on pooled counts (positive vs. negative) from all biological replicates. Upon verifying significance ($p < 0.05$), pairwise comparisons between strains were evaluated by post-hoc G-test using the Bonferroni-adjusted p-value as a significance threshold ($p = 0.005$). * = $p < 0.005$, ** = $p < 0.0005$, *** = $p < 0.00005$, n.s. = $p > 0.005$.

3.4   Discussion

Here, we define the ubiquitinated proteome of HEK293 cells infected with *Legionella pneumophila* at 1- and 8-hours post infection. Analysis of this dataset reveals that infection with WT *L.p.* induces hundreds of significant changes in the host ubiquitinome spanning processes known to be involved in infection, such as membrane trafficking and lipid exchange, as well as processes with less characterized or unknown roles in infection, such as mRNA splicing and solute transport. The most dramatic changes in the host ubiquitinome occur at early timepoints during infection, although substantial modification of the ubiquitinome persists at 8hpi. Additionally, we see that many of the same pathways and proteins are targeted throughout infection, suggesting that similar E3 ligases and DUBs may be active throughout infection, or that many early changes in the ubiquitinome are stable. Given the connection between ubiquitination and protein degradation, we also paired our analysis of the host ubiquitinome with an analysis of changes in host protein abundance. Intriguingly, changes in ubiquitination seem to be largely independent of changes in abundance, suggesting that many of the ubiquitination changes we detected during infection are not connected to degradative signaling outcomes.

A major effect of infection was the ubiquitination of 63 of approximately 163 known small GTPases spanning RAB, RAS, RHO/RAC, RAN, and ARF/SAR subfamilies. We determined that many GTPases are monoubiquitinated during infection, and some are polyubiquitinated. Along with our proteomic data showing no significant small GTPase abundance changes during infection, as well as past work demonstrating that ubiquitinated Rab1 is not degraded in the proteasome (Horenkamp et al., 2014), these results strongly suggest that small GTPase ubiquitination plays a non-degradative role during infection. The cross-family ubiquitination of small GTPases also appears to be specific to *L.p.* infection, as human cells infected with *Salmonella* Typhimurium or *Mycobacterium tuberculosis* do not show a comparable level of cross-family ubiquitination (Budzik et al., 2020; Fiskin et al., 2016).

Through sequence alignment and binning of ubiquitinated residues into different structural regions, we were able to determine that most ubiquitination sites fall within GTPase C-terminal regions after the G4 box, including the conserved G5 box SA**K** motif lysine that makes contacts with the guanine of GTP, and the hypervariable C-terminal domain (HVD), which contains sequence elements required for lipidation (Müller and Goody, 2017). Mapping these regions onto the Rab1A structure demonstrated that they form a distinct interface opposite the canonical small GTPase protein binding regions, Switch I and II. This suggests that GTPase ubiquitination during infection functions through an alternative mechanism of action compared to known PTMs within the Switch regions such as phosphorylation and AMPylation, which are known to block GTPase-protein binding interactions more directly (Aktories and Schmidt, 2014; Levin et al., 2016; Müller et al., 2010; Steger et al., 2016; Tan et al., 2011).

Although several studies have investigated small GTPase ubiquitination within these non-Switch regions outside the context of infection, the data on downstream consequences are mixed and appear to be highly GTPase and/or residue dependent. Monoubiquitination of RhoC, Rab11a,

and KRas on either the G5 SAK motif or the preceding α4 helix appears to be activating (Baker et al., 2013; Kholmanskikh et al., 2022; Lachance et al., 2013; Sasaki et al., 2011), while ubiquitination of Rab5 in the same region appears to impair activity (Shin et al., 2017). Equally paradoxical, ubiquitination of Rab7 in the HVD appears to maintain it in the membrane (Sapmaz et al., 2019), while ubiquitination of H/N/KRas in this region prevents membrane association (Steklov et al., 2018).

We determine that robust recruitment and retention of Rab1 on the LCV promotes its ubiquitination. Infection with either *L.p. ΔdrrA* or the AMPylation mutant *L.p. ΔdrrA* + pDrrA D110,112A, known to have reduced Rab1 recruitment to the LCV, results in a substantial decrease in Rab1 ubiquitination compared to *L.p.* WT. Conversely, Rab10, which is not recruited to the LCV by DrrA, undergoes ubiquitination at WT levels during infection with DrrA deficient strains. This result indicates that Rab1 recruitment is required for its ubiquitination, and that ubiquitination of other small GTPases is not contingent upon DrrA activity or Rab1 LCV association.

Paired with our Rab1 LCV-recruitment model, the observation that all Rab5 isoforms are ubiquitinated during infection led us to the finding that Rab5A is recruited to the WT LCV during infection. Previously published results conflicted on whether Rab5 associates with the WT LCV (Clemens et al., 2000; Hoffmann et al., 2014). In the present study we relied on immunofluorescence analysis of endogenous Rab5 during infection, and found that the WT LCV stains positive for Rab5A at moderate frequencies throughout early infection. Additionally, we link Rab5 ubiquitination to LCV recruitment, and observe ubiquitination of endogenous Rab5 in U937 macrophage-like cells. Notably, previous reports suggest that overexpression of Rab5 antagonizes *L.p.* pathogenesis but does so by decreasing the integrity of the LCV membrane (Anand et al., 2020; Kim and Isberg, 2023), rather than by increasing trafficking of the LCV to the

97

lysosome. Consistent with this finding, we observe that Rab5A overexpression results in a bacterial replication defect without an increase in Lamp1 recruitment to the WT LCV. Taken together, these results are inconsistent with a model by which Rab5 activity simply increases trafficking of the LCV to the lysosome, and instead suggest a nuanced interplay between *L.p.* effectors and Rab5 activity during infection.

Our data place the ubiquitin ligase bacterial effectors SidC and SdcA at the center of cross-family small GTPase ubiquitination, although the specific role that they play is still unclear. We find that SidC/SdcA are required for both Rab5A LCV recruitment and ubiquitination. This result adds Rab5A to the list of GTPases already known to be LCV recruited by SidC/SdcA (Arf1, Rab10), and GTPases whose ubiquitination is known to be controlled by SidC/SdcA (Rab1, Rab10) (Horenkamp et al., 2014; Jeng et al., 2019). Here, we show that the ubiquitination of HRas and RhoA is also dependent upon the activity of SidC/SdcA.

Despite their involvement in the recruitment and ubiquitination of these diverse small GTPases, several lines of evidence suggest that small GTPases may not be a direct target of SidC/SdcA ubiquitin ligase activity. First, ectopic expression of SidC/SdcA does not induce ubiquitination of Rab1 (Horenkamp et al., 2014; Hsu et al., 2014) or Rab5 (this study). Second, in vitro ubiquitination reactions containing purified SidC have not resulted in Rab1A ubiquitination (Hsu et al., 2014). Lastly, protein-protein interaction experiments have failed to detect interaction between SidC/SdcA and Rab1, Arf1, or numerous other proteins involved in LCV formation (Horenkamp et al., 2014). We cannot rule out the possibility that SidC/SdcA may be activated by, or interact in complex with another bacterial or host cell protein during infection in order to directly catalyze cross-family small GTPase ubiquitination.

Intriguingly, we note that SidC and SdcA contribute differentially towards the ubiquitination of various GTPases. We find that SdcA is primarily responsible for Rab1 ubiquitination, SidC is primarily responsible for HRas, and RhoA ubiquitination, and both SidC and SdcA seem to play equivalent roles in promoting Rab5 ubiquitination. This difference in specificity implies that SidC and SdcA may target different membranes or GTPases for recruitment to the LCV, consistent with past work that has found lower conservation in a domain of SidC/SdcA hypothesized to be involved in membrane tethering (Horenkamp et al., 2014).

Our discovery of the involvement of the SidE family of bacterial effectors contribute to high molecular weight polyubiquitination – but not monoubiquitination – of the GTPases Rab1/5, leads us to the conclusion that cross-family small GTPase ubiquitination is at least in part a means to promote the retention of GTPases in the bacterial vacuole membrane. This conclusion is supported by our data demonstrating the role of SidE/SdeA/B/C in the LCV recruitment of Rab5, as well as cellular fractionations showing polyubiquitinated Rab1/5 almost exclusively localizing to membrane fractions. SidE-mediated polyubiquitination appears to occur downstream of initial recruitment and monoubiquitination, as manipulations such as knockout of the Rab1 GEF effector DrrA, deletion of CAAX box residues, and knockout of SidC/SdcA all affect the accumulation of mono- and polyubiquitinated species together. Notably, knockout of SidE/SdeA/B/C does not completely prevent polyubiquitination of Rab5 (Fig 7A), suggesting that other effectors play a role in polyubiquitination. However, the Δ*sidE/sdeABC* strain LCV is largely Rab5-negative, suggesting that non-canonical phosphoribosyl ubiquitination may play a specific role in maintaining Rab5 at the LCV membrane.

We note that here that there are differences in the recruitment and ubiquitination cascades that regulate Rab1 and Rab5: While SidC/SdcA and SidE/SdeA/B/C regulate the mono- and polyubiquitination of Rab1, the role that they play in its LCV localization is unclear, as numerous

effectors, including DrrA, regulate Rab1 recruitment and retention in the LCV membrane (Hardiman and Roy, 2014; Ingmundson et al., 2007; Mukherjee et al., 2011; Neunuebel et al., 2012). Indeed, past work demonstrates that SidC/SdcA play no role in the recruitment of Rab1 to the LCV membrane (Horenkamp et al., 2014). For Rab5, however, the SidC/SdcA-SidE family ubiquitination cascade appears to be primarily responsible for Rab5 recruitment and retention.

Our data lead us to propose a model in which: (1) Initial recruitment of small GTPases to the LCV membrane, which may be mediated by SidC/SdcA, precedes (2) monoubiquitination, for which SidC/SdcA are required, priming these LCV-localized small GTPases for (3) SidE-mediated polyubiquitination, that leads to (4) their retention in the membrane (**Fig 3.6G**). This work suggests a complex interplay between SidC/SdcA and the SidE effector family in the ubiquitination and LCV retention of small GTPases during infection, and more broadly implies a collaboration between these two effector groups in modulating ubiquitin signaling during infection. Our findings position *L.p.* as a tool to understand a small GTPase regulation in both infected and uninfected contexts. Further examination of the host and bacterial proteins required for cross-family small GTPase ubiquitination is warranted, as the mechanistic details of this phenomenon will provide insight into both eukaryotic regulation of small GTPase activity and bacterial strategies of host cell manipulation.

3.5 Materials and methods

3.5.1 Cell lines

HEK293T cells (female), HEK293 cells (female) stably expressing the Fcγ receptor IIb (HEK293 FcγR cells), and HeLa FcγR cells were cultured in Dulbecco's Modified Eagle's Medium (DMEM, GIBCO) containing 10% fetal bovine serum (FBS, VWR) at 37°C and 5% CO_2. FcγR expressing cell lines were gifts from the lab of Dr. Craig Roy at Yale University. U937 cells (a gift from Dr.

Michael Bassik at Stanford University) were cultured in RPMI-1640 (Corning) supplemented with 10% heat-inactivated FBS (VWR). U937 were differentiated into macrophage-like cells in 20 ng/mL phorbol 12-myristate 13-acetate (PMA, Sigma) for 72 hours, then re-plated in media without PMA and allowed to rest for 48 hours before *L.p* infection.

3.5.2   Bacterial strains and plasmids

Experiments were performed with *Legionella pneumophila* serogroup 1, strain Lp01 or Lp02. Avirulent T4SS-null strains were derived as previously described (Berger et al., 1994; Berger and Isberg, 1993). *L. pneumophila* strains were grown on Charcoal Yeast Extract (CYE) agar plates or AYE broth supplemented with (FeNO$_3$ 0.135g/10mL) and cysteine (0.4g/10mL). Growth media for Lp02 thymidine auxotroph-derived strains was supplemented with 100 ug/mL thymidine. For strains carrying complementation plasmids, chloramphenicol (5 µg/mL) was supplemented for plasmid maintenance, and IPTG (1 mM) was added for 2 hours of induction prior to infection. The unmarked gene deletion Δ*sidC-sdcA* and Δ*drrA* strains were derived from the parental strain using allelic exchange as described previously (Berger et al., 1994). Rab5A, Rab5B, and Rab5C coding sequences were amplified from HeLa cDNA and cloned into a pcDNA3.1 mammalian expression vector containing the appropriate N-terminal tag (3XFlag or mCherry). Rab5A, Rab1A, and Rab10 CAAX deletion inserts were derived from appropriate full-length plasmid by PCR amplification of the desired region.

3.5.3   Infection of cultured mammalian cells with L.p.

Infections with *L.p.* were performed as previously described (Treacy-Abarca and Mukherjee, 2015). *L.p.* heavy patches grown for 48 h on CYE plates were either used directly for infection, or for overnight liquid cultures in AYE medium until reaching an OD600 of 3. *L.p.* from the overnight culture was enumerated and the appropriate amount was opsonized with *L.p.*-specific antibodies at a dilution of 1:2000 in cell growth medium for 20 min. HEK293 FcγR were grown on poly-lysine coated cell culture plates to a confluency of 80% and infected with the *L.p.* WT strain or the isogenic Δ*dotA* mutant strain at a multiplicity of infection (MOI) of 1-100 as indicated. The infection

was synchronized by centrifugation of the plates at 1000xg for 5 min. To prevent internalization of any remaining extracellular bacteria at later timepoints, cells were washed three times with warm PBS after 1 h of infection and fresh growth medium was added. Cells were collected for down-stream processing at the indicated timepoints. Uninfected samples used as controls for infection experiments were mock-infected using media and opsonization antibody only.

3.5.4 Sample preparation for proteomics analysis

HEK293 FcγR infected for 1 h or 8 h with the *L.p.* WT strain Lp01 or the isogenic *ΔdotA* mutant were infected at an MOI of 100. Uninfected HEK293 FcγR cells were included as a control. Cells were washed with ice-cold PBS, collected and the pellet was frozen at -80°C. Cell pellets were lysed by probe sonication in three pulses of 20% amplitude for 15 s in a lysis buffer consisting of: 8 M urea, 150 mM NaCl, 100 mM ammonium bicarbonate, pH 8; added per 10 ml of buffer: 1 tablet of Roche mini-complete protease inhibitor EDTA free and 1 tablet of Roche PhosSTOP. In order to remove insoluble precipitate, lysates were centrifuged at 16,100 g at 4°C for 30 min. A Bradford Assay (Thermo) was performed to measure protein concentration in cell lysate supernatants. 6 mg of each clarified lysate was reduced with 4 mM tris(2-carboxyethyl)phosphine for 30 min at room temperature and alkylated with 10 mM iodoacetamide for 30 min at room temperature in the dark. Remaining alkylated agent was quenched with 10 mM 1,4-dithiothreitol for 30 min at room temperature in the dark. The samples were diluted with three starting volumes of 100 mM ammonium bicarbonate, pH 8.0, to reduce the urea concentration to 2 M. Samples were incubated with 50 µg of sequencing grade modified trypsin (Promega) and incubated at room temperature with rotation for 18 hr. The sample pH was reduced to approximately 2.0 by the addition of 10% trifluoroacetic acid (TFA) to a final concentration of 0.3% trifluoroacetic acid. Insoluble material was removed by centrifugation at 16,000 g for 10 min. Peptides were desalted using SepPak C18 solid-phase extraction cartridges (Waters). The columns were activated with 1 ml of 80% acetonitrile (I), 0.1% TFA, and equilibrated 3 times with 1 ml of 0.1% TFA. Peptide samples were applied to the columns, and the columns were washed 3 times with 1 ml of 0.1%

TFA. Peptides were eluted with 1.2 ml of 50% I, 0.25% formic acid. Peptides were divided for global protein analysis (10 µg) or diGly-enrichment (remaining sample), and lyophilized.

3.5.5   *diGlycine peptide enrichment by immunoprecipitation*

Peptide samples were subjected to ubiquitin remnant immunoaffinity. 10 uL of PTMScan® Ubiquitin Remnant Motif (K-ε-GG) Antibody Bead Conjugate purification (Cell Signaling) slurry was used per 1 mg peptide sample. Ubiquitin remnant beads were washed twice with IAP buffer, then split into individual 1.7 mL low bind tubes (Eppendorf) for binding with peptides. Peptides were dried with a centrifugal evaporator for 12 hours to remove TFA in the elution. The lyophilized peptides were resuspended in 1 ml of IAP buffer (50 mM 4- morpholinepropnesulfonic acid, 10 mM disodium hydrogen phosphate, 50 mM sodium chloride, pH 7.5). Peptides were sonicated and centrifuged for 5 minutes at 16,100g. The soluble peptide supernatant was incubated with the beads at 4˚C for 90 minutes with rotation. Unbound peptides were separated from the beads after centrifugation at 700g for 60 seconds. Beads containing peptides with di-glycine remnants were washed twice with 500 µL of IAP buffer, then washed twice with 500 µL of water, with a 700g 60s centrifugation to allow the collection of each wash step. Peptides were eluted twice with 60 µL of 0.15% TFA. Di-glycine remnant peptides were desalted with UltraMicroSpin C18 column (The Nest Group). Desalted peptides were dried with a centrifugal adaptor and stored at -20˚C until analysis by liquid chromatograph and mass spectrometry.

3.5.6   *Mass spectrometry data acquisition and processing*

Samples were resuspended in 4% formic acid, 4% acetonitrile solution, separated by a reversed-phase gradient over a nanoflow column (360 µm O.D. x 75 µm I.D.) packed with 25 cm of 1.8 µm Reprosil C18 particles with (Dr. Maisch), and directly injected into an Orbitrap Fusion Lumos Tribrid Mass Spectrometer (Thermo). Total acquisition times were 120 min for protein abundance, 100 min for phosphorylation, and 70 min for ubiquitylation analyses. Specific data acquisition settings are detailed in **Supplemental File 3**. Raw MS data were searched with MaxQuant against both the human proteome (UniProt canonical protein sequences downloaded January 11,

2016) and the *Legionella Pneumophila Philadelphia* proteome (downloaded July 17, 2017). Peptides, proteins, and PTMs were filtered to 1% false discovery rate in MaxQuant (Cox et al., 2014). Principal Component analysis of normalized MS Intensities of experimental conditions (control, Δ*dotA*-1h, Δ*dotA*-8h, WT-1h, WT-8h) was performed using the factoextra R package as implemented by the artMS bioconductor package. The plot illustrates the relationship between the variables (conditions) and the principal components, where each variable is represented as a vector, and the direction and length of the vectors indicate how each variable contributes to the two principal components. If two vectors are close together indicates a strong positive correlation between those two variables, i.e. they contribute to the principal components in a similar way. Statistical analysis of quantifications obtained from MaxQuant was performed with the artMS Bioconductor package (version 0.9) (Jimenez-Morales et al., 2019). Each dataset (proteome and ubiquitinome) was analyzed independently. Quality control plots were generated using the artMS quality control functions. The site-specific relative quantification of posttranslational modifications required a preliminary step consisting of providing the ptm-site/peptide-specific annotation ("artmsProtein2SiteConversion()" function). artMS performs the relative quantification using the MSstats Bioconductor package (version 3.14.1) (Choi et al., 2014). Contaminants and decoy hits were removed. Samples were normalized across fractions by median-centering the Log_2-transformed MS1 intensity distributions (**Sup Fig 3.1-1B, Sup Fig 3.1-3B**). **Imputation strategy:** Log2FC for protein/sites with missing values in one condition but found in ≥ 2 biological replicates of the other condition of any given comparison were estimated by imputing intensity values from the lowest observed MS1-intensity across sample peptides (Webb-Robertson et al., 2015); p-values were randomly assigned between 0.05 and 0.01 for illustration purposes.

3.5.7 *Subcellular compartment analysis, functional enrichment analysis, and small GTPase sequence alignment*

Statistically significant changes were selected by applying the joint thresholds of |Log2FC| ≥ 1, adj.-p-value < 0.05. Imputed values were also considered significant and are indicated in figures

separately from non-imputed values. WT1hr-Control, WT8hr-Control, Δ*dotA*1hr-Control, and Δ*dotA*8hr-Control comparisons were filtered using these significance criteria for subsequent analyses. Subcellular compartment analysis was performed by tabulating the number of significantly regulated proteins per compartment based on subcellular localization identifiers from UniProt. Biological pathway and protein complex enrichment was performed using Metascape (Zhou et al., 2019) (https://metascape.org). The following ontology sources were used for analysis: GO Biological Processes, KEGG Pathway, GO Molecular Functions, GO Cellular Components, Reactome Gene Sets, Hallmark Gene Sets, Canonical Pathways, BioCarta Gene Sets, CORUM, WikiPathways and PANTHER Pathway. Significant enrichment terms were selected using the combined thresholds of p-value < 0.01, a minimum count of 3 proteins, and an enrichment factor > 1.5. Proportional Venn diagrams were created using DeepVenn (Hulsen, 2022) and recolored in Adobe Illustrator. Proteins within the Ras superfamily were defined based on the "Ras small GTPase superfamily" definition in the HUGO Gene Nomenclature Committee database (https://www.genenames.org/, HGNC group ID = 358). Sequence alignment was performed using Jalview (Waterhouse et al., 2009).

3.5.8   *Cell lysis, immunoprecipitation, and immunoblot analysis*

HEK293 FcγR cells grown on poly-lysine coated plates were treated as indicated, washed three times with ice-cold PBS and harvested with a cell scraper. Cells were pelleted at 3000xg for 10 minutes at 4C. For preparation of whole cell lysates, cell pellets were resuspended in RIPA buffer supplemented with cOmplete Protease Inhibitor Cocktail (Roche), phenymethylsulphonyl fluoride (PMSF, 1 mM), and 10 mM NEM and lysed under constant agitation for 20 min at 4°C. Cell debris was removed by centrifugation at 16,000xg for 20 min at 4°C. Protein concentration was measured using the Pierce 660nm Protein Assay Kit or the Pierce™ BCA Protein Assay Kit (Thermo Fisher Scientific). For each sample, 20-30 µg of proteins were denatured in SDS sample buffer/5% β-mercaptoethanol at 95°C for 5 min. For Flag pulldown assays, cells were lysed in 137

mM NaCl, 20 mM Tris base pH 8, 1% v/v NP40, 2 mM EDTA supplemented with inhibitors as above. Protein concentrations were measured as above, and lysates were diluted to equal volumes at equal concentrations (1-3 mg/mL). Input samples were removed and prepared for SDS-PAGE as above. Anti-Flag M2 antibody was added at a 1:50 dilution to the remaining lysate and rotated overnight at 4C. Samples were incubated with rotation with Protein G Dynabeads (1.5 mg/sample) for 2 hours at 4C. Beads were washed three times with ice cold lysis buffer, and bound proteins were eluted in 30 uL 2X SDS sample buffer for 10 minutes at 95C. For ubiquitin pulldown assays using the SignalSeeker kit (Cytoskeleton Inc), cells were lysed in provided BlastR buffer with protease inhibitor and NEM, and total protein concentration measured using Precision Red Advanced protein assay. Lysates were diluted to 1 mg/mL, and 1 mL of diluted lysate was incubated with either unconjugated (control) or ubiquitin binding domain conjugated beads for 2 hours at 4C on a rotating platform. Beads were washed three times in wash buffer, and bound proteins were eluted using kit spin columns. For immunoblot analysis, samples were loaded on 8-12% SDS-polyacrylamide gels and separated by SDS-PAGE. Proteins were transferred to PVDF membranes (0.45 µm, Millipore) at 30 V, 4°C for 16 h. For total ubiquitin blots (**Fig 3.1D**), total protein was quantified before blocking using Invitrogen No-Stain Protein Labeling Reagent. Membranes were washed with PBS-T (PBS/ 0.1% Tween-20 (Thermo Fisher Scientific)), blocked with 5% Blotting Grade Blocker Non Fat Dry Milk (Bio-Rad) for 1 h at room temperature and incubated with the primary antibodies diluted in blocking buffer/0.02% (w/v) sodium azide overnight at 4°C. Membranes were washed three times with PBS-T and incubated with Goat Anti-Mouse IgG (H+L) HRP Conjugate (Thermo Fisher Scientific), Goat Anti-Rabbit IgG (H+L) (Thermo Fisher Scientific), HRP Conjugate, diluted at 1:5000 in blocking buffer for 60 min at room temperature. After three washes with PBS-T, membranes were incubated with Amersham ECL Western Blotting Detection Reagent (Global Life Science Solutions) for 1 min and imaged on a ChemiDoc Imaging System (BioRad).

3.5.9   Cellular fractionation

After indicated treatment, cells were collected by gentle scraping into the culture medium and pelleted at 200xg for 5 minutes at 4C. Cells were washed in ice cold 1X PBS, then gently homogenized in ice cold homogenization buffer (150 mM KCl, 20 mM HEPES pH 7.4, 2 mM EDTA, 1X cOmplete Protease Inhibitor Cocktail). Cells were lysed with 20-30 passes through a 25g needle. Lysates were spun at 0.6xg, 4C for 5 minutes to remove nuclei and unlysed cells. Post-nuclear supernatant was spun at 150,000xg for 45 minutes, and the supernatant transferred to a new tube (cytosolic fraction). The membrane pellet was washed once in homogenization buffer and re-pelleted at 150,000xg, 4C for 20 minutes. The supernatant was removed, and the membrane pellet resuspended in homogenization buffer + 1% v/v Triton-X 100.

3.5.10 Immunoblot quantification

Images were exported from ImageLab (BioRad) as 16-bit tiff and analyzed in ImageJ. Plot profiles were generated for each lane and the integrated density was calculated using the ImageJ built in gel analyzer tools. Total ubiquitin signal was normalized to total protein, and the fold change was calculated compared to the appropriate uninfected control. To calculate normalized Rab monoubiquitination intensity, integrated density was measured for the unmodified band at sub-saturated exposure. Integrated density was measured for the higher molecular weight monoubiquitination band at the lowest exposure in which this band was visible. Normalized Rab monoubiquitination was calculated as follows: IntDen monoUb/(IntDen monoUb + InDen unmod Ub). To standardize these values across biological replicates, values are represented as a percentage of the WT infection condition for each replicate. The intensity profiles in Fig 7B were generated in Fiji.

3.5.11 Immunofluorescence, image acquisition, and image analysis

HeLa FcγR cells were grown on poly-lysine coated coverslips in 24well cell culture plates. Cells were treated as indicated, washed three times with PBS and fixed in 4% paraformaldehyde/PBS for 15 min at room temperature. Cells were then treated with 2% BSA, 0.5% saponin in PBS (blocking/permeabilization buffer) for 1h at RT. Cells were stained with primary antibodies diluted

in blocking/permeabilization buffer overnight at 4C, washed three times with PBS and stained with secondary antibodies diluted in blocking/permeabilization buffer for 1h at RT. Cells were then stained with Hoechst33342 at 1:2000 in PBS for 10 min and washed three times with PBS. Coverslips were dipped three times into purified ddH$_2$O to remove salts, dried and mounted on microscopy glass slides with Prolong Diamond antifade 5 (Thermo Fisher Scientific). Slides were cured overnight at room temperature. Images were acquired on a Nikon Ti2 Eclipse inverted microscope outfitted with a CREST X-Light V2 spinning disk unit and Photometrics Prime 95B CMOS camera (binning 1x1, 16-bit). All images were acquired using a 60X 1.4NA oil immersion objective. NIS-Elements software was used to control the microscope and acquire images. Lasers were used at the following intensities: ExW 365nm 25%, ExW 488nm 25%, ExW 561nm 100%, ExW 640nm 100%. Exposure time ranged from 10-50 ms. Images were analyzed in Fiji. Experimental conditions were blinded either before image acquisition, or before image analysis using the Fiji Blind Analysis Tools plugin filename encrypter. For LCV scoring, max intensity Z projections were generated. LCVs were scored positive if the LCV region was visible in the protein marker of interest channel only (i.e. without the *L.p.* marker). All LCV area measurements were carried out in Fiji using the freehand selection tool. Representative images in all figures are max intensity Z projections.

3.5.12 Cell transfections

All transfections were performed with jetPRIME (Polyplus). HEK293 FcγR or HeLa FcγR cells were grown to 60% confluency and transfected according to the manufacturer's recommendations. For transfection of plasmid DNA, 0.25 µg DNA was used for 24well plates, 1-2 µg DNA for 6 well plates, 2-3 ug for 60 mm plates, and 5-10 ug for 100 mm plates. 24h after transfection, cells were treated as indicated and analyzed or harvested. For experiments in which HA-ubiquitin was transiently co-expressed, the expression construct was added at 20% of the total amount of DNA to minimize pleiotropic effects of strong ubiquitin overexpression.

3.5.13 Data availability

The mass spectrometry data files have been deposited to the ProteomeXchange Consortium (http://proteomecentral.proteomexchange.org) via the PRIDE partner repository with the dataset identifier PXD019217 (Vizcaíno et al., 2016).

3.5.14 Key resources table

Cell lines		
Cell Line	**ID**	**Source**
Human: HEK293 cells stably expressing FcγRIIb	derived from ATCC CRL-1573	Gift from Dr. Craig Roy
Human: HEK293T cells stably expressing FcγRIIb	derived from ATCC CRL-3216	This study
Human: HeLa cells stably expressing FcγRIIb	derived from ATCC CCL-2	Gift from Dr. Craig Roy
Human: U937	ATCC CRL-1593.2	Gift from Dr. Michael Bassik
Bacterial Strains		
Strain	**ID**	**Source**
Legionella pneumophila serogroup 1 strain Lp01	LEG001	(Berger et al., 1994), Gift from Dr. Craig Roy
Lp01 Δ*dotA*	LEG002	(Berger et al., 1994), Gift from Dr. Craig Roy
Lp01 Δ*drrA*	LEG005	Gift from Dr. Craig Roy
Lp01 Δ*drrA* pJB1806	LEG169	This study
Lp01 Δ*drrA* pJB1806::DrrA	LEG045	This study
Lp01 Δ*drrA* pJB1806::DrrA D110, 112A	LEG046	This study
Lp01 Δ*sidC/sdcA* (Δ*lpg2510-2511)*	LEG073	Gift from Dr. Craig Roy
Lp01 Δ*sidC/sdcA* pJB1806	LEG184	This study
Lp01 Δ*sidC/sdcA* pJB1806::SdcA	LEG081	This study
Lp01 Δ*sidC/sdcA* pJB1806::SidC	LEG082	This study
Legionella pneumophila serogroup 1 strain Lp02 *rpsL hsdR thyA*	LEG003	(Berger and Isberg, 1993), Gift from Dr. Craig Roy

Strain	ID	Source
Lp02 Δ*dotA* (LP03)	LEG004	(Berger and Isberg, 1993),Gift from Dr. Craig Roy
Lp02 Δ*sidC/sdcA* (Δ*lpg2510-2511*)	LEG173	This study
Lp02 Δ*sidC/sdcA* pJB1806	LEG179	This study
Lp02 Δ*sidC/sdcA* pJB1806::SdcA	LEG180	This study
Lp02 Δ*sidC/sdcA* pJB1806::SidC	LEG181	This study
Lp02 Δ*sidE* Δ*sdeC* Δ*sdeBA* (Δl*pg0234*, Δl*pg2153* Δl*pg2156-2157*), annotated as "Δ*sidE/sdeABC*" for brevity	LEG151	(Jeong et al., 2015), Gift from Dr. Ralph Isberg
Lp02 Δ*sidE* Δ*sdeC* Δ*sdeBA* pJB1806	LEG170	This study
Lp02 Δ*sidE* Δ*sdeC* Δ*sdeBA* pJB1806::SdeB	LEG171	This study
Recombinant DNA		
Vector	**ID**	**Source**
pEGFP-N1 Arf1-GFP	pSM114	Gift from Dr. Craig Roy
pEGFP-N1 Arf6-GFP	pSM115	Gift from Dr. Craig Roy
pCDNA3.1 3XFlag-Rab1 WT	pSM178	This study
pCDNA3.1 3XFlag-Rab1 ΔCAAX	pSM183	This study
pcDNA3.1 EGFP-Rab1 WT	pSM234	This study
pcDNA3.1 EGFP-Rab1 ΔCAAX	pSM236	This study
pCDNA3.1 3XFlag-Rab10 WT	pSM184	This study
pCDNA3.1 3XFlag-Rab10 ΔCAAX	pSM186	This study
pEGFP-C1 GFP-Rab6A	RC45	Gift from Dr. Craig Roy
pEGFP-C1 GFP-Rab9A	RC57	Gift from Dr. Craig Roy
pEGFP-C1 GFP-Rab19	RC66	Gift from Dr. Craig Roy

Vector	ID	Source
pEGFP-C1 GFP-Rab20	RC69	Gift from Dr. Craig Roy
pEGFP-C1 GFP-Rab35	RC77	Gift from Dr. Craig Roy
pXFP mCerulean3-Rap1	pSM259	Addgene #134928
pEGFP-C1 GFP-Rap2B	pSM258	Addgene #118321
pCl mEGFP-HRas	pSM253	Addgene #18662
pEGFP-C3 GFP-RhoA	pSM254	Addgene #23224
pEGFP-C2 GFP-RhoB	pSM255	Addgene #23225
pEGFP-C2 GFP-RhoC	pSM256	Addgene #23226
pEGFP-C GFP-RhoQ	pSM257	Addgene #23232
pcDNA3.1 mCherry-Rab5A	pAS042	This study
pcDNA3.1 mCherry-Rab5A ΔCAAX	pAS049	This study
pcDNA3.1 3XFlag-Rab5A	pAS034	This study
pcDNA3.1 3XFlag-Rab5A ΔCAAX	pAS041	This study
pcDNA3.1 3XFlag-Rab5B	pAS050	This study
pcDNA3.1 3XFlag-Rab5C	pAS051	This study
pEGFP-C2	pSM150	Gift from Dr. Craig Roy
pEGFP-C2 GFP-SdcA	pSM261	Gift from Dr. Craig Roy
pEGFP-C2 GFP-SidC	pSM174	Gift from Dr. Craig Roy
pRK5-HA Ubiquitin	pSM099	Gift from Dr. Kohei Arasaki
Antibodies		
Antigen	**Dilution (application)**	**Source**
Rab5A	1:1000 (WB), 1:200 (IF)	Cell Signaling Technology (46449)
EEA1	1:100 (IF)	Abcam (ab70521)
Lamp1	1:200 (IF)	Cell Signaling Technology (15665)
Flag	1:2500 (WB), 1:50 (IP)	Sigma (F1804)
Flag (HRP conjugate)	1:2500 (WB)	Sigma (A8592)
Hsp70	1:2000 (WB)	Santa Cruz (sc-66048)
GFP	1:1000 (WB)	Roche (11814460001)
Ubiquitin	1:1000 (WB)	Cell Signaling Technology (3933S)

Antigen	Dilution (application)	Source
HA (HRP conjugate)	1:1000 (WB)	Thermo (26183-HRP)
L. pneumophila	1:2000 (opsonization)	Thermo (PA1-7227)
Goat anti-Rabbit IgG (H+L) Highly Cross-Adsorbed Secondary Antibody (Alexa Fluor 633)	1:500 (IF)	Life Technologies (a21071)
Goat anti-Mouse IgG (H+L) Highly Cross-Adsorbed Secondary Antibody (Alexa Fluor 488)	1:500 (IF)	Life Technologies (a11029)
Goat Anti-Mouse IgG (H+L) HRP Conjugate	1:5000 (WB)	Life Technologies (A16066)
Goat Anti-Rabbit IgG (H+L) HRP Conjugate	1:5000 (WB)	Life Technologies (A16096)
Mouse Anti rabbit IgG (Conformation Specific) - HRP conjugate	1:2000 (WB) - used for ubiquitin immunoblots to avoid detection of opsonization antibody	Cell Signaling Technology (5127S)
Kits		
Signal-Seeker™ Ubiquitination Detection Kit	Cytoskeleton, Inc.	Cat.# BK161
Software and algorithms		
Name	**Source**	**Link**
MaxQuant	(Cox et al., 2014)	https://www.maxquant.org
artMS Bioconductor package (v 0.9)	(Jimenez-Morales et al., 2019)	https://bioconductor.org/packages/release/bioc/html/artMS.html
factoextra R package	(Jimenez-Morales et al., 2023)	https://zenodo.org/record/8093247
Metascape	(Zhou et al., 2019)	https://metascape.org
DeepVenn	(Hulsen, 2022)	https://www.deepvenn.com
Jalview	(Waterhouse et al., 2009)	https://www.jalview.org
Fiji	(Schindelin et al., 2012)	https://fiji.sc
Prism	Graphpad	https://www.graphpad.com
ggplot2 (R package for generating plots)		https://ggplot2.tidyverse.org
UCSF ChimeraX	(Pettersen et al., 2021)	https://www.cgl.ucsf.edu/chimerax/

Deposited data		
Raw data from mass spectrometry	ProteomeXchange Consortium (http://proteomecentral.proteomexchange.org) via PRIDE partner repository	PXD019217

3.5.15 Author contributionsttgf

Conceptualization, S.M., V.B., A.S., D.J-M., D.L.S., and N.J.K.; Methodology, S.M., E.S., G.M.J., D.J-M., D.L.S., and N.J.K.; Data Curation, A.S., V.B., D.J-M., D.L.S.; Validation, A.S., V.B.; Formal Analysis, A.S., V.B., D.J-M.; Investigation, V.B., A.S.; Writing, V.B., A.S., S.M., D.L.S., and D.J-M.; Visualization, A.S., V.B., D.J.-M.; Funding Acquisition, S.M., D.L.S., and N.J.K.; Resources, S.M., D.L.S., and N.J.K.; Supervision, S.M., D.L.S., and N.J.K..

3.5.16 Competing interests

The N.J.K. laboratory has received research support from Vir Biotechnology, F. Hoffmann-La Roche and Rezo Therapeutics. N.J.K. has previously held financially compensated consulting agreements with the Icahn School of Medicine at Mount Sinai, New York and Twist Bioscience Corp. He currently has financially compensated consulting agreements with Maze Therapeutics, and Interline Therapeutics, Rezo Therapeutics, and GEn1E Lifesciences, Inc.. He is on the Board of Directors of Rezo Therapeutics and is a shareholder of Tenaya Therapeutics, Maze Therapeutics, Rezo Therapeutics and Interline Therapeutics. D.L.S. has a consulting agreement with Maze Therapeutics. All other authors declare no competing interests.

3.5.17 Acknowledgements

We thank Dr. Julia Noack for her preparation of the schematic in Figure 1A and for her support with initial analysis of the mass spectrometry data. We thank Dr. Philipp Schlaermann for preparation of cell pellets for the proteomics experiment. We thank Dr. Advait Subramanian and Dr. Joe Henry Steinbach for critically reading the manuscript. V.B. acknowledges support from

3.6 Supplementary Figures

A)

B)

C)

Dataset	Sample	# bioreplica	# bioreplica	n (# peptides)	r (correlation coefficient)
UB	Control	1	2	3000	0.8
UB	Control	1	3	3000	0.85
UB	Control	2	3	3000	0.88
UB	WT1h	1	2	4034	0.91
UB	WT1h	1	3	4034	0.88
UB	WT1h	2	3	4034	0.88
UB	WT8h	1	2	3527	0.9
UB	WT8h	1	3	3527	0.89
UB	WT8h	2	3	3527	0.91
UB	dotA1h	1	2	2728	0.89
UB	dotA1h	1	3	2728	0.87
UB	dotA1h	2	3	2728	0.86
UB	dotA8h	1	2	3241	0.87
UB	dotA8h	1	3	3241	0.9
UB	dotA8h	2	3	3241	0.88

D)
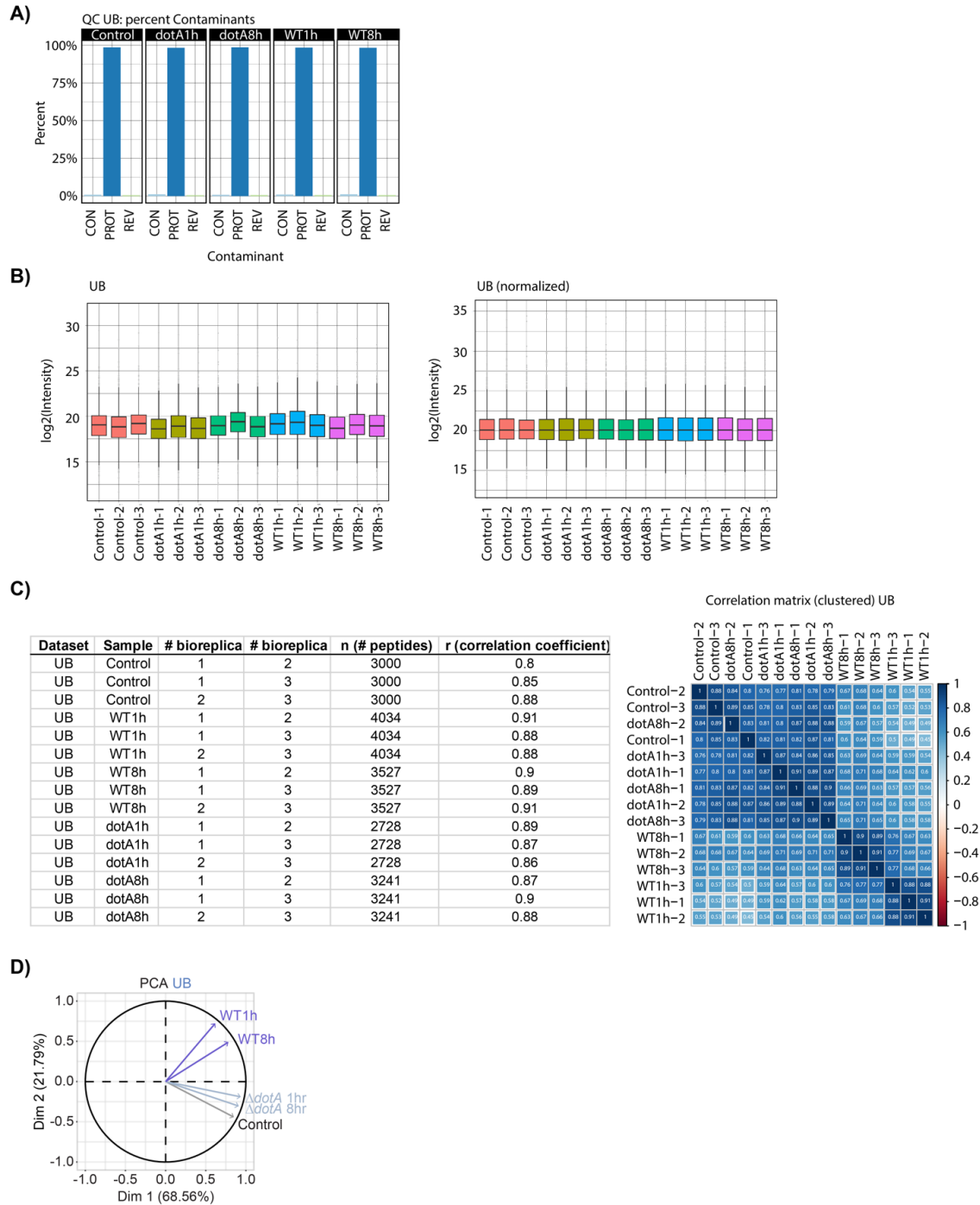
Supplementary Figure 3.1-1: Quantification and quality control plots of ubiquitinomics data. Related to Figure 3.1. Quality control plots for diGly enriched dataset were generated using the artMS Bioconductor package (version 0.9) (Jimenez-Morales et al., 2019). **(A)** Percent of contaminants (CON), proteins (PROT) and reversed sequences (REV) in each experimental condition (control, dotA-1h, dotA-8h, WT-1h, WT-8h) were quantified to adjust the false-discovery-rate (FDR). *Figure caption continued on the next page.*

Figure caption continued from the previous page. **(B)** Samples were normalized across fractions by median-centering the Log2-transformed MS1 intensity distributions. **(C)** Correlation table and matrix showing the clustering of the different experimental conditions. **(D)** Principal Component analysis of normalized MS Intensities of experimental conditions (control, ΔdotA-1h, ΔdotA-8h, WT-1h, WT-8h). PC1 and PC2 captured most of the variability. Loading variables are represented as vectors. The smaller angle between control and the mutant time points (Δ*dotA*-1h, Δ*dotA*-8h) implies a larger positive correlation between them, as opposed to a lower correlation (larger angle) between the Control and the WT strain.
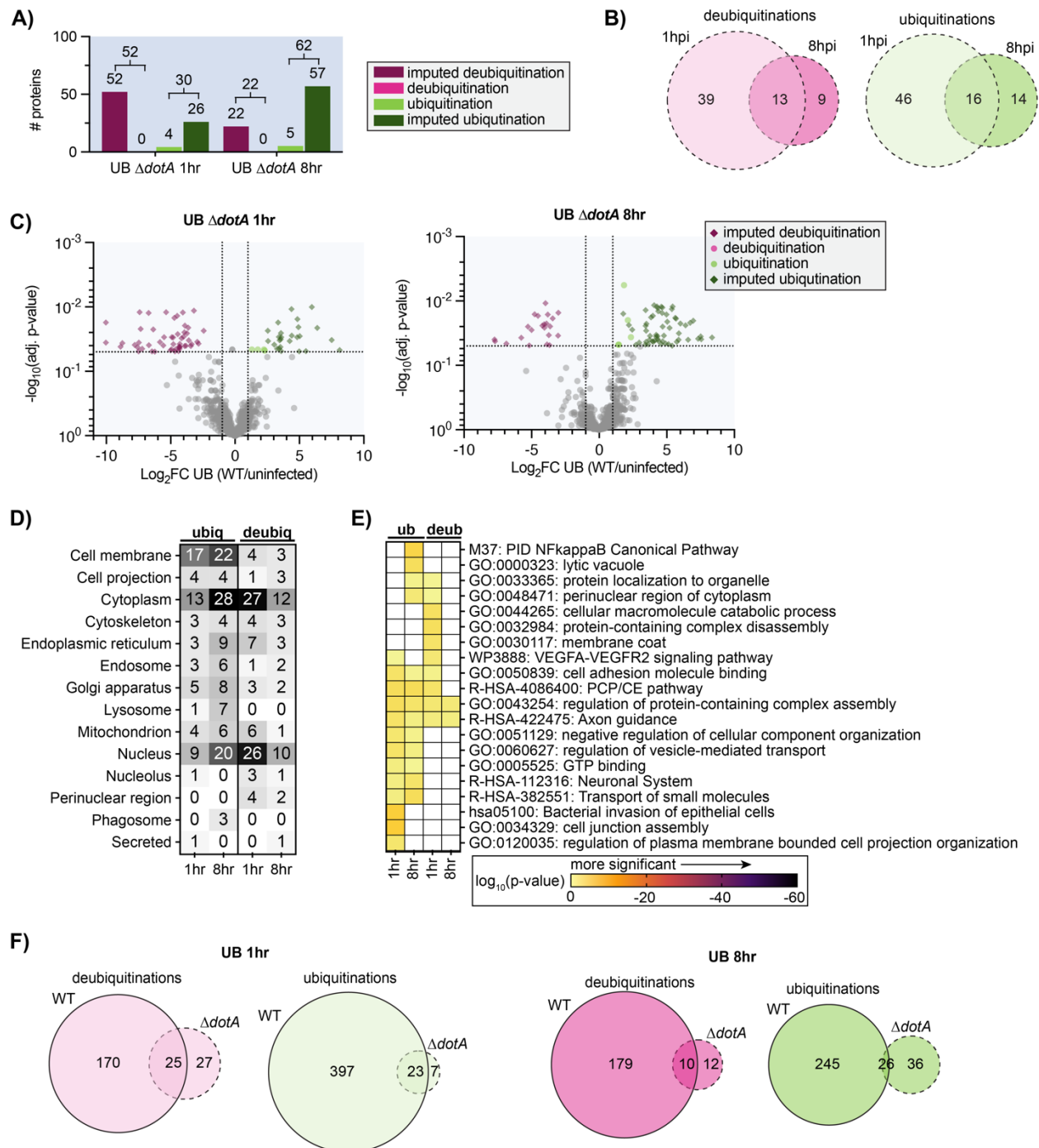
Supplementary Figure 3.1-2: Analysis of T4SS-independent (*L.p. ΔdotA*) changes in the host cell ubiquitinome. Related to Figure 3.1. (A) Counts of proteins with a significant increase (green) or decrease (magenta) in ubiquitination compared to uninfected control for Δ*dotA* 1hr and Δ*dotA* 8hr (same data shown in Figure 1B, repeated here for clarity). **(B)** Overlap of proteins with a significant increase (green) or decrease (magenta) in ubiquitination compared to uninfected control in the 1-hour vs 8-hour *L.p.* Δ*dotA* infected conditions. **(C)** Volcano plot representation of all ubiquitinome data in Δ*dotA* vs uninfected comparison at 1- and 8-hours post-infection. Imputed values are shown as diamonds. Significance threshold is indicated by the dotted line. *Figure caption continued on the next page.*

117

Figure caption continued from the previous page. **(D)** Subcellular localization analysis of proteins with a significant increase or decrease in ubiquitination compared to uninfected control during *L.p.* Δ*dotA* infection for 1 or 8 hours. **(E)** Metascape pathway and protein complex analysis of proteins with a significant increase or decrease in ubiquitination compared to uninfected control during *L.p.* Δ*dotA* infection for 1 or 8 hours. Terms not significantly enriched for a given experimental condition are represented by white boxes. **(F)** Overlap of proteins with a significant increase (green) or decrease (magenta) in ubiquitination compared to uninfected control in the WT *L.p.* vs. Δ*dotA* infected conditions, at both 1- and 8-hours post-infection.

A)

QC AB: percent Contaminants

| Control | dotA1h | dotA8h | WT1h | WT8h |

(Bar chart: Percent vs Contaminant; categories CON, PROT, REV for each)

B)

AB — log2(Intensity) vs samples Control-1, Control-2, Control-3, dotA1h-1, dotA1h-2, dotA1h-3, dotA8h-1, dotA8h-2, dotA8h-3, WT1h-1, WT1h-2, WT1h-3, WT8h-1, WT8h-2, WT8h-3

AB (normalized) — log2(Intensity) vs same samples

C)
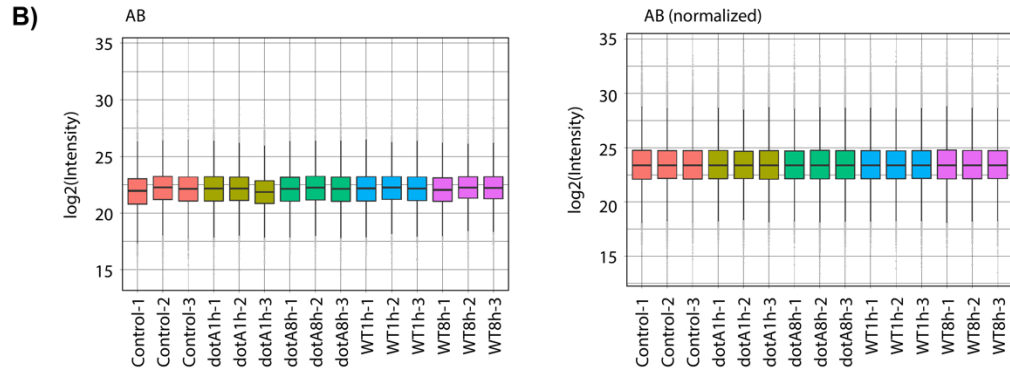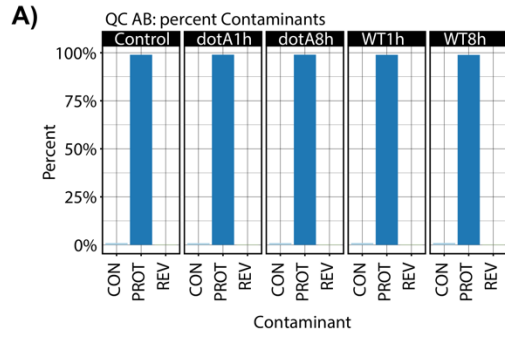
Dataset	Sample	# bioreplica	# bioreplica	n (# peptides)	r (correlation coefficient
AB	Control	1	2	35755	0.86
AB	Control	1	3	35755	0.88
AB	Control	2	3	35755	0.9
AB	WT1h	1	2	40087	0.87
AB	WT1h	1	3	40087	0.86
AB	WT1h	2	3	40087	0.87
AB	WT8h	1	2	40748	0.84
AB	WT8h	1	3	40748	0.84
AB	WT8h	2	3	40748	0.89
AB	dotA1h	1	2	39605	0.85
AB	dotA1h	1	3	39605	0.79
AB	dotA1h	2	3	39605	0.8
AB	dotA8h	1	2	40096	0.86
AB	dotA8h	1	3	40096	0.86
AB	dotA8h	2	3	40096	0.88

Correlation matrix (clustered) AB

D)

PCA AB

Dim 2 (3.15%) vs Dim 1 (91.73%)

WT 8hr
WT 1hr
ΔdotA 1hr
ΔdotA 8hr
Control
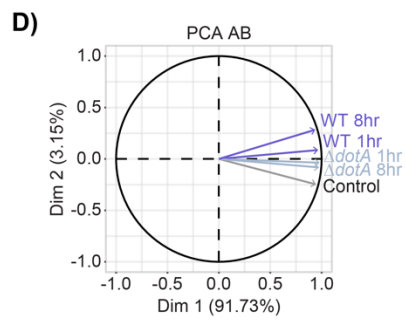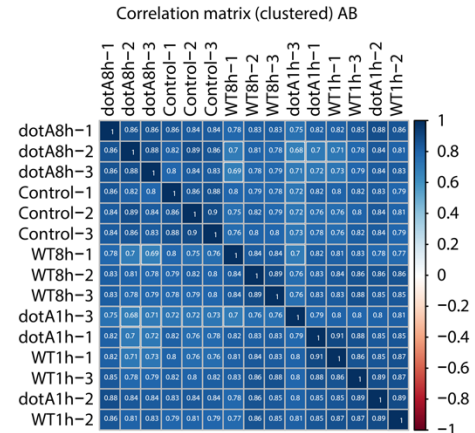
Supplementary Figure 3.1-3: Quantification and quality control plots of abundance data. Related to Figure 3.1. Identical analysis as in Figure 1S1 using abundance data.

119
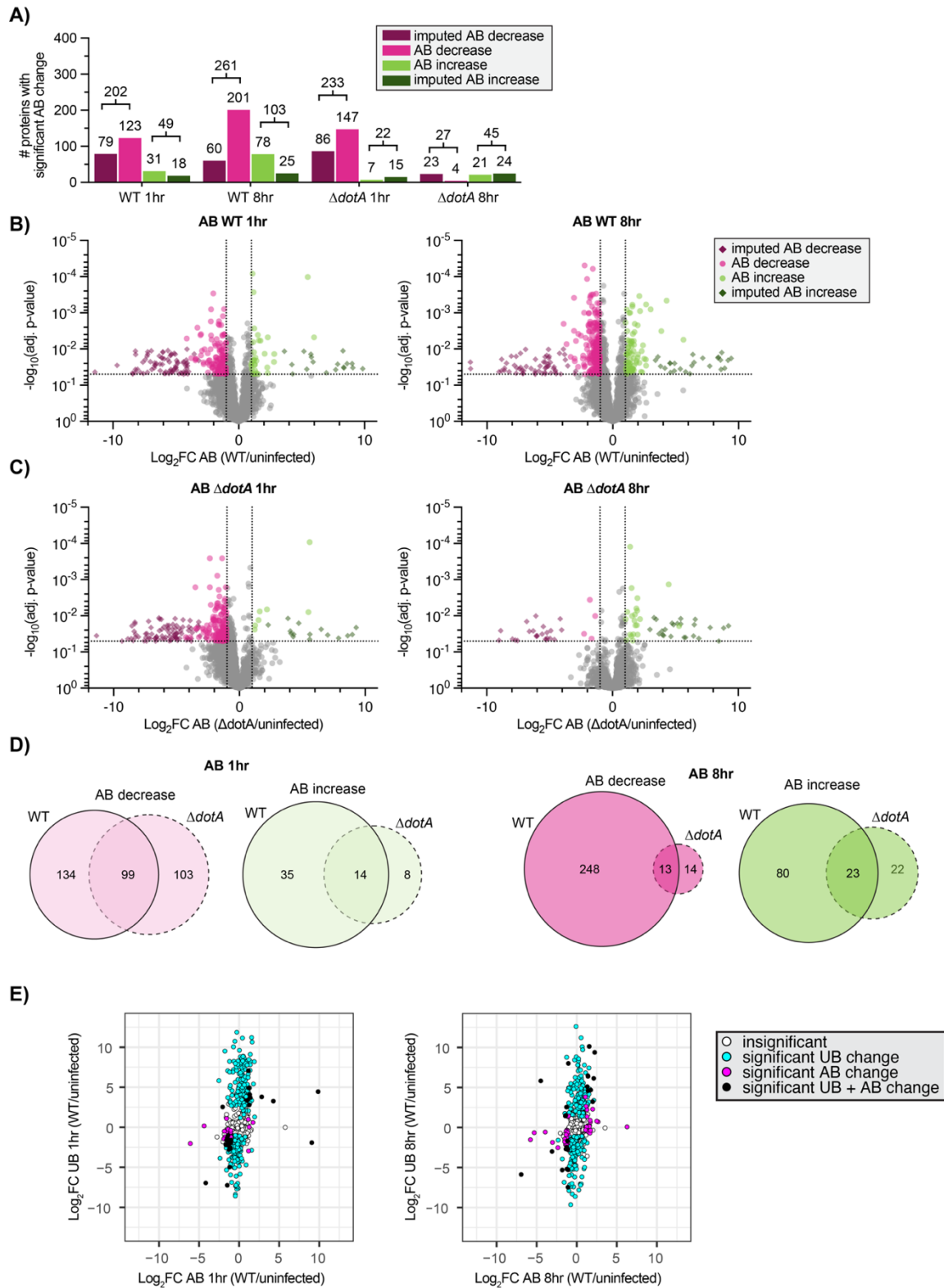
Supplementary Figure 3.1-4: Analysis of *L.p.*-induced changes in host cell abundance. Related to Figure 3.1. Analysis of proteins with significant increases (green) or decreases (magenta) in abundance compared to uninfected control for WT and Δ*dotA* infected conditions, at both 1 and 8 hours post infection. *Figure caption continued on the next page.*

Figure caption continued from the previous page. **(A)-(D)** Comparable to analyses in Fig 1 and Fig 1S2. **(E)** Log2FC comparison of proteins with significant abundance change (grey points), significant ubiquitination change (light blue points), or both significant abundance and ubiquitination change (dark blue points) during infection with WT *L.p.* relative to uninfected control. Proteins with insignificant abundance and ubiquitination changes are shown in white. Data shown are at 1-hour post-infection (left) and 8-hours post-infection (right).
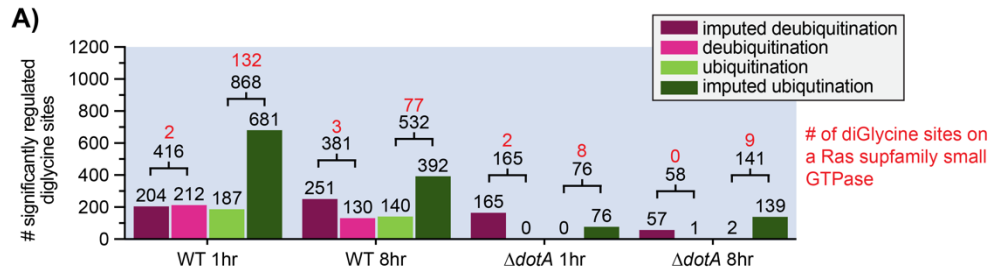
Supplementary Figure 3.2-1: Quantification of diGlycine site data. Related to Figure 3.2. Counts of diGly sites with a significant increase (green) or decrease (magenta) compared to uninfected control for the indicated infection conditions. Significance threshold: |log2(FC)|>1, p<0.05. DiGlycine sites falling on small GTPases indicated in red.
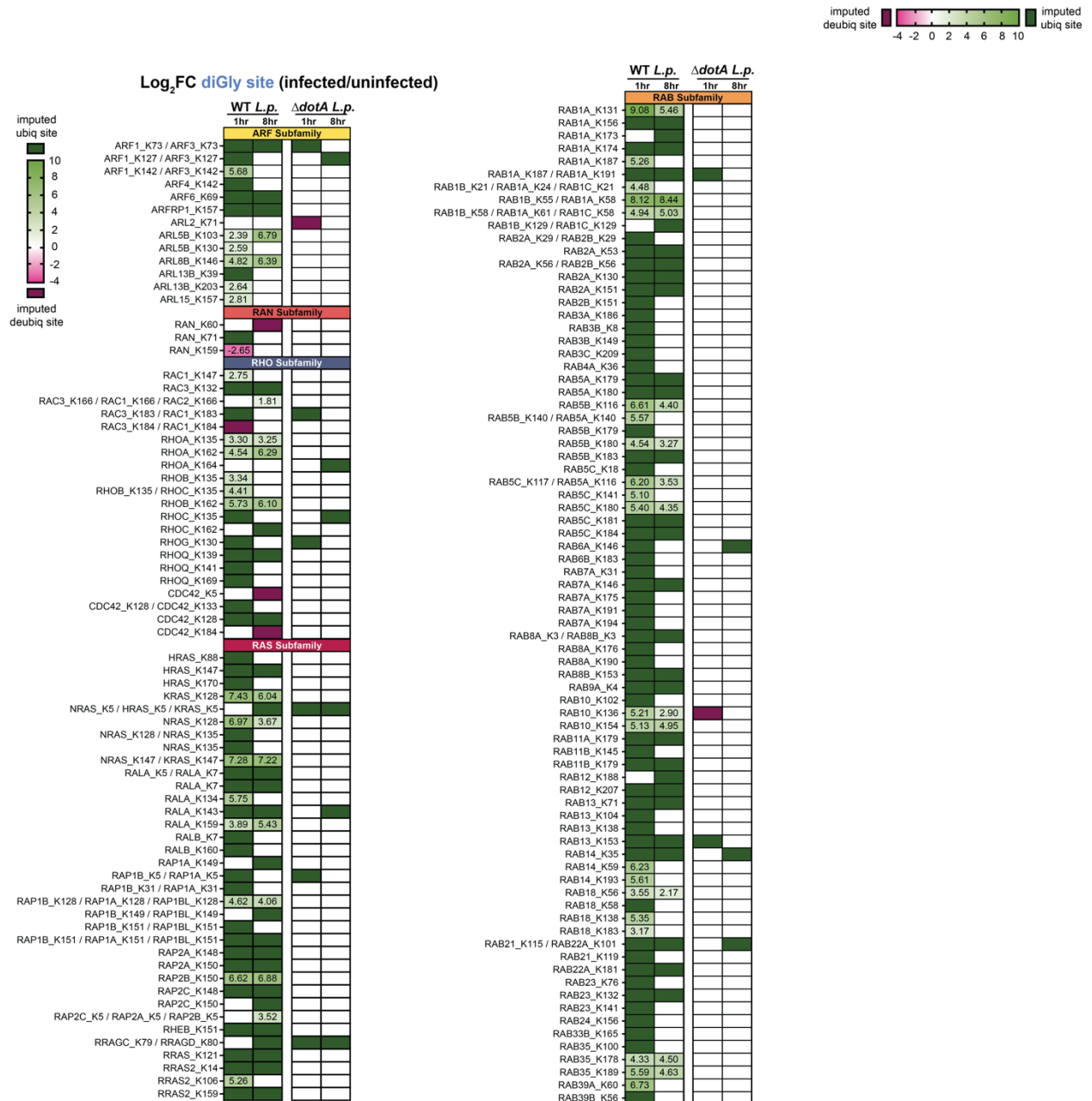
Supplementary Figure 3.2-2: List of significantly regulated diGly sites falling on small GTPases. Related to Figure 3.2. All significantly changing diGlycine sites falling on small GTPases during WT and Δ*dotA L.p.* infection, organized by subfamily and infection timepoint. Cell color and number indicate Log2FC. White cells indicate no significant change. Due to the significant homology between various small GTPases, some trypsinized peptides could not be distinguished between multiple proteins. DiGlycine sites that could be assigned to multiple proteins are indicated with a "/". In our downstream analyses, we use a conservative approach and only consider the first small GTPase listed (e.g. NRAS_K147 / KRAS_K147, only NRAS_K147 is counted as a small GTPase ubiquitination site).
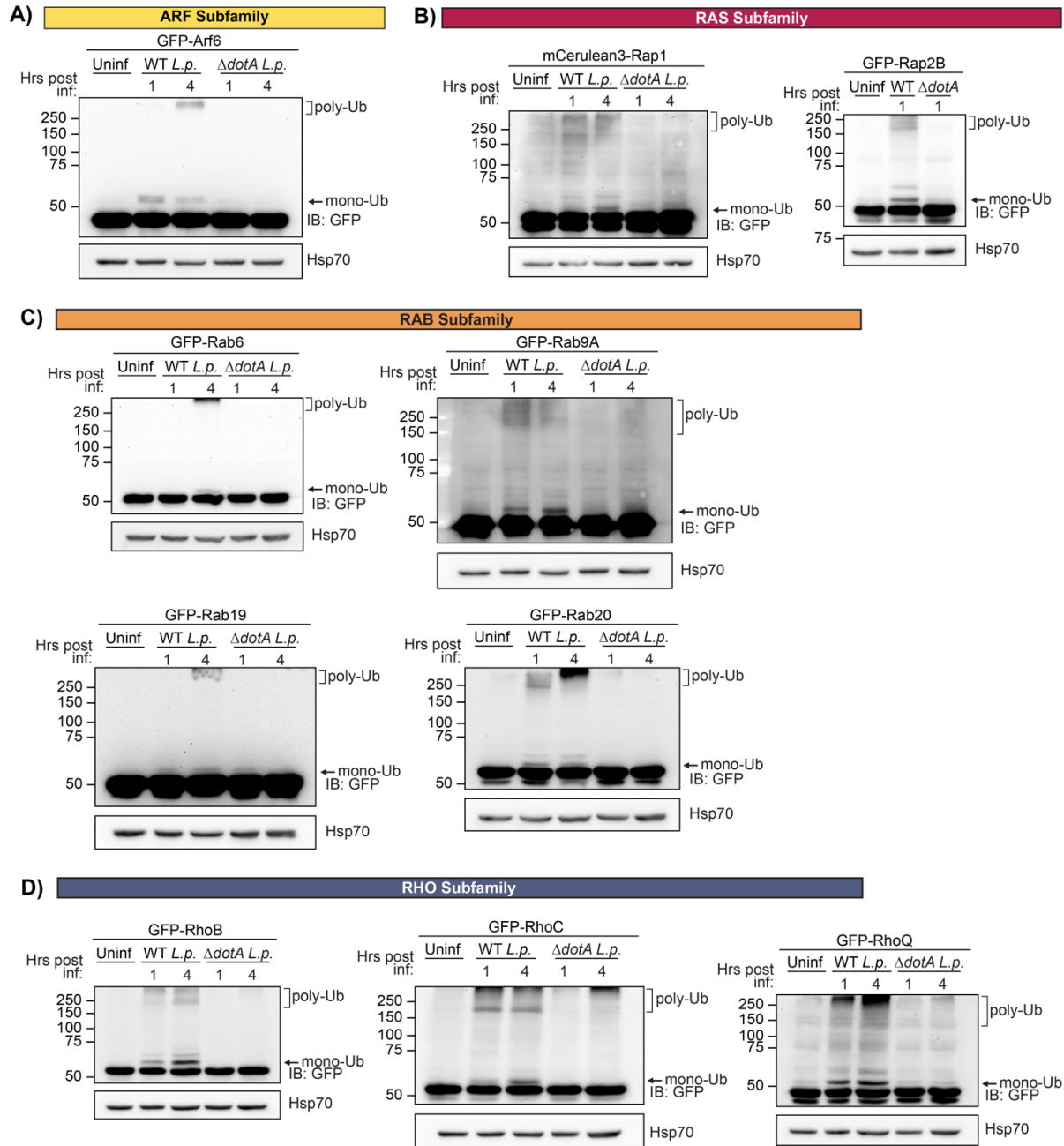
Supplementary Figure 3.2-3: Extended immunoblot analysis of small GTPase ubiquitination confirmations. Related to Figure 3.2. Extension of Figure 2B-E. Immunoblot analysis of lysates prepared from HEK293T FcγR cells transiently transfected with the indicated GFP-tagged small GTPase, then infected with either WT or Δ*dotA L.p.* for 1 to 4 hours, or left uninfected. Blots were probed with anti-GFP and anti-Hsp70 antibodies.
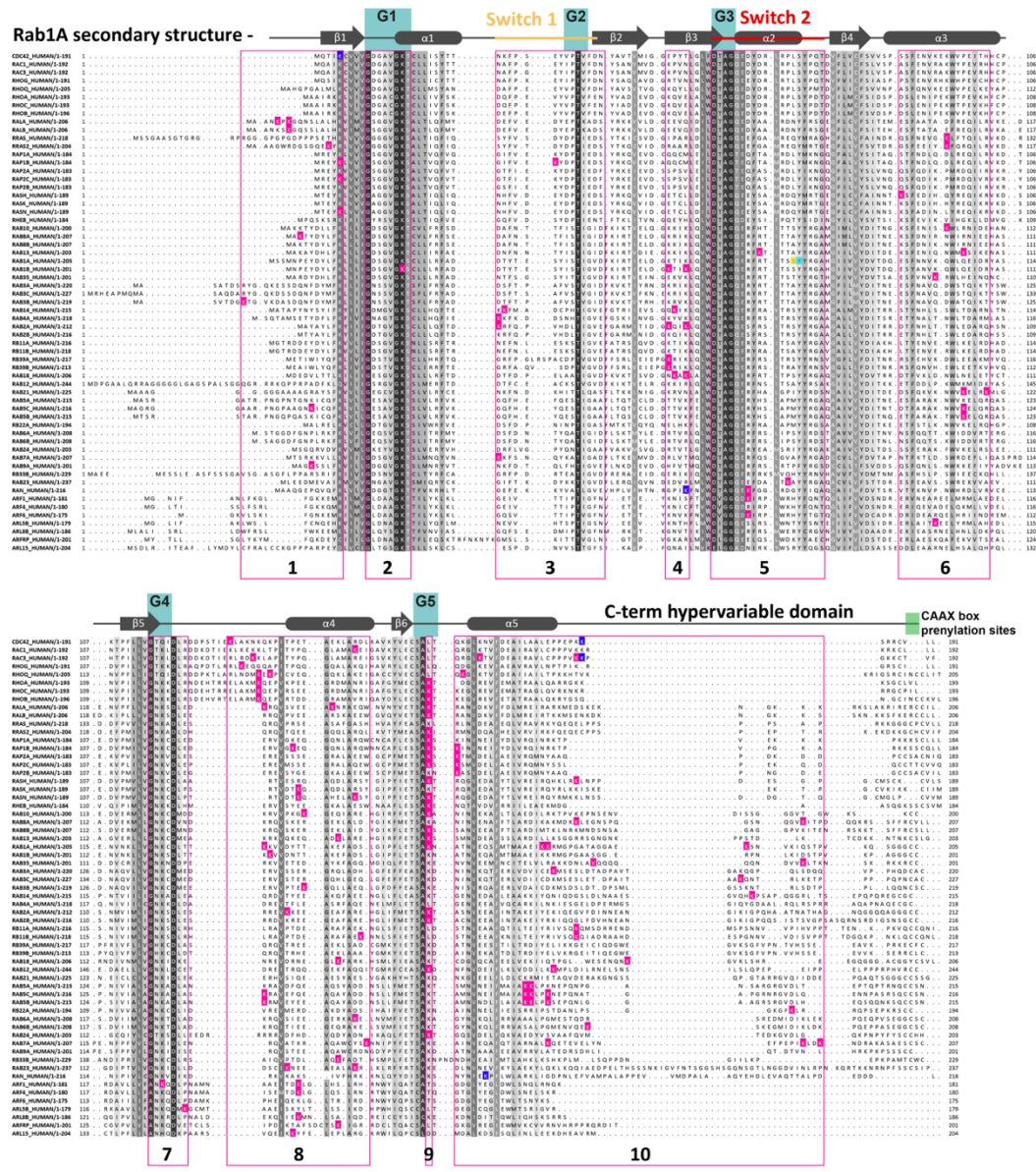
Supplementary Figure 3.3-1: Sequence alignment of ubiquitinated small GTPases with UB sites indicated. Related to Figure 3.3. Sequence alignment of small GTPases ubiquitinated during infection. 61 of 63 ubiquitinated small GTPases represented, with RRAGC and ARL13B omitted for visual clarity due to their significant length. Sequence colored by conservation within the small GTPase superfamily, from white (non-conserved) to black (extremely highly conserved residue). Ubiquitinated residues at either 1- or 8-hours post infection are colored in bright pink and outlined in black, and deubiquitinated residues are colored in dark blue. Structural and functional regions indicated above, using Rab1A as an example. Regions frequently ubiquitinated across detected small GTPases are underlined in pink and numbered 1-10. ARL13B_K39 and RRAGC_K79 fall in UB region #2. ARL13B_K203 falls in UB region #10.

125
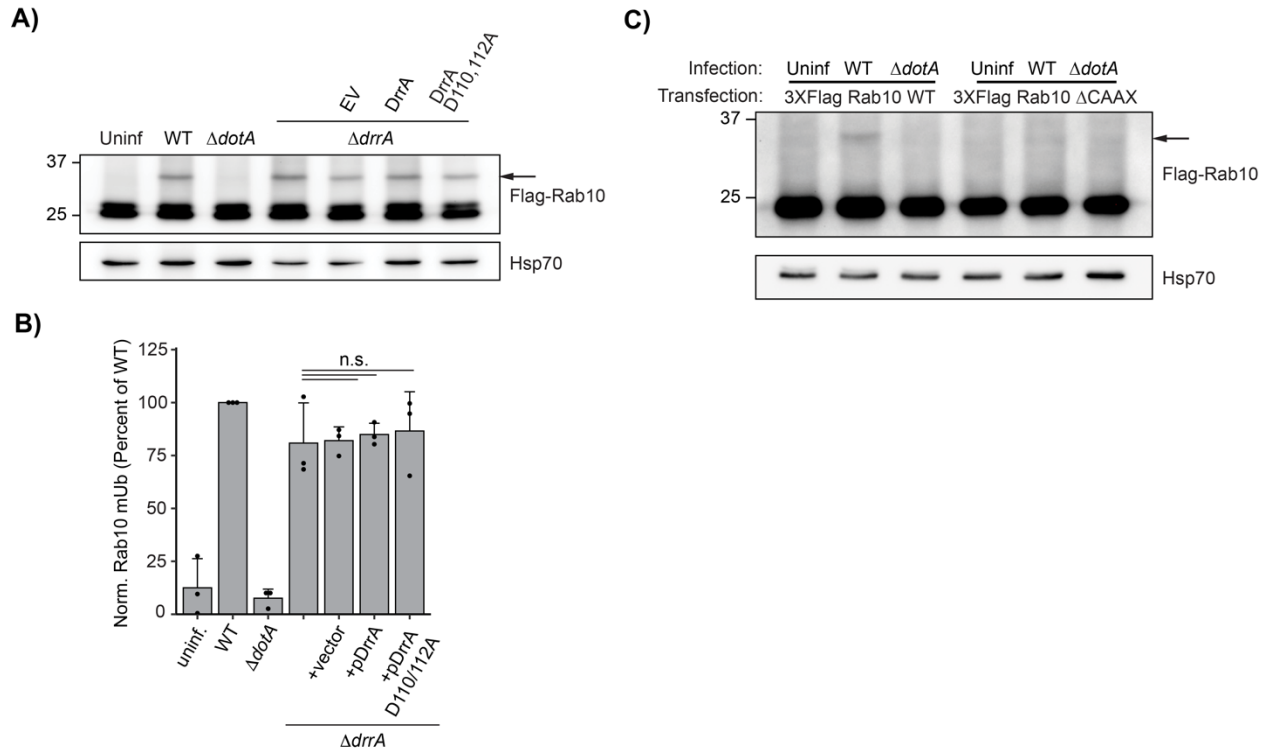
Supplementary Figure 3.4-1: Rab10 ubiquitination is not controlled by DrrA and requires membrane association. Related to Figure 3.4. (A) Immunoblot analysis of lysates prepared from HEK293T FcγR transfected with 3XFlag Rab10 and infected with a Δ*drrA L.p.* strain panel (WT, Δ*dotA*, Δ*drrA*, and Δ*drrA* complemented with empty vector or plasmid encoded DrrA WT or D110, 112A) for 1 hour (MOI=50). Monoubiquitinated Rab10 indicated with an arrow. **(B)** Quantification of biological replicates (N=3) of experiment shown in (A). Normalized Rab10 monoubiquitination intensity was calculated as a percentage of WT *L.p.* infection levels (see Methods). **(C)** Immunoblot analysis of monoubiquitination of Rab10 WT vs ΔCAAX during *L.p.* infection. HEK293T FcγR cells were transfected with either 3X Flag Rab10 WT or ΔCAAX, then infected with WT or Δ*dotA L.p.* for 1 hour (MOI=50) or left uninfected. Lysates were probed with anti-Flag antibody. Monoubiquitinated Rab10 indicated with an arrow.
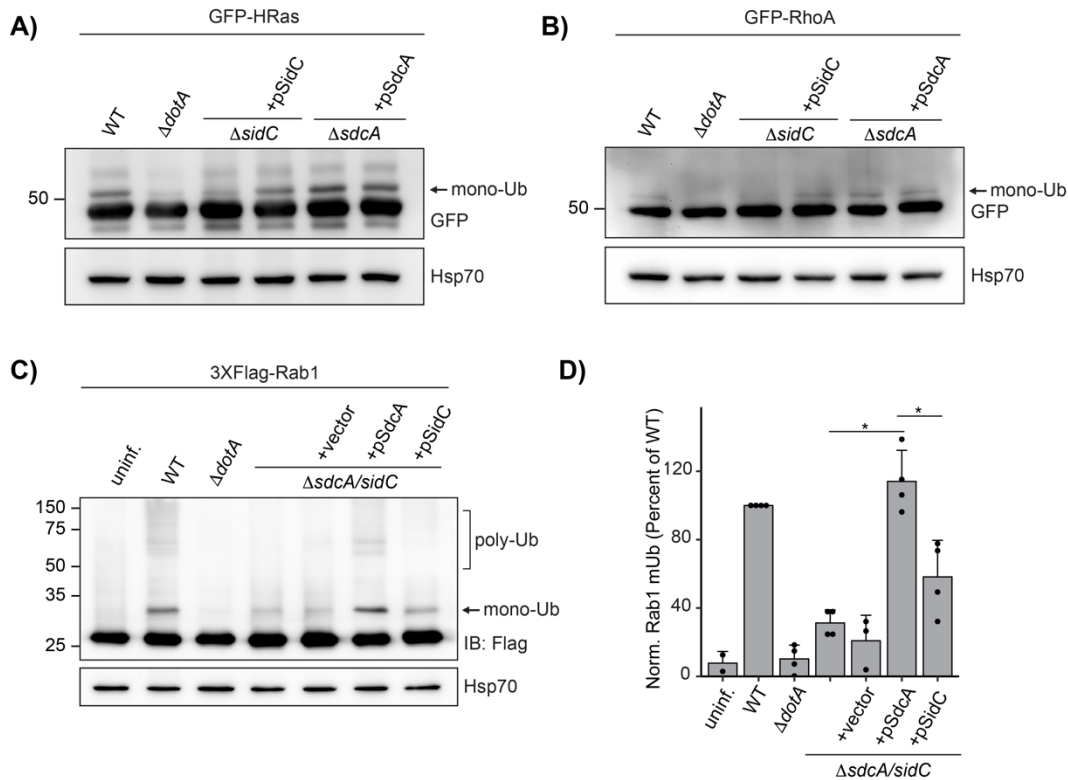
Supplementary Figure 3.5-1 : SidC and SdcA contribute differentially to small GTPase ubiquitination. Related to Figure 3.5. Immunoblot analysis of **(A)** HRas and **(B)** RhoA ubiquitination with SidC and SdcA single knockout strains. HEK293T FcγR cells transiently expressing the indicated GFP-tagged small GTPase were infected for 1 hour with L.p. WT, ΔdotA, ΔsidC, ΔsdcA, and appropriate plasmid complemented strains. Lysates were probed with anti-GFP and anti-HSP70 antibodies. **(C)** Immunoblot analysis of lysates prepared from HEK293T FcγR transfected with 3XFlag Rab1A and infected with a ΔsidC/sdcA L.p. strain panel (WT, ΔdotA, ΔsidC/sdcA, and ΔsidC/sdcA complemented with empty vector or plasmid encoded SdcA or SidC) for 1 hour (MOI=50). **(D)** Quantification of biological replicates (N=3) of experiment shown in **(A)**. Normalized Rab1A monoubiquitination intensity was calculated as a percentage of WT L.p. infection levels (see Methods). Bars represent mean value, error bars represent standard deviation. Individual points are values from each biological replicate. Statistical analysis of Western blot quantification: one-way ANOVA followed by Tukey-Kramer post-hoc test for each pair of means. * = p<0.05, n.s. = p>0.05.
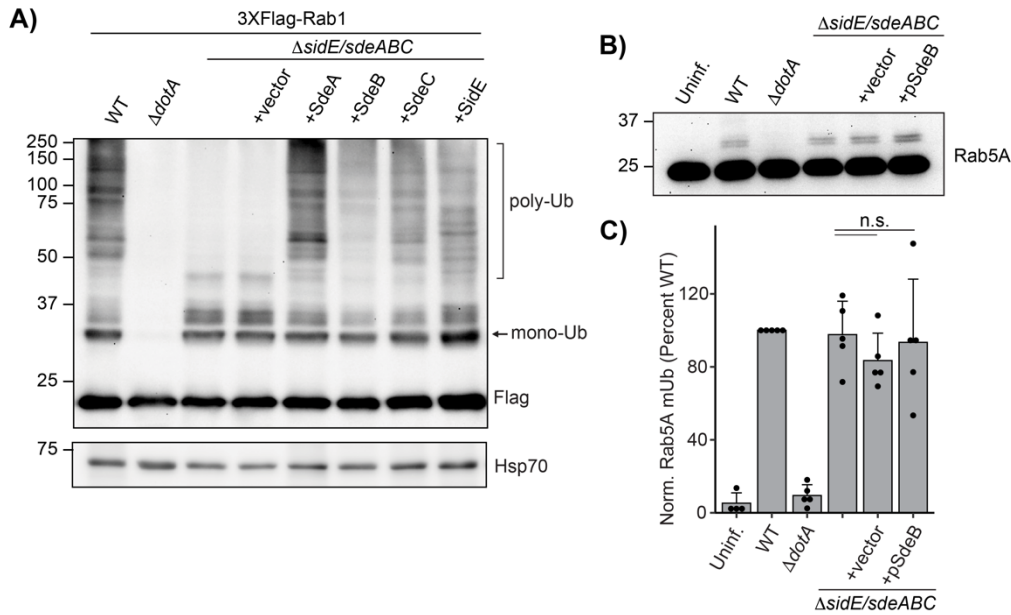
Supplementary Figure 3.6-1: The SidE family of effectors is required for poly- but not monoubiquitination of Rab1/5. Related to Figure 3.6. (A) Immunoblot analysis of Rab1 poly- and monoubiquitination during infection with a SidE family strain panel. HEK293T FcγR cells transiently expressing 3X-Flag Rab1A were infected for 1 hour with the indicated strain, and lysates were probed with anti-Flag and anti-Hsp70 antibodies. **(B)** HEK293T FcγR cells were infected for 4 hours with the indicated strain, and the lysates probed with anti-Rab5A antibody. **(C)** Normalized endogenous Rab5A monoubiquitination intensity was calculated as a percentage of WT *L.p.* infection levels (see Methods). Bars represent mean value (N=3-4), error bars represent standard deviation. Individual points are values from each biological replicate. *Statistical analysis of Western blot quantification*: one-way ANOVA followed by Tukey-Kramer post-hoc test for each pair of means. * = $p < 0.05$, n.s. = $p > 0.05$.

References

Ahola S, Langer T, MacVicar T. 2019. Mitochondrial Proteolysis and Metabolic Control. *Cold Spring Harb Perspect Biol* **11**:a033936. doi:10.1101/cshperspect.a033936

Aktories K, Schmidt G. 2014. Ras Superfamily Small G Proteins: Biology and Mechanisms 1, General Features, Signaling 65–97. doi:10.1007/978-3-7091-1806-1_4

Alkema MJ, Bronk M, Verhoeven E, Otte A, Veer LJ van 't, Berns A, Lohuizen M van. 1997. Identification of Bmi1-interacting proteins as constituents of a multimeric mammalian polycomb complex. *Gene Dev* **11**:226–240. doi:10.1101/gad.11.2.226

Ampofo E, Welker S, Jung M, Müller L, Greiner M, Zimmermann R, Montenarh M. 2013. CK2 phosphorylation of human Sec63 regulates its interaction with Sec62. *Biochimica Et Biophysica Acta Bba - Gen Subj* **1830**:2938–2945. doi:10.1016/j.bbagen.2012.12.020

An H, Ordureau A, Paulo JA, Shoemaker CJ, Denic V, Harper JW. 2019. TEX264 Is an Endoplasmic Reticulum-Resident ATG8-Interacting Protein Critical for ER Remodeling during Nutrient Stress. *Mol Cell* **74**:891-908.e10. doi:10.1016/j.molcel.2019.03.034

Anand IS, Choi W, Isberg RR. 2020. Components of the endocytic and recycling trafficking pathways interfere with the integrity of the Legionella-containing vacuole. *Cell Microbiol* **22**:e13151. doi:10.1111/cmi.13151

Anderson NS, Haynes CM. 2020. Folding the Mitochondrial UPR into the Integrated Stress Response. *Trends Cell Biol*, Trends in Cell Biology. doi:10.1016/j.tcb.2020.03.001

Andréasson C, Ott M, Büttner S. 2019. Mitochondria orchestrate proteostatic and metabolic stress responses. *Embo Rep* **20**:e47865. doi:10.15252/embr.201947865

Arasaki K, Mikami Y, Shames SR, Inoue H, Wakana Y, Tagaya M. 2017. Legionella effector Lpg1137 shuts down ER-mitochondria communication through cleavage of syntaxin 17. *Nat Commun* **8**:15406. doi:10.1038/ncomms15406

Arasaki K, Roy CR. 2010. Legionella pneumophila Promotes Functional Interactions between Plasma Membrane Syntaxins and Sec22b. *Traffic* **11**:587–600. doi:10.1111/j.1600-0854.2010.01050.x

Arnould T, Michel S, Renard P. 2015. Mitochondria Retrograde Signaling and the UPRmt: Where Are We in Mammals? *Int J Mol Sci* **16**:18224–18251. doi:10.3390/ijms160818224

Asrat S, Jesús DA de, Hempstead AD, Ramabhadran V, Isberg RR. 2014. Bacterial Pathogen Manipulation of Host Membrane Trafficking. *Annu Rev Cell Dev Biol* **30**:1–31. doi:10.1146/annurev-cellbio-100913-013439

Baker R, Lewis SM, Sasaki AT, Wilkerson EM, Locasale JW, Cantley LC, Kuhlman B, Dohlman HG, Campbell SL. 2013. Site-specific monoubiquitination activates Ras by impeding GTPase-activating protein function. *Nat Struct Mol Biol* **20**:46–52. doi:10.1038/nsmb.2430

Banga S, Gao P, Shen X, Fiscus V, Zong W-X, Chen L, Luo Z-Q. 2007. Legionella pneumophila inhibits macrophage apoptosis by targeting pro-death members of the Bcl2 protein family. *Proc National Acad Sci* **104**:5121–5126. doi:10.1073/pnas.0611030104

Belyi Y, Niggeweg R, Opitz B, Vogelsgesang M, Hippenstiel S, Wilm M, Aktories K. 2006. Legionella pneumophila glucosyltransferase inhibits host elongation factor 1A. *Proc National Acad Sci* **103**:16953–16958. doi:10.1073/pnas.0601562103

Belyi Y, Tabakova I, Stahl M, Aktories K. 2008. Lgt: a Family of Cytotoxic Glucosyltransferases Produced by Legionella pneumophila ▿ †. *J Bacteriol* **190**:3026–3035. doi:10.1128/jb.01798-07

Berger KH, Isberg RR. 1993. Two distinct defects in intracellular growth complemented by a single genetic locus in Legionella pneumophila. *Mol Microbiol* **7**:7–19. doi:10.1111/j.1365-2958.1993.tb01092.x

Berger KH, Merriam JJ, Isberg RR. 1994. Altered intracellular targeting properties associated with mutations in the Legionella pneumophila dotA gene. *Mol Microbiol* **14**:809–822. doi:10.1111/j.1365-2958.1994.tb01317.x

Best A, Kwaik YA. 2018. Evolution of the Arsenal of Legionella pneumophila Effectors To Modulate Protist Hosts. *Mbio* **9**:e01313-18. doi:10.1128/mbio.01313-18

Bhogaraju S, Bonn F, Mukherjee R, Adams M, Pfleiderer MM, Galej WP, Matkovic V, Lopez-Mosqueda J, Kalayil S, Shin D, Dikic I. 2019. Inhibition of bacterial ubiquitin ligases by SidJ–calmodulin catalysed glutamylation. *Nature* **572**:382–386. doi:10.1038/s41586-019-1440-8

Bhogaraju S, Kalayil S, Liu Y, Bonn F, Colby T, Matic I, Dikic I. 2016. Phosphoribosylation of Ubiquitin Promotes Serine Ubiquitination and Impairs Conventional Ubiquitination. *Cell* **167**:1636-1649.e13. doi:10.1016/j.cell.2016.11.019

Black MH, Osinski A, Gradowski M, Servage KA, Pawłowski K, Tomchick DR, Tagliabracci VS. 2019. Bacterial pseudokinase catalyzes protein polyglutamylation to inhibit the SidE-family ubiquitin ligases. *Science* **364**:787–792. doi:10.1126/science.aaw7446

Bruckert WM, Kwaik YA. 2015. Complete and Ubiquitinated Proteome of the Legionella-Containing Vacuole within Human Macrophages. *J Proteome Res* **14**:236–248. doi:10.1021/pr500765x

Budzik JM, Swaney DL, Jimenez-Morales D, Johnson JR, Garelis NE, Repasy T, Roberts AW, Popov LM, Parry TJ, Pratt D, Ideker T, Krogan NJ, Cox JS. 2020. Dynamic post-translational modification profiling of M. tuberculosis-infected primary macrophages. *Elife* **9**:e51461. doi:10.7554/elife.51461

Bueno M, Brands J, Voltz L, Fiedler K, Mays B, Croix CSt, Sembrat J, Mallampalli RK, Rojas M, Mora AL. 2018. ATF3 represses PINK1 gene transcription in lung epithelial cells to control mitochondrial homeostasis. *Aging Cell* **17**:e12720. doi:10.1111/acel.12720

Burdette DL, Monroe KM, Sotelo-Troha K, Iwig JS, Eckert B, Hyodo M, Hayakawa Y, Vance RE. 2011. STING is a direct innate immune sensor of cyclic di-GMP. *Nature* **478**:515–518. doi:10.1038/nature10429

Callegari S, Dennerlein S. 2018. Sensing the Stress: A Role for the UPRmt and UPRam in the Quality Control of Mitochondria. *Frontiers Cell Dev Biology* **6**:31. doi:10.3389/fcell.2018.00031

Camus SM, Camus MD, Figueras-Novoa C, Boncompain G, Sadacca LA, Esk C, Bigot A, Gould GW, Kioumourtzoglou D, Perez F, Bryant NJ, Mukherjee S, Brodsky FM. 2019. CHC22 clathrin mediates traffic from early secretory compartments for human GLUT4 pathway biogenesis. *J Cell Biol* **219**:e201812135. doi:10.1083/jcb.201812135

Carpenter AE, Jones TR, Lamprecht MR, Clarke C, Kang IH, Friman O, Guertin DA, Chang JH, Lindquist RA, Moffat J, Golland P, Sabatini DM. 2006. CellProfiler: image analysis software for identifying and quantifying cell phenotypes. *Genome Biol* **7**:R100. doi:10.1186/gb-2006-7-10-r100

Cherfils J, Zeghouf M. 2013. Regulation of Small GTPases by GEFs, GAPs, and GDIs. *Physiol Rev* **93**:269–309. doi:10.1152/physrev.00003.2012

Chino H, Hatta T, Natsume T, Mizushima N. 2019. Intrinsically Disordered Protein TEX264 Mediates ER-phagy. *Mol Cell* **74**:909-921.e6. doi:10.1016/j.molcel.2019.03.033

Choi M, Chang C-Y, Clough T, Broudy D, Killeen T, MacLean B, Vitek O. 2014. MSstats: an R package for statistical analysis of quantitative mass spectrometry-based proteomic experiments. *Bioinformatics* **30**:2524–2526. doi:10.1093/bioinformatics/btu305

Clemens DL, Lee B-Y, Horwitz MA. 2000. Deviant Expression of Rab5 on Phagosomes Containing the Intracellular Pathogens Mycobacterium tuberculosis and Legionella pneumophila Is Associated with Altered Phagosomal Fate. *Infect Immun* **68**:2671–2684. doi:10.1128/iai.68.5.2671-2684.2000

Cornejo E, Schlaermann P, Mukherjee S. 2017. How to rewire the host cell: A home improvement guide for intracellular bacteria. *J Cell Biol* **216**:3931–3948. doi:10.1083/jcb.201701095

Cox J, Hein MY, Luber CA, Paron I, Nagaraj N, Mann M. 2014. Accurate Proteome-wide Label-free Quantification by Delayed Normalization and Maximal Peptide Ratio Extraction, Termed MaxLFQ*. *Mol Cell Proteomics* **13**:2513–2526. doi:10.1074/mcp.m113.031591

Cox J, Mann M. 2008. MaxQuant enables high peptide identification rates, individualized p.p.b.-range mass accuracies and proteome-wide protein quantification. *Nature Biotechnology* **26**:1367–1372. doi:10.1038/nbt.1511

Degtyar E, Zusman T, Ehrlich M, Segal G. 2009. A Legionella effector acquired from protozoa is involved in sphingolipids metabolism and is targeted to the host cell mitochondria. *Cell Microbiol* **11**:1219–1235. doi:10.1111/j.1462-5822.2009.01328.x

Derré I, Isberg RR. 2004. Legionella pneumophila Replication Vacuole Formation Involves Rapid Recruitment of Proteins of the Early Secretory System. *Infect Immun* **72**:3048–3053. doi:10.1128/iai.72.5.3048-3053.2004

Dewhurst HM, Choudhury S, Torres MP. 2015. Structural Analysis of PTM Hotspots (SAPH-ire) – A Quantitative Informatics Method Enabling the Discovery of Novel Regulatory Elements in Protein Families* [S]. *Mol Cell Proteomics* **14**:2285–2297. doi:10.1074/mcp.m115.051177

Dohlman HG, Campbell SL. 2019. Regulation of large and small G proteins by ubiquitination. *J Biol Chem* **294**:18613–18623. doi:10.1074/jbc.rev119.011068

Dolezal P, Aili M, Tong J, Jiang J-H, Marobbio CMT, Marobbio CM, Lee SF, Schuelein R, Belluzzo S, Binova E, Mousnier A, Frankel G, Giannuzzi G, Palmieri F, Gabriel K, Naderer T, Hartland EL, Lithgow T. 2012. Legionella pneumophila Secretes a Mitochondrial Carrier Protein during Infection. *Plos Pathog* **8**:e1002459. doi:10.1371/journal.ppat.1002459

Doncheva NT, Morris JH, Gorodkin J, Jensen LJ. 2019. Cytoscape StringApp: Network Analysis and Visualization of Proteomics Data. *J Proteome Res* **18**:623–632. doi:10.1021/acs.jproteome.8b00702

Dorer MS, Kirton D, Bader JS, Isberg RR. 2006. RNA Interference Analysis of Legionella in Drosophila Cells: Exploitation of Early Secretory Apparatus Dynamics. *Plos Pathog* **2**:e34. doi:10.1371/journal.ppat.0020034

Dotto VD, Fogazza M, Carelli V, Rugolo M, Zanna C. 2018. Eight human OPA1 isoforms, long and short: What are they for? *Biochimica Et Biophysica Acta Bba - Bioenergetics* **1859**:263–269. doi:10.1016/j.bbabio.2018.01.005

Duncan ED, Han K-J, Trout MA, Prekeris R. 2022. Ubiquitylation by Rab40b/Cul5 regulates Rap2 localization and activity during cell migration. *J Cell Biol* **221**:e202107114. doi:10.1083/jcb.202107114

Dwingelo JV, Chung IYW, Price CT, Li L, Jones S, Cygler M, Kwaik YA. 2019. Interaction of the Ankyrin H Core Effector of Legionella with the Host LARP7 Component of the 7SK snRNP Complex. *Mbio* **10**:e01942-19. doi:10.1128/mbio.01942-19

Emmerich CH, Cohen P. 2015. Optimising methods for the preservation, capture and identification of ubiquitin chains and ubiquitylated proteins by immunoblotting. *Biochem Bioph Res Co* **466**:1–14. doi:10.1016/j.bbrc.2015.08.109

Escoll P, Song O-R, Viana F, Steiner B, Lagache T, Olivo-Marin J-C, Impens F, Brodin P, Hilbi H, Buchrieser C. 2017. Legionella pneumophila Modulates Mitochondrial Dynamics to Trigger Metabolic Repurposing of Infected Macrophages. *Cell Host Microbe* **22**:302-316.e7. doi:10.1016/j.chom.2017.07.020

Eura Y. 2003. Two Mitofusin Proteins, Mammalian Homologues of FZO, with Distinct Functions Are Both Required for Mitochondrial Fusion. *J Biochem* **134**:333–344. doi:10.1093/jb/mvg150

Fajardo M, Schleicher M, Noegel A, Bozzaro S, Killinger S, Heuner K, Hacker J, Steinert M. 2004. Calnexin, calreticulin and cytoskeleton-associated proteins modulate uptake and growth of Legionella pneumophila in Dictyostelium discoideum. *Microbiology+* **150**:2825–2835. doi:10.1099/mic.0.27111-0

Ferreira CB, Sumner RP, Rodriguez-Plata MT, Rasaiyaah J, Milne RS, Thrasher AJ, Qasim W, Towers GJ. 2020. Lentiviral Vector Production Titer Is Not Limited in HEK293T by Induced Intracellular Innate Immunity. *Mol Ther - Methods Clin Dev* **17**:209–219. doi:10.1016/j.omtm.2019.11.021

Fessler E, Eckl E-M, Schmitt S, Mancilla IA, Meyer-Bender MF, Hanf M, Philippou-Massier J, Krebs S, Zischka H, Jae LT. 2020. A pathway coordinated by DELE1 relays mitochondrial stress to the cytosol. *Nature* **579**:433–437. doi:10.1038/s41586-020-2076-4

Fiskin E, Bionda T, Dikic I, Behrends C. 2016. Global Analysis of Host and Bacterial Ubiquitinome in Response to Salmonella Typhimurium Infection. *Mol Cell* **62**:967–981. doi:10.1016/j.molcel.2016.04.015

Fontana MF, Banga S, Barry KC, Shen X, Tan Y, Luo Z-Q, Vance RE. 2011. Secreted Bacterial Effectors That Inhibit Host Protein Synthesis Are Critical for Induction of the Innate Immune Response to Virulent Legionella pneumophila. *Plos Pathog* **7**:e1001289. doi:10.1371/journal.ppat.1001289

Fontana MF, Shin S, Vance RE. 2012. Activation of Host Mitogen-Activated Protein Kinases by Secreted Legionella pneumophila Effectors That Inhibit Host Protein Translation. *Infect Immun* **80**:3570–3575. doi:10.1128/iai.00557-12

Francione L, Smith PK, Accari SL, Taylor PE, Bokko PB, Bozzaro S, Beech PL, Fisher PR. 2009. Legionella pneumophila multiplication is enhanced by chronic AMPK signalling in mitochondrially diseased Dictyostelium cells. *Dis Model Mech* **2**:479–489. doi:10.1242/dmm.003319

Fu L, Kilberg MS. 2013. Elevated cJUN expression and an ATF/CRE site within the ATF3 promoter contribute to activation of ATF3 transcription by the amino acid response. *Physiol Genomics* **45**:127–137. doi:10.1152/physiolgenomics.00160.2012

Gan N, Guan H, Huang Y, Yu T, Fu J, Nakayasu ES, Puvar K, Das C, Wang D, Ouyang S, Luo Z. 2020. Legionella pneumophila regulates the activity of UBE2N by deamidase-mediated deubiquitination. *Embo J* **39**:e102806. doi:10.15252/embj.2019102806

Giacomello M, Pyakurel A, Glytsou C, Scorrano L. 2020. The cell biology of mitochondrial membrane dynamics. *Nat Rev Mol Cell Bio*, Nature Reviews Molecular Cell Biology. doi:10.1038/s41580-020-0210-7

Gomez-Valero L, Buchrieser C. 2019. Intracellular parasitism, the driving force of evolution of Legionella pneumophila and the genus Legionella. *Microbes Infect* **21**:230–236. doi:10.1016/j.micinf.2019.06.012

Goody RS, Müller MP, Wu Y-W. 2017. Mechanisms of action of Rab proteins, key regulators of intracellular vesicular transport. *Biol Chem* **398**:565–575. doi:10.1515/hsz-2016-0274

Guo X, Aviles G, Liu Y, Tian R, Unger BA, Lin Y-HT, Wiita AP, Xu K, Correia MA, Kampmann M. 2020. Mitochondrial stress is relayed to the cytosol by an OMA1–DELE1–HRI pathway. *Nature* **579**:427–432. doi:10.1038/s41586-020-2078-2

Hai T, Wolfgang CD, Marsee DK, Allen AE, Sivaprasad U. 1999. ATF3 and stress responses. *Gene Expression* **7**:321–35.

Harada T, Miyake M, Imai Y. 2007. Evasion of Legionella pneumophila from the Bactericidal System by Reactive Oxygen Species (ROS) in Macrophages. *Microbiol Immunol* **51**:1161–1170. doi:10.1111/j.1348-0421.2007.tb04011.x

Hardiman CA, Roy CR. 2014. AMPylation Is Critical for Rab1 Localization to Vacuoles Containing Legionella pneumophila. *Mbio* **5**:e01035-13. doi:10.1128/mbio.01035-13

Hoffmann C, Finsel I, Otto A, Pfaffinger G, Rothmeier E, Hecker M, Becher D, Hilbi H. 2014. Functional analysis of novel Rab GTPases identified in the proteome of purified Legionella-containing vacuoles from macrophages. *Cell Microbiol* **16**:1034–1052. doi:10.1111/cmi.12256

Homma Y, Hiragi S, Fukuda M. 2021. Rab family of small GTPases: an updated view on their regulation and functions. *Febs J* **288**:36–55. doi:10.1111/febs.15453

Horenkamp FA, Mukherjee S, Alix E, Schauder CM, Hubber AM, Roy CR, Reinisch KM. 2014. Legionella pneumophila Subversion of Host Vesicular Transport by SidC Effector Proteins. *Traffic* **15**:488–499. doi:10.1111/tra.12158

Horibe T, Hoogenraad NJ. 2007. The Chop Gene Contains an Element for the Positive Regulation of the Mitochondrial Unfolded Protein Response. *Plos One* **2**:e835. doi:10.1371/journal.pone.0000835

Hornung V, Rothenfusser S, Britsch S, Krug A, Jahrsdörfer B, Giese T, Endres S, Hartmann G. 2002. Quantitative Expression of Toll-Like Receptor 1–10 mRNA in Cellular Subsets of Human Peripheral Blood Mononuclear Cells and Sensitivity to CpG Oligodeoxynucleotides. *J Immunol* **168**:4531–4537. doi:10.4049/jimmunol.168.9.4531

Horwitz MA. 1983. Formation of a novel phagosome by the Legionnaires' disease bacterium (Legionella pneumophila) in human monocytes. *J Exp Medicine* **158**:1319–1331. doi:10.1084/jem.158.4.1319

Hsu F, Luo X, Qiu J, Teng Y-B, Jin J, Smolka MB, Luo Z-Q, Mao Y. 2014. The Legionella effector SidC defines a unique family of ubiquitin ligases important for bacterial phagosomal remodeling. *Proc National Acad Sci* **111**:10538–10543. doi:10.1073/pnas.1402605111

Hubber A, Roy CR. 2010. Modulation of Host Cell Function by Legionella pneumophila Type IV Effectors. *Annu Rev Cell Dev Bi* **26**:261–283. doi:10.1146/annurev-cellbio-100109-104034

Hulsen T. 2022. DeepVenn -- a web application for the creation of area-proportional Venn diagrams using the deep learning framework Tensorflow.js. *arXiv*. doi:10.48550/arxiv.2210.04597

Ingmundson A, Delprato A, Lambright DG, Roy CR. 2007. Legionella pneumophila proteins that regulate Rab1 membrane cycling. *Nature* **450**:365–369. doi:10.1038/nature06336

Ivanov SS, Roy CR. 2013. Pathogen signatures activate a ubiquitination pathway that modulates the function of the metabolic checkpoint kinase mTOR. *Nat Immunol* **14**:1219–1228. doi:10.1038/ni.2740

Ivanov SS, Roy CR. 2009. Modulation of ubiquitin dynamics and suppression of DALIS formation by the Legionella pneumophila Dot/Icm system. *Cell Microbiol* **11**:261–278. doi:10.1111/j.1462-5822.2008.01251.x

Jadhav K, Zhang Y. 2017. Activating transcription factor 3 in immune response and metabolic regulation. *Liver Res* **1**:96–102. doi:10.1016/j.livres.2017.08.001

Jaeschke A, Karasarides M, Ventura J-J, Ehrhardt A, Zhang C, Flavell RA, Shokat KM, Davis RJ. 2006. JNK2 Is a Positive Regulator of the cJun Transcription Factor. *Mol Cell* **23**:899–911. doi:10.1016/j.molcel.2006.07.028

Jeng EE, Bhadkamkar V, Ibe NU, Gause H, Jiang L, Chan J, Jian R, Jimenez-Morales D, Stevenson E, Krogan NJ, Swaney DL, Snyder MP, Mukherjee S, Bassik MC. 2019. Systematic Identification of Host Cell Regulators of Legionella pneumophila Pathogenesis Using a Genome-wide CRISPR Screen. *Cell Host Microbe* **26**:551-563.e6. doi:10.1016/j.chom.2019.08.017

Jeong KC, Sexton JA, Vogel JP. 2015. Spatiotemporal Regulation of a Legionella pneumophila T4SS Substrate by the Metaeffector SidJ. *Plos Pathog* **11**:e1004695. doi:10.1371/journal.ppat.1004695

Jimenez-Morales D, Campos AR, Dollen JV. 2019. artMS: Analytical R tools for Mass Spectrometry. *Bioconductor*.

Jimenez-Morales D, Turaga N, Dollen JV, Bpolacco, Campos A, Zhouyuan A, Obenchain V, King E. 2023. biodavidjm/artMS: artMS for Zenodo. Zenodo.

Kagan JC, Roy CR. 2002. Legionella phagosomes intercept vesicular traffic from endoplasmic reticulum exit sites. *Nat Cell Biol* **4**:945–954. doi:10.1038/ncb883

Kagan JC, Stein M-P, Pypaert M, Roy CR. 2004. Legionella Subvert the Functions of Rab1 and Sec22b to Create a Replicative Organelle. *J Exp Medicine* **199**:1201–1211. doi:10.1084/jem.20031706

Kalayil S, Bhogaraju S, Bonn F, Shin D, Liu Y, Gan N, Basquin J, Grumati P, Luo Z-Q, Dikic I. 2018. Insights into catalysis and function of phosphoribosyl-linked serine ubiquitination. *Nature* **557**:734–738. doi:10.1038/s41586-018-0145-8

Kallunki T, Su B, Tsigelny I, Sluss HK, Dérijard B, Moore G, Davis R, Karin M. 1994. JNK2 contains a specificity-determining region responsible for efficient c-Jun binding and phosphorylation. *Gene Dev* **8**:2996–3007. doi:10.1101/gad.8.24.2996

Kang BH, Plescia J, Song HY, Meli M, Colombo G, Beebe K, Scroggins B, Neckers L, Altieri DC. 2009. Combinatorial drug design targeting multiple cancer signaling networks controlled by mitochondrial Hsp90. *J Clin Invest* **119**:454–464. doi:10.1172/jci37613

Kawabata M, Matsuo H, Koito T, Murata M, Kubori T, Nagai H, Tagaya M, Arasaki K. 2021. Legionella hijacks the host Golgi-to-ER retrograde pathway for the association of Legionella-containing vacuole with the ER. *PLoS Pathog* **17**:e1009437. doi:10.1371/journal.ppat.1009437

Kenny TC, Craig AJ, Villanueva A, Germain D. 2019. Mitohormesis Primes Tumor Invasion and Metastasis. *Cell Reports* **27**:2292-2303.e6. doi:10.1016/j.celrep.2019.04.095

Kholmanskikh S, Singh S, Ross ME. 2022. Activation of RhoC by regulatory ubiquitination is mediated by LNX1 and suppressed by LIS1. *Sci Rep-uk* **12**:16493. doi:10.1038/s41598-022-19740-1

Kim S, Isberg RR. 2023. The Sde Phosphoribosyl-Linked Ubiquitin Transferases protect the Legionella pneumophila vacuole from degradation by the host. doi:10.1101/2023.03.19.533379

Kim W, Bennett EJ, Huttlin EL, Guo A, Li J, Possemato A, Sowa ME, Rad R, Rush J, Comb MJ, Harper JW, Gygi SP. 2011. Systematic and Quantitative Assessment of the Ubiquitin-Modified Proteome. *Mol Cell* **44**:325–340. doi:10.1016/j.molcel.2011.08.025

Klausner RD, Donaldson JG, Lippincott-Schwartz J. 1992. Brefeldin A: insights into the control of membrane traffic and organelle structure. *J cell Biol* **116**:1071–1080. doi:10.1083/jcb.116.5.1071

Komander D, Rape M. 2012. The Ubiquitin Code. *Annu Rev Biochem* **81**:203–229. doi:10.1146/annurev-biochem-060310-170328

Kotewicz KM, Ramabhadran V, Sjoblom N, Vogel JP, Haenssler E, Zhang M, Behringer J, Scheck RA, Isberg RR. 2017. A Single Legionella Effector Catalyzes a Multistep Ubiquitination Pathway to Rearrange Tubular Endoplasmic Reticulum for Replication. *Cell Host Microbe* **21**:169–181. doi:10.1016/j.chom.2016.12.007

Kowalczyk B, Chmiel E, Palusinska-Szysz M. 2021. The Role of Lipids in Legionella-Host Interaction. *Int J Mol Sci* **22**:1487. doi:10.3390/ijms22031487

Ku H-C, Cheng C-F. 2020. Master Regulator Activating Transcription Factor 3 (ATF3) in Metabolic Homeostasis and Cancer. *Front Endocrinol* **11**:556. doi:10.3389/fendo.2020.00556

Lachance V, Degrandmaison J, Marois S, Robitaille M, Génier S, Nadeau S, Angers S, Parent J-L. 2013. Ubiquitylation and activation of a Rab GTPase is promoted by a β2AR–HACE1 complex. *J Cell Sci* **127**:111–123. doi:10.1242/jcs.132944

Laguna RK, Creasey EA, Li Z, Valtz N, Isberg RR. 2006. A Legionella pneumophila-translocated substrate that is required for growth within macrophages and protection from host cell death. *Proc National Acad Sci* **103**:18745–18750. doi:10.1073/pnas.0609012103

Lebeau J, Rainbolt TK, Wiseman RL. 2018. Chapter Three: Coordinating Mitochondrial Biology Through the Stress-Responsive Regulation of Mitochondrial ProteasesInternational Review of Cell and Molecular Biology. pp. 79–128. doi:10.1016/bs.ircmb.2018.05.003

Lei Z, Wang J, Zhang L, Liu CH. 2021. Ubiquitination-Dependent Regulation of Small GTPases in Membrane Trafficking: From Cell Biology to Human Diseases. *Frontiers Cell Dev Biology* **9**:688352. doi:10.3389/fcell.2021.688352

Levin RS, Hertz NT, Burlingame AL, Shokat KM, Mukherjee S. 2016. Innate immunity kinase TAK1 phosphorylates Rab1 on a hotspot for posttranslational modifications by host and pathogen. *Proc National Acad Sci* **113**:E4776–E4783. doi:10.1073/pnas.1608355113

Liu S, Jiwei L, Zhen X, Qiu J, Ouyang S, Luo Z-Q. 2020. Interplay between bacterial deubiquitinase and ubiquitin E3 ligase regulates ubiquitin dynamics on Legionella phagosomes. Elife 9:e58114. doi:10.7554/elife.58114

Li T, Lu Q, Wang G, Xu H, Huang H, Cai T, Kan B, Ge J, Shao F. 2013. SET-domain bacterial effectors target heterochromatin protein 1 to activate host rDNA transcription. *Embo Rep* **14**:733–740. doi:10.1038/embor.2013.86

Li X, Anderson DE, Chang Y-Y, Jarnik M, Machner MP. 2022. VpdC is a ubiquitin-activated phospholipase effector that regulates Legionella vacuole expansion during infection. *P Natl Acad Sci Usa* **119**:e2209149119. doi:10.1073/pnas.2209149119

Liu Y, Zhu W, Tan Y, Nakayasu ES, Staiger CJ, Luo Z-Q. 2017. A Legionella Effector Disrupts Host Cytoskeletal Structure by Cleaving Actin. *Plos Pathog* **13**:e1006186. doi:10.1371/journal.ppat.1006186

Lockwood DC, Amin H, Costa TRD, Schroeder GN. 2022. The Legionella pneumophila Dot/Icm type IV secretion system and its effectors: This article is part of the Bacterial Cell Envelopes collection. *Microbiology+* **168**. doi:10.1099/mic.0.001187

López-Sánchez I, Sanz-García M, Lazo PA. 2009. Plk3 Interacts with and Specifically Phosphorylates VRK1 in Ser342, a Downstream Target in a Pathway That Induces Golgi Fragmentation ▽ †. *Mol Cell Biol* **29**:1189–1201. doi:10.1128/mcb.01341-08

Luo J, Wang L, Song L, Luo Z-Q. 2021. Exploitation of the Host Ubiquitin System: Means by Legionella pneumophila. *Front Microbiol* **12**:790442. doi:10.3389/fmicb.2021.790442

Luo Z-Q, Isberg RR. 2004. Multiple substrates of the Legionella pneumophila Dot/Icm system identified by interbacterial protein transfer. *P Natl Acad Sci Usa* **101**:841–846. doi:10.1073/pnas.0304916101

Machner MP, Isberg RR. 2006. Targeting of Host Rab GTPase Function by the Intravacuolar Pathogen Legionella pneumophila. *Dev Cell* **11**:47–56. doi:10.1016/j.devcel.2006.05.013

MacVicar T, Ohba Y, Nolte H, Mayer FC, Tatsuta T, Sprenger H-G, Lindner B, Zhao Y, Li J, Bruns C, Krüger M, Habich M, Riemer J, Schwarzer R, Pasparakis M, Henschke S, Brüning JC, Zamboni N, Langer T. 2019. Lipid signalling drives proteolytic rewiring of mitochondria by YME1L. *Nature* **575**:361–365. doi:10.1038/s41586-019-1738-6

McKeehan W, Hardesty B. 1969. The mechanism of cycloheximide inhibition of protein synthesis in rabbit reticulocytes. *Biochem Biophys Res Commun* **36**:625–630. doi:10.1016/0006-291x(69)90351-9

Meng Q, Xia Y. 2011. c-Jun, at the crossroad of the signaling network. *Protein Cell* **2**:889–898. doi:10.1007/s13238-011-1113-3

Mertins P, Qiao JW, Patel J, Udeshi ND, Clauser KR, Mani DR, Burgess MW, Gillette MA, Jaffe JD, Carr SA. 2013. Integrated proteomic analysis of post-translational modifications by serial enrichment. *Nat Methods* **10**:634–637. doi:10.1038/nmeth.2518

Metz KS, Deoudes EM, Berginski ME, Jimenez-Ruiz I, Aksoy BA, Hammerbacher J, Gomez SM, Phanstiel DH. 2018. Coral: Clear and Customizable Visualization of Human Kinome Data. *Cell Syst* **7**:347-350.e1. doi:10.1016/j.cels.2018.07.001

Michard C, Doublet P. 2015. Post-translational modifications are key players of the Legionella pneumophila infection strategy. *Front Microbiol* **6**:87. doi:10.3389/fmicb.2015.00087

Moss SM, Taylor IR, Ruggero D, Gestwicki JE, Shokat KM, Mukherjee S. 2019. A Legionella pneumophila Kinase Phosphorylates the Hsp70 Chaperone Family to Inhibit Eukaryotic Protein Synthesis. *Cell Host Microbe* **25**:454-462.e6. doi:10.1016/j.chom.2019.01.006

Mottis A, Herzig S, Auwerx J. 2019. Mitocellular communication: Shaping health and disease. *Science* **366**:827–832. doi:10.1126/science.aax3768

Mukherjee S, Liu X, Arasaki K, McDonough J, Galán JE, Roy CR. 2011. Modulation of Rab GTPase function by a protein phosphocholine transferase. *Nature* **477**:103–106. doi:10.1038/nature10335

Müller MP, Goody RS. 2017. Molecular control of Rab activity by GEFs, GAPs and GDI. *Small Gtpases* **9**:5–21. doi:10.1080/21541248.2016.1276999

Müller MP, Peters H, Blümer J, Blankenfeldt W, Goody RS, Itzen A. 2010. The Legionella Effector Protein DrrA AMPylates the Membrane Traffic Regulator Rab1b. *Science* **329**:946–949. doi:10.1126/science.1192276

Münch C, Harper JW. 2016. Mitochondrial unfolded protein response controls matrix pre-RNA processing and translation. *Nature* **534**:710–713. doi:10.1038/nature18302

Murata T, Delprato A, Ingmundson A, Toomre DK, Lambright DG, Roy CR. 2006. The Legionella pneumophila effector protein DrrA is a Rab1 guanine nucleotide-exchange factor. *Nat Cell Biol* **8**:971–977. doi:10.1038/ncb1463

Nagai H, Kagan JC, Zhu X, Kahn RA, Roy CR. 2002. A Bacterial Guanine Nucleotide Exchange Factor Activates ARF on Legionella Phagosomes. *Science* **295**:679–682. doi:10.1126/science.1067025

Neunuebel MR, Mohammadi S, Jarnik M, Machner MP. 2012. Legionella pneumophila LidA Affects Nucleotide Binding and Activity of the Host GTPase Rab1. *J Bacteriol* **194**:1389–1400. doi:10.1128/jb.06306-11

Noack J, Jimenez-Morales D, Stevenson E, Moss T, Jang G, Krogan NJ, Swaney DL, Mukherjee S. 2020. Dynamic proteomics profiling of Legionella pneumophila infection unveils modulation

of the host mitochondrial stress response pathway. *bioRxiv* 2020.05.19.105395. doi:10.1101/2020.05.19.105395

Noack J, Mukherjee S. 2020. "Make way": Pathogen exploitation of membrane traffic. *Curr Opin Cell Biol* **65**:78–85. doi:10.1016/j.ceb.2020.02.011

Ochoa D, Jonikas M, Lawrence RT, Debs BE, Selkrig J, Typas A, Villén J, Santos SD, Beltrao P. 2016. An atlas of human kinase regulation. *Mol Syst Biol* **12**:888. doi:10.15252/msb.20167295

Oliva G, Sahr T, Buchrieser C. 2018. The Life Cycle of L. pneumophila: Cellular Differentiation Is Linked to Virulence and Metabolism. *Front Cell Infect Mi* **8**:3. doi:10.3389/fcimb.2018.00003

Ong SY, Schuelein R, Wibawa RR, Thomas DW, Handoko Y, Freytag S, Bahlo M, Simpson KJ, Hartland EL. 2021. Genome-wide genetic screen identifies host ubiquitination as important for Legionella pneumophila Dot/Icm effector translocation. *Cell Microbiol* **23**:e13368. doi:10.1111/cmi.13368

Osaka N, Hirota Y, Ito D, Ikeda Y, Kamata R, Fujii Y, Chirasani VR, Campbell SL, Takeuchi K, Senda T, Sasaki AT. 2021. Divergent Mechanisms Activating RAS and Small GTPases Through Post-translational Modification. *Frontiers Mol Biosci* **8**:707439. doi:10.3389/fmolb.2021.707439

Pakos-Zebrucka K, Koryga I, Mnich K, Ljujic M, Samali A, Gorman AM. 2016. The integrated stress response. *Embo Rep* **17**:1374–1395. doi:10.15252/embr.201642195

Peng H, Yang J, Li G, You Q, Han W, Li T, Gao D, Xie X, Lee B-H, Du J, Hou J, Zhang T, Rao H, Huang Y, Li Q, Zeng R, Hui L, Wang H, Xia Q, Zhang X, He Y, Komatsu M, Dikic I, Finley D, Hu R. 2017. Ubiquitylation of p62/sequestosome1 activates its autophagy receptor function and controls selective autophagy upon ubiquitin stress. *Cell Res* **27**:657–674. doi:10.1038/cr.2017.40

Pettersen EF, Goddard TD, Huang CC, Meng EC, Couch GS, Croll TI, Morris JH, Ferrin TE. 2021. UCSF ChimeraX: Structure visualization for researchers, educators, and developers. *Protein Sci* **30**:70–82. doi:10.1002/pro.3943

Price CTD, Al-Quadan T, Santic M, Rosenshine I, Kwaik YA. 2011. Host Proteasomal Degradation Generates Amino Acids Essential for Intracellular Bacterial Growth. *Science* **334**:1553–1557. doi:10.1126/science.1212868

Qiu J, Luo Z-Q. 2017a. Legionella and Coxiella effectors: strength in diversity and activity. *Nat Rev Microbiol* **15**:591–605. doi:10.1038/nrmicro.2017.67

Qiu J, Luo Z-Q. 2017b. Hijacking of the Host Ubiquitin Network by Legionella pneumophila. *Front Cell Infect Mi* **7**:487. doi:10.3389/fcimb.2017.00487

Qiu J, Sheedlo MJ, Yu K, Tan Y, Nakayasu ES, Das C, Liu X, Luo Z-Q. 2016. Ubiquitination independent of E1 and E2 enzymes by bacterial effectors. *Nature* **533**:120–124. doi:10.1038/nature17657

Quirós PM, Prado MA, Zamboni N, D'Amico D, Williams RW, Finley D, Gygi SP, Auwerx J. 2017. Multi-omics analysis identifies ATF4 as a key regulator of the mitochondrial stress response in mammals. *J Cell Biol* **216**:2027–2045. doi:10.1083/jcb.201702058

Rabouw HH, Langereis MA, Anand AA, Visser LJ, Groot RJ de, Walter P, Kuppeveld FJM van. 2019. Small molecule ISRIB suppresses the integrated stress response within a defined window of activation. *Proc National Acad Sci* **116**:201815767. doi:10.1073/pnas.1815767116

Ragaz C, Pietsch H, Urwyler S, Tiaden A, Weber SS, Hilbi H. 2008. The Legionella pneumophila phosphatidylinositol-4 phosphate-binding type IV substrate SidC recruits endoplasmic reticulum vesicles to a replication-permissive vacuole. *Cell Microbiol* **10**:2416–2433. doi:10.1111/j.1462-5822.2008.01219.x

Rainbolt TK, Atanassova N, Genereux JC, Wiseman RL. 2013. Stress-Regulated Translational Attenuation Adapts Mitochondrial Protein Import through Tim17A Degradation. *Cell Metab* **18**:908–919. doi:10.1016/j.cmet.2013.11.006

Rainbolt TK, Lebeau J, Puchades C, Wiseman RL. 2016. Reciprocal Degradation of YME1L and OMA1 Adapts Mitochondrial Proteolytic Activity during Stress. *Cell Reports* **14**:2041–2049. doi:10.1016/j.celrep.2016.02.011

Ramond E, Jamet A, Coureuil M, Charbit A. 2019. Pivotal Role of Mitochondria in Macrophage Response to Bacterial Pathogens. *Front Immunol* **10**:2461. doi:10.3389/fimmu.2019.02461

Rath S, Sharma R, Gupta R, Ast T, Chan C, Durham TJ, Goodman RP, Grabarek Z, Haas ME, Hung WHW, Joshi PR, Jourdain AA, Kim SH, Kotrys AV, Lam SS, McCoy JG, Meisel JD, Miranda M, Panda A, Patgiri A, Rogers R, Sadre S, Shah H, Skinner OS, To T-L, Walker MA, Wang H, Ward PS, Wengrod J, Yuan C-C, Calvo SE, Mootha VK. 2020. MitoCarta3.0: an updated mitochondrial proteome now with sub-organelle localization and pathway annotations. *Nucleic Acids Res* **49**:gkaa1011-. doi:10.1093/nar/gkaa1011

Raudvere U, Kolberg L, Kuzmin I, Arak T, Adler P, Peterson H, Vilo J. 2019. g:Profiler: a web server for functional enrichment analysis and conversions of gene lists (2019 update). *Nucleic Acids Res* **47**:W191–W198. doi:10.1093/nar/gkz369

Rolando M, Sanulli S, Rusniok C, Gomez-Valero L, Bertholet C, Sahr T, Margueron R, Buchrieser C. 2013. Legionella pneumophila Effector RomA Uniquely Modifies Host Chromatin to Repress Gene Expression and Promote Intracellular Bacterial Replication. *Cell Host Microbe* **13**:395–405. doi:10.1016/j.chom.2013.03.004

Rothmeier E, Pfaffinger G, Hoffmann C, Harrison CF, Grabmayr H, Repnik U, Hannemann M, Wölke S, Bausch A, Griffiths G, Müller-Taubenberger A, Itzen A, Hilbi H. 2013. Activation of Ran GTPase by a Legionella Effector Promotes Microtubule Polymerization, Pathogen Vacuole Motility and Infection. *Plos Pathog* **9**:e1003598. doi:10.1371/journal.ppat.1003598

Samluk L, Urbanska M, Kisielewska K, Mohanraj K, Kim M-J, Machnicka K, Liszewska E, Jaworski J, Chacinska A. 2019. Cytosolic translational responses differ under conditions of severe short-term and long-term mitochondrial stress. *Mol Biol Cell* **30**:1864–1877. doi:10.1091/mbc.e18-10-0628

Sapmaz A, Berlin I, Bos E, Wijdeven RH, Janssen H, Konietzny R, Akkermans JJ, Erson-Bensan AE, Koning RI, Kessler BM, Neefjes J, Ovaa H. 2019. USP32 regulates late endosomal transport and recycling through deubiquitylation of Rab7. *Nat Commun* **10**:1454. doi:10.1038/s41467-019-09437-x

Sasaki AT, Carracedo A, Locasale JW, Anastasiou D, Takeuchi K, Kahoud ER, Haviv S, Asara JM, Pandolfi PP, Cantley LC. 2011. Ubiquitination of K-Ras Enhances Activation and Facilitates Binding to Select Downstream Effectors. *Sci Signal* **4**:ra13. doi:10.1126/scisignal.2001518

Schator D, Mondino S, Berthelet J, Silvestre CD, Assaya MB, Rusniok C, Rodrigues-Lima F, Wehenkel A, Buchrieser C, Rolando M. 2023. Legionella para-effectors target chromatin and promote bacterial replication. *Nat Commun* **14**:2154. doi:10.1038/s41467-023-37885-z

Schindelin J, Arganda-Carreras I, Frise E, Kaynig V, Longair M, Pietzsch T, Preibisch S, Rueden C, Saalfeld S, Schmid B, Tinevez J-Y, White DJ, Hartenstein V, Eliceiri K, Tomancak P, Cardona A. 2012. Fiji: an open-source platform for biological-image analysis. *Nat Methods* **9**:676–682. doi:10.1038/nmeth.2019

Schmölders J, Manske C, Otto A, Hoffmann C, Steiner B, Welin A, Becher D, Hilbi H. 2017. Comparative Proteomics of Purified Pathogen Vacuoles Correlates Intracellular Replication of Legionella pneumophila with the Small GTPase Ras-related protein 1 (Rap1)*. *Mol Cell Proteomics* **16**:622–641. doi:10.1074/mcp.m116.063453

Schoebel S, Cichy AL, Goody RS, Itzen A. 2011. Protein LidA from Legionella is a Rab GTPase supereffector. *Proc National Acad Sci* **108**:17945–17950. doi:10.1073/pnas.1113133108

Schuelein R, Spencer H, Dagley LF, Li P fei, Luo L, Stow JL, Abraham G, Naderer T, Gomez-Valero L, Buchrieser C, Sugimoto C, Yamagishi J, Webb AI, Pasricha S, Hartland EL. 2018. Targeting of RNA Polymerase II by a nuclear Legionella pneumophila Dot/Icm effector SnpL. *Cell Microbiol* **20**:e12852. doi:10.1111/cmi.12852

Shannon P, Markiel A, Ozier O, Baliga NS, Wang JT, Ramage D, Amin N, Schwikowski B, Ideker T. 2003. Cytoscape: A Software Environment for Integrated Models of Biomolecular Interaction Networks. *Genome Res* **13**:2498–2504. doi:10.1101/gr.1239303

Shen X, Banga S, Liu Y, Xu L, Gao P, Shamovsky I, Nudler E, Luo Z. 2009. Targeting eEF1A by a Legionella pneumophila effector leads to inhibition of protein synthesis and induction of host stress response. *Cell Microbiol* **11**:911–926. doi:10.1111/j.1462-5822.2009.01301.x

Shin D, Mukherjee R, Liu Yaobin, Gonzalez A, Bonn F, Liu Yan, Rogov VV, Heinz M, Stolz A, Hummer G, Dötsch V, Luo Z-Q, Bhogaraju S, Dikic I. 2020. Regulation of Phosphoribosyl-Linked Serine Ubiquitination by Deubiquitinases DupA and DupB. *Mol Cell* **77**:164-179.e6. doi:10.1016/j.molcel.2019.10.019

Shin D, Na W, Lee J-H, Kim G, Baek J, Park SH, Choi CY, Lee S. 2017. Site-specific monoubiquitination downregulates Rab5 by disrupting effector binding and guanine nucleotide conversion. *Elife* **6**:e29154. doi:10.7554/elife.29154

Shin S, Case CL, Archer KA, Nogueira CV, Kobayashi KS, Flavell RA, Roy CR, Zamboni DS. 2008. Type IV Secretion-Dependent Activation of Host MAP Kinases Induces an Increased Proinflammatory Cytokine Response to Legionella pneumophila. *Plos Pathog* **4**:e1000220. doi:10.1371/journal.ppat.1000220

Shpilka T, Haynes CM. 2017. The mitochondrial UPR: mechanisms, physiological functions and implications in ageing. *Nat Rev Mol Cell Bio* **19**:109–120. doi:10.1038/nrm.2017.110

Sidrauski C, Acosta-Alvear D, Khoutorsky A, Vedantham P, Hearn BR, Li H, Gamache K, Gallagher CM, Ang KK-H, Wilson C, Okreglak V, Ashkenazi A, Hann B, Nader K, Arkin MR, Renslo AR, Sonenberg N, Walter P. 2013. Pharmacological brake-release of mRNA translation enhances cognitive memory. *Elife* **2**:e00498. doi:10.7554/elife.00498

Siegelin MD, Dohi T, Raskett CM, Orlowski GM, Powers CM, Gilbert CA, Ross AH, Plescia J, Altieri DC. 2011. Exploiting the mitochondrial unfolded protein response for cancer therapy in mice and human cells. *J Clin Invest* **121**:1349–1360. doi:10.1172/jci44855

Simon S, Wagner MA, Rothmeier E, Müller-Taubenberger A, Hilbi H. 2014. Icm/Dot-dependent inhibition of phagocyte migration by Legionella is antagonized by a translocated Ran GTPase activator. *Cell Microbiol* **16**:977–992. doi:10.1111/cmi.12258

Steger M, Tonelli F, Ito G, Davies P, Trost M, Vetter M, Wachter S, Lorentzen E, Duddy G, Wilson S, Baptista MA, Fiske BK, Fell MJ, Morrow JA, Reith AD, Alessi DR, Mann M. 2016. Phosphoproteomics reveals that Parkinson's disease kinase LRRK2 regulates a subset of Rab GTPases. *Elife* **5**:e12813. doi:10.7554/elife.12813

Steiner B, Weber S, Hilbi H. 2018. Formation of the Legionella-containing vacuole: phosphoinositide conversion, GTPase modulation and ER dynamics. *Int J Med Microbiol* **308**:49–57. doi:10.1016/j.ijmm.2017.08.004

Steklov M, Pandolfi S, Baietti MF, Batiuk A, Carai P, Najm P, Zhang M, Jang H, Renzi F, Cai Y, Asbagh LA, Pastor T, Troyer MD, Simicek M, Radaelli E, Brems H, Legius E, Tavernier J, Gevaert K, Impens F, Messiaen L, Nussinov R, Heymans S, Eyckerman S, Sablina AA. 2018. Mutations in LZTR1 drive human disease by dysregulating RAS ubiquitination. *Science* **362**:1177–1182. doi:10.1126/science.aap7607

Swaney DL, Villén J. 2016. Enrichment of Phosphopeptides via Immobilized Metal Affinity Chromatography. *Cold Spring Harb Protoc* **2016**:pdb.prot088005. doi:10.1101/pdb.prot088005

Swart AL, Steiner B, Gomez-Valero L, Schütz S, Hannemann M, Janning P, Irminger M, Rothmeier E, Buchrieser C, Itzen A, Panse VG, Hilbi H. 2020. Divergent Evolution of Legionella RCC1 Repeat Effectors Defines the Range of Ran GTPase Cycle Targets. *Mbio* **11**:e00405-20. doi:10.1128/mbio.00405-20

Tan Y, Arnold RJ, Luo Z-Q. 2011. Legionella pneumophila regulates the small GTPase Rab1 activity by reversible phosphorylcholination. *Proc National Acad Sci* **108**:21212–21217. doi:10.1073/pnas.1114023109

Theriot JA. 1995. The Cell Biology of Infection by Intracellular Bacterial Pathogens. *Annu Rev Cell Dev Biol* **11**:213–239. doi:10.1146/annurev.cb.11.110195.001241

Thul PJ, Åkesson L, Wiking M, Mahdessian D, Geladaki A, Blal HA, Alm T, Asplund A, Björk L, Breckels LM, Bäckström A, Danielsson F, Fagerberg L, Fall J, Gatto L, Gnann C, Hober S, Hjelmare M, Johansson F, Lee S, Lindskog C, Mulder J, Mulvey CM, Nilsson P, Oksvold P, Rockberg J, Schutten R, Schwenk JM, Sivertsson Å, Sjöstedt E, Skogs M, Stadler C, Sullivan DP, Tegel H, Winsnes C, Zhang C, Zwahlen M, Mardinoglu A, Pontén F, Feilitzen K von, Lilley KS, Uhlén M, Lundberg E. 2017. A subcellular map of the human proteome. *Science* **356**:eaal3321. doi:10.1126/science.aal3321

Thurston TLM, Ryzhakov G, Bloor S, Muhlinen N von, Randow F. 2009. The TBK1 adaptor and autophagy receptor NDP52 restricts the proliferation of ubiquitin-coated bacteria. *Nat Immunol* **10**:1215–1221. doi:10.1038/ni.1800

Tiku V, Kew C, Mehrotra P, Ganesan R, Robinson N, Antebi A. 2018. Nucleolar fibrillarin is an evolutionarily conserved regulator of bacterial pathogen resistance. *Nat Commun* **9**:3607. doi:10.1038/s41467-018-06051-1

Tiku V, Tan M-W, Dikic I. 2020. Mitochondrial Functions in Infection and Immunity. *Trends Cell Biol* **30**:263–275. doi:10.1016/j.tcb.2020.01.006

Torres M. 2016. Chapter Two - Heterotrimeric G Protein Ubiquitination as a Regulator of G Protein Signaling. *Prog Mol Biol Transl* **141**:57–83. doi:10.1016/bs.pmbts.2016.03.001

Tran CS, Eran Y, Ruch TR, Bryant DM, Datta A, Brakeman P, Kierbel A, Wittmann T, Metzger RJ, Mostov KE, Engel JN. 2014. Host Cell Polarity Proteins Participate in Innate Immunity to Pseudomonas aeruginosa Infection. *Cell Host Microbe* **15**:636–643. doi:10.1016/j.chom.2014.04.007

Treacy-Abarca S, Mukherjee S. 2015. Legionella suppresses the host unfolded protein response via multiple mechanisms. *Nat Commun* **6**:7887. doi:10.1038/ncomms8887
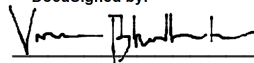
Udeshi ND, Mani DR, Eisenhaure T, Mertins P, Jaffe JD, Clauser KR, Hacohen N, Carr SA. 2012. Methods for Quantification of in vivo Changes in Protein Ubiquitination following Proteasome and Deubiquitinase Inhibition*. *Mol Cell Proteomics* **11**:148–159. doi:10.1074/mcp.m111.016857

Urwyler S, Nyfeler Y, Ragaz C, Lee H, Mueller LN, Aebersold R, Hilbi H. 2009. Proteome Analysis of Legionella Vacuoles Purified by Magnetic Immunoseparation Reveals Secretory and Endosomal GTPases. *Traffic* **10**:76–87. doi:10.1111/j.1600-0854.2008.00851.x

Vizcaíno JA, Csordas A, del-Toro N, Dianes JA, Griss J, Lavidas I, Mayer G, Perez-Riverol Y, Reisinger F, Ternent T, Xu Q-W, Wang R, Hermjakob H. 2016. 2016 update of the PRIDE database and its related tools. *Nucleic Acids Res* **44**:D447–D456. doi:10.1093/nar/gkv1145

Wang Y, Shi M, Feng H, Zhu Y, Liu S, Gao A, Gao P. 2018. Structural Insights into Non-canonical Ubiquitination Catalyzed by SidE. *Cell* **173**:1231-1243.e16. doi:10.1016/j.cell.2018.04.023

Wang Y, Wan B, Li D, Zhou J, Li R, Bai M, Chen F, Yu L. 2012. BRSK2 is regulated by ER stress in protein level and involved in ER stress-induced apoptosis. *Biochem Bioph Res Co* **423**:813–818. doi:10.1016/j.bbrc.2012.06.046

Waterhouse AM, Procter JB, Martin DMA, Clamp M, Barton GJ. 2009. Jalview Version 2—a multiple sequence alignment editor and analysis workbench. *Bioinformatics* **25**:1189–1191. doi:10.1093/bioinformatics/btp033

Webb-Robertson B-JM, Wiberg HK, Matzke MM, Brown JN, Wang J, McDermott JE, Smith RD, Rodland KD, Metz TO, Pounds JG, Waters KM. 2015. Review, Evaluation, and Discussion of the Challenges of Missing Value Imputation for Mass Spectrometry-Based Label-Free Global Proteomics. *J Proteome Res* **14**:1993–2001. doi:10.1021/pr501138h

Welch MD. 2015. Why should cell biologists study microbial pathogens? *Mol Biol Cell* **26**:4295–4301. doi:10.1091/mbc.e15-03-0144

Welch MD, Iwamatsu A, Mitchison TJ. 1997. Actin polymerization is induced by Arp 2/3 protein complex at the surface of Listeria monocytogenes. *Nature* **385**:265–269. doi:10.1038/385265a0

Welch MD, Rosenblatt J, Skoble J, Portnoy DA, Mitchison TJ. 1998. Interaction of Human Arp2/3 Complex and the Listeria monocytogenes ActA Protein in Actin Filament Nucleation. *Science* **281**:105–108. doi:10.1126/science.281.5373.105

Westermann B. 2012. Bioenergetic role of mitochondrial fusion and fission. *Biochimica Et Biophysica Acta Bba - Bioenergetics* **1817**:1833–1838. doi:10.1016/j.bbabio.2012.02.033

Xu G, Paige JS, Jaffrey SR. 2010. Global analysis of lysine ubiquitination by ubiquitin remnant immunoaffinity profiling. *Nat Biotechnol* **28**:868–873. doi:10.1038/nbt.1654

Yau R, Rape M. 2016. The increasing complexity of the ubiquitin code. *Nat Cell Biol* **18**:579–586. doi:10.1038/ncb3358

Zemirli N, Morel E, Molino D. 2018. Mitochondrial Dynamics in Basal and Stressful Conditions. *Int J Mol Sci* **19**:564. doi:10.3390/ijms19020564

Zhao Q, Wang J, Levichkin IV, Stasinopoulos S, Ryan MT, Hoogenraad NJ. 2002. A mitochondrial specific stress response in mammalian cells. *Embo J* **21**:4411–4419. doi:10.1093/emboj/cdf445

Zhou Y, Zhou B, Pache L, Chang M, Khodabakhshi AH, Tanaseichuk O, Benner C, Chanda SK. 2019. Metascape provides a biologist-oriented resource for the analysis of systems-level datasets. *Nat Commun* **10**:1523. doi:10.1038/s41467-019-09234-6

Zhu B, Zheng Y, Pham A-D, Mandal SS, Erdjument-Bromage H, Tempst P, Reinberg D. 2005. Monoubiquitination of Human Histone H2B: The Factors Involved and Their Roles in HOX Gene Regulation. *Mol Cell* **20**:601–611. doi:10.1016/j.molcel.2005.09.025

Publishing Agreement

It is the policy of the University to encourage open access and broad distribution of all theses, dissertations, and manuscripts. The Graduate Division will facilitate the distribution of UCSF theses, dissertations, and manuscripts to the UCSF Library for open access and distribution. UCSF will make such theses, dissertations, and manuscripts accessible to the public and will take reasonable steps to preserve these works in perpetuity.

I hereby grant the non-exclusive, perpetual right to The Regents of the University of California to reproduce, publicly display, distribute, preserve, and publish copies of my thesis, dissertation, or manuscript in any form or media, now existing or later derived, including access online for teaching, research, and public service purposes.

DocuSigned by:

_____   12/14/2023
16D5A12E8BB2464...   Author Signature   Date